

# Preference for evolving dark energy in light of the galaxy bispectrum

Zhiyu Lu<sup>1,2,3</sup>, Théo Simon<sup>4</sup>, and Pierre Zhang<sup>5,6,7</sup>

<sup>1</sup> *Department of Astronomy, School of Physical Sciences, University of Science and Technology of China  
Hefei, Anhui 230026, China*

<sup>2</sup> *CAS Key Laboratory for Researches in Galaxies and Cosmology, School of Astronomy and Space  
Science, University of Science and Technology of China, Hefei, Anhui 230026, China*

<sup>3</sup> *Deep Space Exploration Laboratory, Hefei 230088, China*

<sup>4</sup> *Laboratoire Univers & Particules de Montpellier, CNRS & Université de Montpellier, 34095  
Montpellier, France*

<sup>5</sup> *Institute for Particle Physics and Astrophysics, ETH Zürich, 8093 Zürich, Switzerland*

<sup>6</sup> *Institut für Theoretische Physik, ETH Zürich, 8093 Zürich, Switzerland*

<sup>7</sup> *Dipartimento di Fisica “Aldo Pontremoli”, Università degli Studi di Milano, 20133 Milan, Italy*

## Abstract

We analyse pre-DESI clustering data using a dark energy equation of state  $w(z)$  parametrised by  $(w_0, w_a)$ , finding a  $2.8 - 3.9\sigma$  preference for evolving dark energy over the cosmological constant  $\Lambda$  when combined with cosmic microwave background data from *Planck* and supernova data from Pantheon+, Union3, or DESY5. Our constraints, consistent with DESI Y1 results, are derived from the power spectrum and bispectrum of SDSS/BOSS galaxies using the Effective Field Theory of Large Scale Structure (EFTofLSS) at one loop. The evidence remains robust across analysis variations but disappears without the one-loop bispectrum. When combining DESI baryon acoustic oscillations with BOSS full-shape data, while marginalising over the sound horizon in the latter to prevent unaccounted correlations, the significance increases to  $3.7 - 4.4\sigma$ , depending on the supernova dataset. Using a data-driven reconstruction of  $w(z)$ , we show that the evidence arises from deviations from  $\Lambda$  at multiple redshifts. In addition, our findings are interpreted within the Effective Field Theory of Dark Energy (EFTofDE), from which we explicitly track the non-standard time evolution in EFTofLSS predictions. For perturbatively stable theories in the  $w < -1$  regime, the evidence persists in the clustering limit ( $c_s^2 \rightarrow 0$ ) when higher-derivative corrections are present, as well as in the quasi-static limit ( $c_s^2 \rightarrow 1$ ) when additional EFTofDE parameters are considered.

# Contents

<b>1</b>	<b>Introduction</b>	<b>2</b>
<b>2</b>	<b>Dark energy meet galaxies</b>	<b>4</b>
2.1	EFTofDE . . . . .	5
2.2	Three shades of quintessence . . . . .	9
2.3	EFTofLSS . . . . .	10
<b>3</b>	<b>Inference setup</b>	<b>17</b>
3.1	Probing evolution in the dark . . . . .	18
3.2	Datasets and inference framework . . . . .	18
3.3	EFT likelihood . . . . .	20
<b>4</b>	<b>Cosmological results</b>	<b>22</b>
4.1	$w_0w_a$ CDM . . . . .	22
4.2	Consistency checks . . . . .	26
4.3	$w_0w_a$ CDM + $\Omega_k$ . . . . .	30
4.4	$w_0w_a$ CDM in modified gravity . . . . .	30
<b>5</b>	<b>Discussions</b>	<b>32</b>
5.1	Dark energy histories . . . . .	32
5.2	Quantifying the phantom evidence . . . . .	35
5.3	Stability for $w < -1$ . . . . .	36
<b>6</b>	<b>Conclusions</b>	<b>38</b>
<b>A</b>	<b>Details on the EFTofLSS</b>	<b>40</b>
A.1	Time dependence in presence of quintessence . . . . .	40
A.2	Time dependence in modify gravity . . . . .	41
A.3	Bias expansion . . . . .	43
<b>B</b>	<b>Supplementary analysis products</b>	<b>43</b>
<b>C</b>	<b>Reconstructing <math>w(z)</math> histories</b>	<b>44</b>

## 1 Introduction

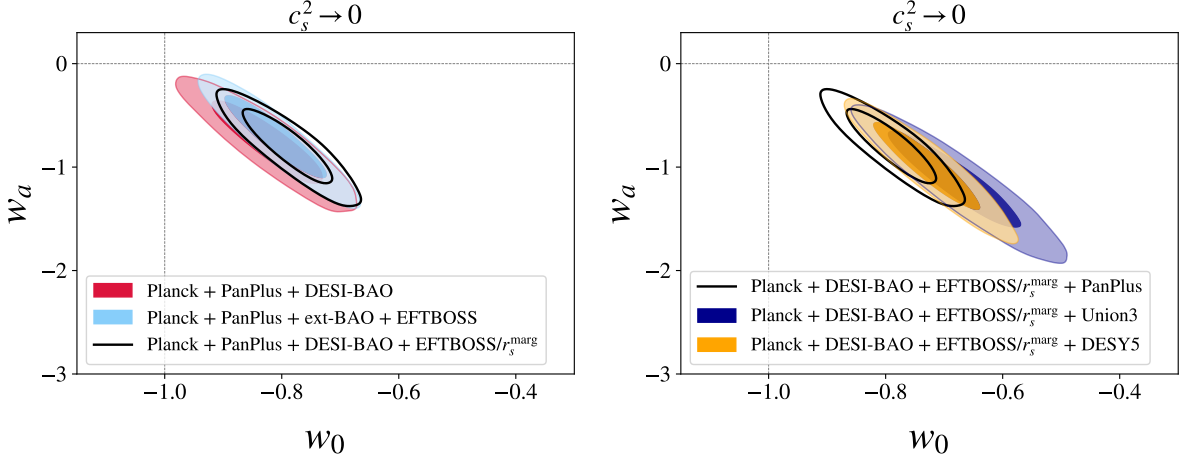
What drives the accelerated expansion of the Universe if not a cosmological constant  $\Lambda$ ? Understanding the nature of dark energy remains one of the most pressing questions in cosmology, and is central to major ongoing redshift survey programmes such as DESI [1] and Euclid [2]. By mapping the large-scale structure (LSS) of the Universe over increasingly large volumes, these

surveys will measure the cosmic expansion with percent precision, providing stringent tests for potential deviations from  $\Lambda$ . Notably, the recently released DESI Year 1 (Y1) data revealed a mild ( $2 - 4\sigma$ ) preference for evolving dark energy based on the baryon acoustic oscillations (BAO) and the full-shape modelling of the power spectrum [3]. Despite these promising prospects, an inherent limitation remains: the observable Universe at low redshifts, where effects of dark energy are detectable, provides only a finite data volume. Maximising the information extraction from LSS is therefore crucial.

In this work, we revisit the analysis of pre-DESI data with three main objectives. First, we demonstrate the constraining power of the Effective Field Theory of LSS (EFTofLSS) [4, 5] on dark energy properties, extending beyond the now-conventional one-loop power spectrum (see *e.g.*, refs. [6–14, 3] for an overview of progress in the field). The bispectrum of galaxies at one loop, as developed in refs. [15–17], enables unprecedented precision on the dark energy equation of state  $w$ , as recently highlighted in ref. [18]. Here, we extend this investigation by allowing for time variations in  $w$ . Second, we provide an independent cross-check of the preference for evolving dark energy over  $\Lambda$  observed in DESI data by analysing earlier galaxy surveys, SDSS/BOSS [19, 20]. Additionally, we assess the significance for evolving dark energy when combining DESI BAO with BOSS full-shape data, using the sound horizon information from the former while marginalizing over it in the latter. Third, we explore how constraints on  $w$  depend on theoretical assumptions about dark energy, based on the Effective Field Theory of Dark Energy (EFTofDE) [21, 22]. In conjunction with the EFTofLSS, our symmetry-based approach provides a unified theoretical framework for consistently treating dark energy fluctuations in LSS. A key novelty in this aspect is an explicit derivation of the exact time dependence in the EFTofLSS in presence of dark energy for the bispectrum, considering two phenomenologically distinct limits: the clustering ( $c_s^2 \rightarrow 0$ ) and smooth ( $c_s^2 \rightarrow 1$ ) regime. Our main results are summarised in fig. 1.

This work is organised as follow. In sec. 2, we review the EFTofDE and the EFTofLSS, highlighting the observational consequences for LSS in the presence of dark energy. Our inference setup is presented in sec. 3. Cosmological results are presented in sec. 4, and their significance is further discussed in sec. 5. We finally conclude in sec. 6. Supplementary materials are provided in appendices. App. A provides details on the EFTofLSS in presence of dark energy, and additional analysis products are given in app. B. Finally, a methodology to reconstruct  $w(z)$  from the data or within a specific model is detailed in app. C.

**Conventions** In this paper, we adopt the following conventions. To denote quantities that evolve across the cosmic history, we use interchangeably the physical time  $t$ , the scale factor  $a$  (normalised today at  $a_0 \equiv 1$ ), or the redshift  $z$ . Dotted quantities are derivatives with respect to  $t$ , *e.g.*,  $\dot{x} \equiv dx/dt$ .  $H = \dot{a}/a$  is the Hubble parameter, and  $\mathcal{H} \equiv aH$  is the comoving Hubble parameter. Quantities in bold like  $\mathbf{x}$  or written with one index like  $x_i$  refer to vectors, and with more indices like  $x_{ij}$  represent tensors. Repeated indices are understood to be summed over following Einstein conventions. We use interchangeably lower or upper cases for the indices, *e.g.*,  $x_i \equiv x^i$ .  $\partial_i$  refers to a derivatives with respect to space dimension  $i$ , and  $\partial^2$  is the Laplacian operator.



Dataset	$w_0$	$w_a$	$p > \Lambda$	$\Delta\chi^2$
<i>Planck</i> + PanPlus + DESI-BAO	$-0.821 \pm 0.063$	$-0.77 \pm 0.27$	$2.5\sigma$	-8.9
<i>Planck</i> + PanPlus + ext-BAO + EFTBOSS	$-0.809^{+0.053}_{-0.061}$	$-0.72^{+0.28}_{-0.25}$	$2.8\sigma$	-10.3
<i>Planck</i> + PanPlus + DESI-BAO + EFTBOSS/ $r_s^{\text{marg}}$	$-0.789 \pm 0.050$	$-0.80^{+0.25}_{-0.22}$	$3.7\sigma$	-16.9
<i>Planck</i> + Union3 + DESI-BAO + EFTBOSS/ $r_s^{\text{marg}}$	$-0.677 \pm 0.075$	$-1.14^{+0.33}_{-0.29}$	$3.8\sigma$	-17.7
<i>Planck</i> + DESY5 + DESI-BAO + EFTBOSS/ $r_s^{\text{marg}}$	$-0.726 \pm 0.060$	$-1.00^{+0.30}_{-0.25}$	$4.4\sigma$	-22.9

Figure 1: **Constraints on  $(w_0, w_a)$  across dataset combinations** — 2D posterior distributions in the  $w_0 - w_a$  plane obtained by fitting cosmic microwave background data from *Planck* alongside various galaxy clustering datasets (*upper left*) and supernova datasets (*upper right*), within the  $w_0 w_a$  CDM model. Corresponding 68% credible intervals, as well as the preference over  $\Lambda$  ( $p > \Lambda$ ) and the associated  $\Delta\chi^2$ , are also shown (*lower panel*). For the comparison of galaxy clustering data, we consider SDSS/BOSS [19] full-shape (FS) power spectrum and bispectrum (dubbed EFTBOSS), DESI Y1 BAO [1], or their combination, using Pantheon+ supernovae. For the comparison of supernova data, we consider Pantheon+ [23], Union3 [24], or DESY5 [25], using EFTBOSS + DESI-BAO as the galaxy clustering dataset. When combining EFTBOSS with DESI-BAO, the sound horizon information is marginalised over in EFTBOSS (dubbed  $r_s^{\text{marg}}$ ), avoiding unaccounted correlations between the two datasets. When analysed separately, we complete BOSS data with additional pre-DESI BAO measurements [26, 27, 20] (dubbed ext-BAO). Here we show the results corresponding to the  $c_s^2 \rightarrow 0$  (*i.e.*, clustering quintessence) limit in the EFTofDE, using the EFTofLSS at one loop. See main text for details. All the cosmological results are shown in sec. 4.

## 2 Dark energy meet galaxies

In this work, we aim to probe deviations from an expanding Universe accelerated by a cosmological constant  $\Lambda$ . We assume the existence of a physical clock, the so-called dark energy, whose evolution we track by profiling its equation of state  $w(t)$ . To do so, we will consider various phenomenological parametrisations for  $w(t)$  in sec. 3.1. We work under the lamppost of effective-field theories (EFT), guiding our explorations in what are the physically-allowed observational consequences (especially at the perturbative level) by ensuring that basic principles, such as spacetime symmetries, are respected. In sec. 2.1, we review the EFTofDE. We then isolate in sec. 2.2 three phenomenologically-distinct classes of stable theories of dark energy. Finally in sec. 2.3, we derive

their observational imprints in gravitational clustering under the framework of the EFTofLSS.

## 2.1 EFTofDE

Departure from  $\Lambda$  can be probed under the assumption that (spontaneously-broken) time translations are nonlinearly realised around a Fridman-Lemaître spacetime. The EFTofDE [28, 29, 21, 22] allows us to systematically organise the expansions of the fluctuations that remain invariant under the preserved (time-dependent) spatial diffeomorphisms, providing us a consistent and model-independent parametrisation of deviations from  $\Lambda$ . We focus on an EFT with one scalar degree of freedom, corresponding to the Goldstone boson associated to spontaneously-broken time translations. Working in the unitary gauge, we consider the following gravitational action [28, 30],

$$S_G = \int d^4x \sqrt{-g} \left[ \frac{M_{\text{pl}}^2}{2} R - \Lambda(t) - c(t)g^{00} + \frac{m_2^4(t)}{2}(\delta g^{00})^2 - \frac{m_3^3}{2}\delta g^{00}\delta K \right], \quad (2.1)$$

where the metric  $g_{\mu\nu}$ , and the operators built from it, are in the unitary gauge as well. Here  $\delta g^{00} = 1 + g^{00}$  are the perturbations in the 00-component of the metric  $g^{00}$ ,  $\delta K_\mu^\nu = K_\mu^\nu - H\delta_\mu^\nu$  are the perturbations of the extrinsic curvature, and  $\delta K = K - 3H$  is the trace of the latter. In full generality, other operators can show up at quadratic order in perturbations and leading order in spatial derivatives, such as combinations involving  $\delta K_\mu^\nu \delta K_\nu^\mu$  or  $\delta K^2$ . Moreover, additional ones appear at cubic and quartic order, and one could also consider a time-dependent Planck mass,  $M_{\text{pl}} \rightarrow M_* f(t)$  [22]. For simplicity, in this work we consider eq. (2.1). Moreover, we take the action for matter  $S_M$  to be fully diffeomorphism invariant such that no couplings between the fluctuations of dark energy and matter are considered.

**Background equations** The matter sector contributes to the background equations through the matter energy density  $\bar{\rho}_m(t)$ , while the matter pressure is null,  $\bar{p}_m(t) = 0$ . By analogy, it is useful to perform a change of variables of the zeroth-order functions  $c(t)$  and  $\Lambda(t)$  in eq. (2.1) to the energy density  $\bar{\rho}_d(t)$  and pressure  $\bar{p}_d(t)$  of a dark component,

$$2c(t) = \bar{\rho}_d(t) + \bar{p}_d(t), \quad 2\Lambda(t) = \bar{\rho}_d(t) - \bar{p}_d(t). \quad (2.2)$$

Solving the zeroth-order Einstein equations and re-arranging them, leads to the usual Fridman equations,

$$H^2 = \frac{1}{3M_{\text{pl}}^2}(\bar{\rho}_m + \bar{\rho}_d), \quad (2.3)$$

$$\dot{H} = -\frac{1}{2M_{\text{pl}}^2}(\bar{\rho}_m + \bar{\rho}_d + \bar{p}_d), \quad (2.4)$$

where the time dependence is dropped from the notation to remove clutter. Defining the usual fractional energy densities as

$$\Omega_i = \frac{\bar{\rho}_i}{3M_{\text{pl}}^2 H^2}, \quad i = m, d, \quad (2.5)$$

satisfying  $\Omega_m + \Omega_d = 1$ , the equation of state of dark energy is then given by

$$w \equiv \frac{\bar{p}_d}{\bar{\rho}_d} = -\frac{1}{1 - \Omega_m} \left( 1 + \frac{2}{3} \frac{\dot{H}}{H^2} \right) . \quad (2.6)$$

Conservation of the matter stress-energy tensor implies the usual continuity equation for matter,

$$\dot{\bar{\rho}}_m + 3H\bar{\rho}_m = 0 . \quad (2.7)$$

Dotting (2.3) and using (2.4) and (2.7), lead to an analogous equation for the evolution of the dark component,

$$\dot{\bar{\rho}}_d + 3(1 + w)H\bar{\rho}_d = 0 . \quad (2.8)$$

Given an equation of state  $w(t)$ , we can solve  $\bar{\rho}_d$  in (2.8) using the first Fridman equation (2.3). It is convenient to rewrite the Hubble and the matter density parameters with respect to their values at present time  $H_0$  and  $\Omega_{m,0}$ , as

$$H = H_0 \sqrt{\Omega_{m,0} a^{-3} + (1 - \Omega_{m,0}) a^{-3(1+\tilde{w})}} , \quad \Omega_m = \frac{\Omega_{m,0} a^{-3}}{(H/H_0)^2} , \quad (2.9)$$

where

$$\tilde{w} = \frac{1}{\ln a} \int_1^a \frac{w(a')}{a'} da' . \quad (2.10)$$

**Perturbation equations** From the action (2.1) in unitary gauge, we can reintroduce the Goldstone mode  $\pi$  via the Stückelberg trick, restoring manifest general covariance. This amounts to perform a time coordinate change  $t \rightarrow t + \pi$  and track the resulting transformations in the quantities appearing in (2.1). To describe gravitational perturbations, we consider the perturbed FLRW metric in Newtonian gauge,

$$ds^2 = -(1 + 2\Phi)dt^2 + a(t)^2(1 - 2\Psi)\delta_{ij}dx^i dx^j , \quad (2.11)$$

where we ignore tensor fluctuations. Expanding the gravitational action (2.1) together with the one of matter up to quadratic order in perturbations leads to the quadratic action governing the linear propagation of scalar fluctuations (see *e.g.*, [31] for details). Variation of the quadratic action with respect to  $\pi$  then leads to an equation of motion for the propagating mode  $\pi$  [22, 31]. The dispersion relation  $\omega^2 = c_s^2 k^2$  can be read off from the kinematic part, defining a speed of sound for  $\pi$ ,

$$c_s^2 = \frac{\nu}{\alpha} , \quad (2.12)$$

where

$$\nu = -\alpha_B^2 + \alpha_B \left( \alpha_w - 1 + \frac{3}{2} \Omega_m \right) + \alpha_w - \frac{\dot{\alpha}_B}{H} , \quad (2.13)$$

$$\alpha = \alpha_w + \alpha_K + 3\alpha_B^2 . \quad (2.14)$$

Using the background equations and the definition of  $w$ , *i.e.*, eq. (2.6), we have defined dimensionless time-dependent parameters,

$$\alpha_w \equiv \frac{c}{M_{\text{pl}}^2 H^2} = \frac{3}{2}(1+w)(1-\Omega_m) , \quad (2.15)$$

together with<sup>1</sup>

$$\alpha_K = \frac{2m_2^4}{M_{\text{pl}}^2 H^2} , \quad \alpha_B = -\frac{m_3^3}{2M_{\text{pl}}^2 H} . \quad (2.16)$$

Varying the quadratic action with respect to metric perturbations yields the linear perturbed Einstein equations [22, 31]. There are two constraint equations, the first relating  $\Phi - \Psi$  to the anisotropic stress tensors,<sup>2</sup> and the second being a generalised Poisson equation relating  $\partial^2 \Psi$  with the fluctuations in matter or dark energy. General formulae can be found in [22]. To close the linear system of equations, conservation of the stress-energy tensor further leads to the continuity and Euler equations for the matter fluctuations. Since we will be interested in describing the galaxy distribution at the shortest possible distance, it is useful to consider the full nonlinear equations for the matter fluctuations [4, 34],

$$\dot{\delta} + \frac{1}{a}\theta = -\frac{1}{a}\partial_i(\delta v^i) , \quad (2.17)$$

$$\dot{\theta} + H\theta + \frac{1}{a}\partial^2 \Phi = -\frac{1}{a}\partial_i(v^j \partial_j v^i) , \quad (2.18)$$

where  $\delta \equiv \rho_m/\bar{\rho}_m - 1$  is the matter overdensity field,  $v^i$  is the matter velocity field, and  $\theta \equiv \partial_i v^i$  is the velocity divergence.<sup>3</sup>

**Quasi-static limit** Scales observed in galaxy surveys are much shorter than the Hubble radius such that relativistic corrections can be neglected. Moreover, for sufficiently large speed of sound,  $c_s^2 \rightarrow 1$ , they are well below the sound horizon. When so, gravitational and field fluctuations on these scales can be assumed to evolve in the quasi-static approximation where time derivatives are much smaller than spatial derivatives. In this limit, the field equations take a particularly simple form [35],

$$\partial^2 \Phi = \frac{\bar{\rho}_m a^2}{2M_{\text{pl}}^2} \left( 1 + \frac{\alpha_B^2}{\nu} \right) \delta , \quad (2.19)$$

$$H\partial^2 \pi = \frac{\bar{\rho}_m a^2}{2M_{\text{pl}}^2} \frac{\alpha_B}{\nu} \delta . \quad (2.20)$$

---

<sup>1</sup>Notice that our definitions differ slightly from the ones of *e.g.*, [32, 33].

<sup>2</sup>At linear order, the anisotropic stress tensors are zero thus setting  $\Psi = \Phi$ . In general in this work, we consider  $\Psi = \Phi$  (up to small corrections from neutrinos) as we neglect relativistic corrections, sub-leading at LSS survey scales.

<sup>3</sup>Here we have left out the vorticity component of the velocity,  $w_i \sim \epsilon_{ijk} \partial^j v^k$ , which starts contributing at forth order in fluctuations (more on that latter). This does not affect the present discussion, as we focus only on modifications due to the presence of dark energy up to third order for reasons that we explain later.

Here the propagation of  $\pi$  is fully determined by the matter fluctuations  $\delta$ . The sole difference with general relativity lies in a modification of the Poisson equation. If  $\alpha_B = 0$ , there is no dark energy fluctuations participating to clustering, and we recover standard smooth quintessence. In principle, one can also consider nonlinear corrections stemming from higher-order operators that have been neglected in (2.1). Formulae for the generalised Poisson equation, that we provide in app. A.2, and their analog equations for  $\Psi$  and  $\pi$  in the EFTofDE within the quasi-static approximation have been derived up to third order in fluctuations in ref. [35].

**Clustering limit** Another phenomenologically interesting limit is obtained for vanishing sound speed,  $c_s^2 \rightarrow 0$ . When so, fluctuations in dark energy fall in potential wells, thus participating to gravitational clustering. Without lack of generality, we set  $m_3^2 = 0$  in the following discussion, as the resulting equations relevant for LSS remains unchanged otherwise [31]. In the limit  $c_s^2 \rightarrow 0$ , eq. (2.12) yields  $m_2^4 \approx \bar{\rho}_d(1+w)/(4c_s^2)$ , and the linear equation for  $\pi$  reads [30, 31]

$$\frac{1}{a^3 m_2^4} \frac{d}{dt} [a^3 m_2^4 (\dot{\pi} - \Phi)] = \frac{1}{a^2} \frac{c_s^2}{1 - c_s^2} \partial^2 \pi . \quad (2.21)$$

Counting powers of  $c_s^2$ , we see that the r.h.s. is negligible. This shows that, once the decaying mode has fade away,  $\dot{\pi} - \Phi = 0$ , implying  $\partial_i \dot{\pi} - \partial_i \Phi = 0$ . Since  $\partial_i \Phi = -\frac{d}{dt}(av^i)$  from linearising the Euler equation (2.18), we find that the two species are comoving,

$$\partial_i \pi = -av^i . \quad (2.22)$$

The Poisson equation is then sourced by a single growing adiabatic mode [30, 36],

$$\partial^2 \Phi = \frac{\bar{\rho}_m a^2}{2M_{\text{pl}}^2} \delta_A , \quad \delta_A = \delta + \delta_d , \quad (2.23)$$

where we have defined a quintessence overdensity field as

$$\delta_d = \frac{4m_2^4}{\bar{\rho}_m} (\dot{\pi} - \Phi) \approx \frac{1+w}{c_s^2} \frac{\bar{\rho}_d}{\bar{\rho}_m} (\dot{\pi} - \Phi) . \quad (2.24)$$

Using (2.17) and (2.21), together with  $\partial^2 \pi = -a^2 \theta$  that follows from (2.22), dotting  $\delta_A$  leads to the linear continuity equation for the adiabatic mode,

$$\dot{\delta}_A + \frac{1}{a} C(a) \theta = 0 , \quad (2.25)$$

where we have defined

$$C(a) = 1 + (1+w) \frac{\bar{\rho}_d}{\bar{\rho}_m} . \quad (2.26)$$

The Euler equation for the adiabatic mode simply follows from relating  $\theta_A = \theta$  (as the two species are comoving) to the gravitational potential using (2.18). Derivation of the equations of motion at nonlinear order, relying on an argument that shows that the two species remain comoving, can be found in [31]. The nonlinear continuity and Euler equations for the adiabatic mode read [31]

$$\dot{\delta}_A + \frac{1}{a} C(a) \theta = -\frac{1}{a} \partial_i (\delta_A v^i) , \quad (2.27)$$

$$\dot{\theta} + H\theta + \frac{1}{a} \partial^2 \Phi = -\frac{1}{a} \partial_i (v^j \partial_j v^i) . \quad (2.28)$$



**Stability** To ensure the absence of gradient instabilities, the sound speed  $c_s^2$  defined in (2.12) has to be positive. To avoid ghost instabilities, we can further impose that the kinematic energy of  $\pi$  (proportional to  $\alpha$ ) has to be positive as well. These requirements yield

$$\alpha > 0, \quad \nu \geq 0. \quad (2.29)$$

Allowing  $\alpha_B$  and  $\alpha_K$  to take large values  $\sim \mathcal{O}(1)$  (see refs. [37, 38]), one can show that the stability requirements (2.29) can be generically satisfied even for  $w < -1$ . This is also the case when generalising the action (2.1) with a time-dependent Planck mass or in the presence of the quadratic operator leading to tensor modes propagating at non-luminal speed [22].

For  $\alpha_w \sim \alpha_B \ll \alpha_K \sim \mathcal{O}(1)$ , *i.e.*,  $m_3^3 \sim m_2^4$  and  $w \sim -1$ , the propagation of  $\pi$  can still be stabilised in a region  $w < -1$ , not too far from  $w = -1$ : the kinetic and the gradient terms remain positive provided that  $\alpha \approx \alpha_K > 0$ ,  $\nu \approx \alpha_w - \alpha_B(p + 1 + \frac{3}{2}\Omega_m) > 0$ . When so, the speed of sound is small,  $c_s^2 \ll 1$ . Note that this limit is technically natural:  $c_s^2 \equiv 0$  is protected by the presence of a shift symmetry [39, 28], which in particular enforces  $\alpha_B \equiv 0$ . Higher-derivative operators not shown in (2.1) can also lead to stable propagations even when  $c_s^2 < 0$  for  $w < -1$  [28, 30]: leading to a modified dispersion relation of the type  $w^2 \sim k^4$ , they act as a cutoff — confining the gradient instability to (quantum-safe) large scales. However, this is effective only if  $c_s^2 \rightarrow 0$  as shown to be necessary for the rate of the instability to not grow too fast within a Hubble time [30].

When all operators (but the zeroth-order ones) are small, we are in the regime of  $k$ -essence with unit sound speed, where nothing in the EFT can prevent ghost instabilities when the null energy condition is violated. To summarise, based on stability requirements, we consider three classes of theories: *i*)  $k$ -essence where  $w < -1$  is not allowed, *ii*) EFTofDE in the quasi-static limit, stable for all  $w$  with large  $c_s^2 \rightarrow 1$ , yielding a modified Poisson equation (2.19), and *iii*) clustering quintessence with  $c_s^2 \rightarrow 0$  where  $w \lesssim -1$  is allowed. We now review them in regards of their distinct phenomenology, whose description we complete in sec. 2.3 for their imprints on the LSS.

## 2.2 Three shades of quintessence

From considerations on the stability of fluctuations in dark energy, we have distinguished three broad classes of theories. In this section, we describe their distinct observational signatures. Their main features, summarised in tab. 1, are detailed below.

**Smooth quintessence** This is the standard  $k$ -essence with unit sound speed,  $c_s^2 = 1$ . At the background level, the cosmological constant is replaced by a dark energy component with a general equation of state  $w(t)$ . At the perturbation level, the structure of the time dependence in the EFTofLSS is modified when  $w \neq -1$ : this will be detailed in the next section. EFTofDE operators are negligible, *e.g.*,  $\alpha_K, \alpha_B = 0$ . There is thus nothing in the EFT that prevents from ghost instabilities when the null energy condition is violated. When considering such theory in sec. 5.3, we safely impose a physical cut on the equation of state,  $-1 < w$ . See ref. [40] for a class of  $k$ -essence models appearing natural and stable under quantum corrections.

Dark energy theories	$c_s^2$	$w < -1$	Signatures in LSS perturbations
Standard $k$ -essence	1	Prohibited	non-EdS time evolution
Smooth quintessence in modified gravity	1	Stable	Modified time evolution from generalised Poisson equation
Clustering quintessence	0	Stable	Modified time evolution from dark energy clustering

Table 1: Classification of dark energy theories within the EFTofDE according to their distinct observational consequences in LSS (galaxy clustering at the perturbative level). Stability requirements in the propagations of dark energy fluctuations impose restrictions when probing  $w(t)$ . See main text for more details.

**Smooth quintessence in modified gravity** This is the regime of the EFTofDE that is stable in regions where  $w < -1$ , *i.e.*, where the stability requirements (2.29) are met, preventing ghost and gradient instabilities. We consider the limit  $c_s^2 \rightarrow 1$  where the quasi-static approximation is valid at scales observed in galaxy surveys. This leads to a modified Poisson equation (2.19), generalisable to higher order in fluctuations [35], which in turn modifies the time evolution of EFTofLSS operators [34] (see app. A.2). When considering smooth quintessence, additional degrees of freedom, *e.g.*,  $\alpha_B$ , need to be marginalised to probe the  $w < -1$  region safely. See refs. [37, 38] for the cubic Galileon — a class of models where  $\alpha_B$  can naturally takes large ( $\sim \mathcal{O}(1)$ ) values, thereby preventing gradient instabilities.

**Clustering quintessence** Instabilities can be avoided when  $w < -1$  in the limit of a vanishing sound speed ( $c_s^2 \rightarrow 0$ ) without extra degrees of freedom (relevant at cosmological scales), provided that  $w$  stays relatively close to  $w = -1$  [30]. We explicitly check that those theoretical bounds are satisfied in sec. 5.3. In the limit  $c_s^2 \rightarrow 0$ , the dark energy and matter fluctuations form a single growing adiabatic mode relevant to gravitational clustering. The equations of motion for the matter fluctuations, eqs. (2.17) and (2.18), are replaced by analogous ones for the adiabatic mode sourcing the gravitational potential, eqs. (2.27) and (2.28).

In this work, we analyse the equation of state  $w(t)$  both in the presence of smooth ( $c_s^2 \rightarrow 1$ ) and clustering ( $c_s^2 \rightarrow 0$ ) quintessence. The main results presented in sec. 4 are obtained imposing no prior on  $w$  and without marginalising over additional EFTofDE parameters (using the standard fluid approximation). In sec. 5.3, we revisit the constraints on dark energy in light of the stability of the fluctuations.

## 2.3 EFTofLSS

To make contact with observations, *i.e.*, maps of distant massive objects such as galaxies, we make use of the EFTofLSS [4, 5, 31, 34, 15]. At sufficiently long distances, the equivalence principle allows for a perturbative description of gravitational clustering: all dust-like fields at long distances are governed by the same symmetries. A long-wavelength field  $\phi_\ell$  at position  $\mathbf{x}$  in the Universe is invariant under translations and Galilean boosts — *i.e.*, the Newtonian limit of diffeomorphism [41–

43],

$$\mathbf{x} \rightarrow \mathbf{x} + \mathbf{n} , \quad \mathbf{v} \rightarrow \mathbf{v} + \boldsymbol{\chi} , \quad (2.30)$$

where  $\mathbf{v} = \dot{\mathbf{x}}$ , and  $\mathbf{n}$  and  $\boldsymbol{\chi}$  are constant in space. Correlation functions of  $\phi_\ell$  are further preserving rotational invariance. In the following, we describe the steps to compute the power spectrum and bispectrum of galaxies in the EFTofLSS at one loop in the presence of smooth or clustering quintessence. Our goal is to highlight the main difference with the original computations of [15], which are modifications of the time dependence of the EFTofLSS operators.

**Dark matter - quintessence effective fluid** The first step is to smooth all fields  $\phi \rightarrow \phi_\ell^{(\Lambda_s)}$  over a length scale  $\Lambda_s$  such that an EFT can be written for the resulting long-wavelength fluctuations on the scales where their variance are smaller than unity. For example, one can apply a sharp cutoff in Fourier space, namely imposing  $\phi_\ell(\mathbf{k}) = \phi(\mathbf{k})$  for  $|\mathbf{k}| < \Lambda_s^{-1}$ ,  $\phi_\ell(\mathbf{k}) = 0$  otherwise. Defining so a long-wavelength density  $\delta_\ell$  and momentum  $\mathbf{p}_\ell = \bar{\rho}_m(1 + \delta_\ell)\mathbf{v}_\ell$  of the adiabatic mode, as well as a long-wavelength gravitational potential  $\Phi_\ell$ , we obtain a smoothed version of the system of equations (continuity, Euler, and Poisson) governing the propagation of the long-wavelength fields [4, 34],<sup>4</sup>

$$\dot{\delta}_\ell + \frac{1}{a}C(a)\theta_\ell = -\frac{1}{a}\partial_i(\delta_\ell v_\ell^i) , \quad (2.31)$$

$$\dot{\theta}_\ell + H\theta_\ell + \frac{1}{a}\partial^2\Phi_\ell = -\frac{1}{a}\partial_i(v_\ell^j\partial_j v_\ell^i) - \frac{1}{a}\partial_i\left(\frac{1}{\rho_m}\partial_j\tau^{ij}\right) , \quad (2.32)$$

$$\partial^2\Phi_\ell = \frac{3}{2}\Omega_m\mathcal{H}^2\delta_\ell . \quad (2.33)$$

For clarity, the effects of modified gravity within the EFTofLSS are discussed in app. A.2, while the main text retains the standard Poisson equation. In smooth quintessence ( $c_s^2 \rightarrow 1$ ), the adiabatic mode are simply the matter fluctuations such that  $C \equiv 1$ , while in clustering quintessence ( $c_s^2 \rightarrow 0$ ), the adiabatic mode also includes dark energy fluctuations (2.24) such that  $C$  is given by (2.26). Upon smoothing, we consider, on the r.h.s. of (2.32), the divergence of a stress tensor  $\partial_j\tau^{ij}$  enclosing the effects of the short-wavelength fluctuations sourcing the long-wavelength fields [5]. In the following, we drop the lower-case index  $\ell$  to avoid clutter.

Leaving aside counterterms for now, *i.e.*, solutions generated from the sourcing of the Euler equation by the EFT expansion of  $\tau^{ij}$ , the perturbation theory contributions for  $\psi_\alpha \equiv (\delta_\ell, \theta_\ell)^T$  are obtained by solving recursively the system of equations (2.31) to (2.33). The  $n$ -th order solutions for the fields  $\psi_\alpha$  read

$$\psi_\alpha^{(n)}(\mathbf{k}, a) = \int \frac{d^3q_1}{(2\pi)^3} \cdots \frac{d^3q_n}{(2\pi)^3} (2\pi)^3 \delta_D(\mathbf{k} - \mathbf{q}_1 - \cdots - \mathbf{q}_n) K_\alpha(\mathbf{q}_1, \dots, \mathbf{q}_n, a) \delta_{\mathbf{q}_1}^{(1)}(a) \cdots \delta_{\mathbf{q}_n}^{(1)}(a) , \quad (2.34)$$

where  $\delta_D$  is the Dirac delta-distribution and  $\delta_{\mathbf{q}}^{(1)}(a)$  is the linearly-evolved adiabatic mode up to scale factor  $a$  evaluated at Fourier mode  $\mathbf{q}$ . Explicit expressions for the time-dependent Fourier

---

<sup>4</sup>Here we have again left out the curl component of the velocity from the presentation, although when computing the one-loop contributions to the bispectrum we are actually also solving for it [15].

kernels  $K_\alpha^{(n)}$  up to third order in clustering quintessence can be found in [44], and read schematically as

$$K_\alpha^{(n)}(\mathbf{q}_1, \dots, \mathbf{q}_n, a) = \sum_\sigma \Pi_\sigma(\mathbf{q}_1, \dots, \mathbf{q}_n) \mathcal{G}_\sigma^{(n),\alpha}(a) , \quad (2.35)$$

where we see that they can be decomposed into a sum of momentum-dependent functions  $\Pi_\sigma$  (whose form, universal, is dictated by the equivalence principle [45]) multiplied by time-dependent functions  $\mathcal{G}_\sigma^{(n),\alpha}$  that are found by solving for the Green's functions associated to the system of equations (2.31) to (2.33) [5, 31]. Smooth quintessence is recovered taking the limit  $C(a) \equiv 1$  in  $\mathcal{G}_\sigma^\alpha$  and taking further  $w = -1$  lands us in  $\Lambda$ CDM. Explicit expressions are given in app. A.1.

**Exact time dependence** An exact treatment of time dependence in the EFTofLSS contrasts with the standard approach based on the Einstein-de Sitter (EdS) approximation. In the latter, the time evolution of perturbations is approximated by simple powers of the growth factor  $D$ , as it would be in a matter-dominated Universe ( $\Omega_m \equiv 1$ ), *e.g.*,  $\delta_{\mathbf{k}}^{(n)}(a) \simeq D(a)^n \delta_{\mathbf{k}}^{(n)}(a_i)$ , where  $D$  is normalised at some initial time  $a_i$  (deep inside matter domination). This approximation has been shown to be highly accurate within  $\Lambda$ CDM and in smooth quintessence for the data volume of LSS Stage-4 surveys [46]. In the case of clustering quintessence, exact time dependence was discussed in ref. [44]. These previous analyses, based on the power spectrum, assumed a constant dark energy equation of state.

In this work, we explore general time-varying  $w(t)$  in light of the one-loop bispectrum of galaxies. Unlike the power spectrum, where deviations from the EdS approximation arise only at the loop level, the bispectrum is already affected at tree level (through  $\delta^{(2)}$ ). In the present cosmological analysis, we incorporate the exact time dependence in both the one-loop power spectrum and the tree-level contribution of the galaxy bispectrum. As we find that exact time dependence has a negligible impact on cosmological constraints (see sec. 4), we omit it in the loop contributions of the bispectrum.

**Galaxies** Positions of biased tracers (that we refer as galaxies) of the underlying dark matter - quintessence fluid, are what we are offered in LSS surveys — these are ultimately what we want to describe. At sufficiently long distances, we can again make use of the equivalence principle to write the most general expressions for the galaxy density in terms of all possible scalars constructed from the tidal field  $\partial_i \partial_j \Phi$  and spatial derivatives [47, 48, 7]. This expansion is integrated over the past lightcone within which galaxies form, and is evaluated along the fluid elements throughout their history flowing into the final observed positions [7, 49]. Leaving aside stochastic terms for now, the bias expansion of the galaxy density at final position  $\mathbf{x}$  and time  $t$  is given by

$$\delta_g(\mathbf{x}, t) = \sum_i \int^t dt' H(t') c_i(t, t') \mathcal{O}_i \left[ \frac{\partial_i \partial_j \Phi(\mathbf{x}_\mathbf{g}, t')}{H(t')^2}, \frac{\partial_i}{k_M} \right] , \quad (2.36)$$

where  $\mathcal{O}_i$  are all possible Galilean-invariant scalars built from powers of  $\partial_i \partial_j \Phi$  and spatial derivatives  $\partial_i$  (normalised by  $k_M$ , the spatial extension of the observed objects) that are evaluated at

the fluid element  $\mathbf{x}_\mathbf{f}$  defined from displacing recursively the position as

$$\mathbf{x}_\mathbf{f}(\mathbf{x}, a, a') = \mathbf{x} - \int_{a'}^a \frac{d\tilde{a}}{a\mathcal{H}(\tilde{a})} \mathbf{v}(\mathbf{x}_\mathbf{f}(\mathbf{x}, a, \tilde{a}), \tilde{a}) . \quad (2.37)$$

Note that for clustering quintessence, the bias expansion is constructed from the adiabatic mode. After Taylor expanding around  $\mathbf{x}$  to the relevant order in fields and accounting for the degeneracies, the galaxy density schematically reads as

$$\delta_g(\mathbf{x}, t) = \sum_i b_i(t) \mathcal{D}_i(t) \mathbb{C}_i(\mathbf{x}, t) , \quad (2.38)$$

where  $b_i$  are time-dependent free coefficients to adjust to the data,  $\mathcal{D}_i$  are calculable generalised growth functions, and  $\mathbb{C}_i$  are operators carrying the position dependence constructed from powers of  $\delta^{(1)}$  and derivatives. The time dependence of the operator  $\mathbb{C}_i$  at order  $n$  in perturbations is  $D(t)^n$ , such that in the EdS time approximation,  $\mathcal{D}_i(t) = 1$ . At nonlinear order ( $n \geq 2$ ),  $\mathcal{D}_i$  can take more complicated forms [50]. The bias expansion up to third order has been derived within the EdS approximation in [49, 51, 52], later with exact time dependence in [50] for  $\Lambda$ CDM and smooth quintessence, and finally in [44] for clustering quintessence (see also [53, 45]). Explicit expression for the galaxy density field can be found in app. A.

**Redshift-space distortions** Because galaxies and dark matter are comoving at large scales, their velocities are the same (up to higher-derivative terms). As shown in app. A, it is convenient to write  $\theta_g \equiv \theta$  in the form of (2.38) with specific values of the biases. For general cosmologies, those are calculable time-dependent functions identified with the ones appearing in the dark matter velocity expansion (2.35). This is important as galaxies are observed in redshift space where their positions are distorted by peculiar velocities along the line-of-sight  $\hat{z}$ . Upon this change of variables,

$$\mathbf{x} \rightarrow \mathbf{x} + \frac{\mathbf{v} \cdot \hat{z}}{\mathcal{H}} \hat{z} , \quad (2.39)$$

new terms are generated in the expansion of the galaxy density involving products of density and momentum operators [54, 15]. At lowest order in the Taylor expansion around  $\mathbf{x}$ , we have

$$\begin{aligned} \delta_{g,r}(\mathbf{x}) &= \delta_g(\mathbf{x}) + \partial_i \left( (1 + \delta_g(\mathbf{x})) \frac{\mathbf{v} \cdot \hat{z}}{\mathcal{H}} \hat{z}^i \right) + \dots \\ &= \delta_g(\mathbf{x}) + \frac{\hat{z}^i \hat{z}^j}{\mathcal{H} \rho_m} \partial_i p^j + \dots , \end{aligned} \quad (2.40)$$

where we remind that the momentum reads

$$\mathbf{p} = \bar{\rho}_m (1 + \delta) \mathbf{v} . \quad (2.41)$$

The final structure is similar to (2.38) but now with terms that are explicitly depending on the line-of-sight direction,

$$\delta_{g,r}(\mathbf{k}, t) = \sum_j \mu^{\nu_j} b_j^{\mathcal{G}}(t) \mathcal{D}_j(t) \mathbb{C}_j(\mathbf{k}, t) , \quad (2.42)$$

where  $\mu = \hat{k} \cdot \hat{z}$ ,  $\nu$ 's are some even integer powers, and we use a different index  $j$  compared to  $i$  in (2.38) to stress that the terms have been shuffled and redefined. In particular,  $b_j^{\mathcal{G}}$  symbolically represents that sometimes it is not a free bias coefficient but a calculable time function when  $\mathbb{C}_j$  stems from a product of momentum operators only. This means that thanks to redshift-space distortions, the (partial) degeneracies of the time-dependent growth functions with the galaxy biases  $b_i$  are further broken, thus allowing in principle for a measurements of their dependence — in particular on  $w(t)$ .

**Modified time dependence** To illustrate a nontrivial modification of the time dependence in the presence of dark energy, let us inspect a few contributions to  $\delta_g$  or  $\theta_g$  from (A.25) and (A.26). For example, the operator  $\mathbb{C}_{\delta,1}^{(2)}$  comes multiplied by a time function  $\mathcal{G}$  defined as

$$\mathcal{G}(a) = \frac{1}{D(a)} \int^a \frac{da'}{a'} \frac{f(a')}{C(a')}, \quad (2.43)$$

where  $f \equiv \frac{d \ln D}{d \ln a}$  is the growth rate. It is relevant only for the clustering case, as when  $C(a) \equiv 1$ , we have  $\mathcal{G}(a) \equiv 1$ . Another example comes from the contribution  $\frac{7}{2}(1 - \mathcal{G}_1^\theta) \mathbb{C}_{\delta,2}^{(2)}$  to  $\theta_g$ , relevant for both smooth and clustering quintessence. Because  $\mathbb{C}_{\delta,1}^{(2)}$  and  $\mathbb{C}_{\delta,2}^{(2)}$  are second order, we expect  $\mathcal{G}$  and  $\mathcal{G}_1^\theta$  to enter in the loop of the power spectrum (through the 22-diagram) and linearly in the tree-level bispectrum in redshift space. In fig. 2, we plot  $\mathcal{G}$  and  $\mathcal{G}_1^\theta$  as function of the redshift for  $w(z)$  given by the best fit found with the  $(w_0, w_a)$ -parametrisation in this work. For relative data uncertainties of  $\sim 10\%$ , we expect this rescaling of  $\sim 1\%$  (with respect to the EdS case)<sup>5</sup> on the leading redshift-space distortions in the bispectrum to be small.

**Counterterms** So far, we have only focus on the perturbation theory contributions. There are various counterterms to consider.

- Counterterms that arise from the expansion of  $\tau^{ij}$  in the r.h.s. of the smoothed Euler equation (2.32). This has nothing but the same structure written for the galaxy density (2.36) but equipped with  $\delta_{ij}$ , where we further allow for Galilean tensors under rotations of the  $i$  and  $j$  indices. The scale controlling this expansion,  $k_{\text{NL}}^{-1}$ , corresponds roughly to when the variance of the unsmoothed field becomes nonlinear, *i.e.*,  $\sim \mathcal{O}(1)$ . There are two types of contributions that arise from the expansion of  $\tau^{ij}$ : either terms constructed from the tidal tensor  $\partial_i \partial_j \Phi$ , or stochastic terms. We discuss the latter below and we focus now on the former, that we call response terms. They start contributing at third order in perturbations, since it is  $\partial_i \partial_j \tau^{ij}$  that sources the Euler equation (2.32). The leading response  $\sim \partial^2 \delta^{(1)} / k_{\text{NL}}^2$  is degenerate with the leading spatial derivative correction  $\sim \partial^2 \delta^{(1)} / k_{\text{M}}^2$ , where  $k_{\text{M}}^{-1}$  represents the spatial extension of the galaxy, roughly the size of the host halo. We comment on the next-to-leading response terms below.

<sup>5</sup>For clustering quintessence, when referring to the EdS approximation we further assume  $C = 1$  beyond linear order [15], yielding  $\mathcal{G} = 1$ .

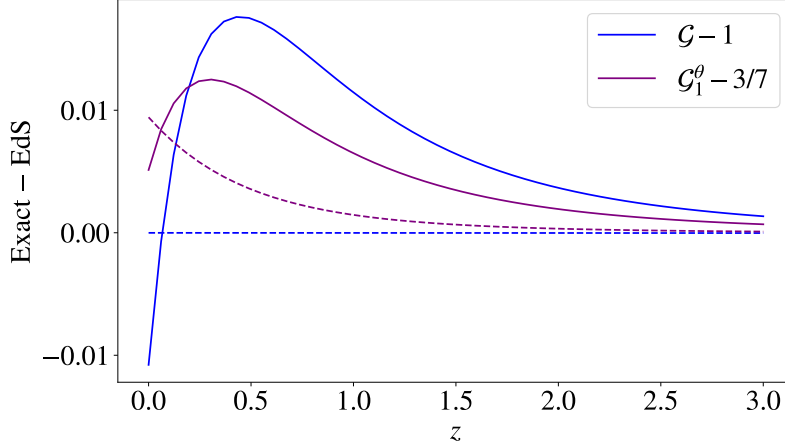


Figure 2: Relative difference of the nonlinear time functions  $\mathcal{G}$  and  $\mathcal{G}_1^\theta$  between their exact values and their EdS approximations (using the best fit values found in this work in  $w_0w_a$ CDM). The continuous and dashed lines are for  $c_s^2 \rightarrow 0$  and  $c_s^2 \rightarrow 1$ , respectively.

In presence of modified gravity, we have to further consider the Galilean-invariant tensors  $\partial_i\partial_j\Psi$  and  $\partial_i\partial_j\pi$  when expanding  $\tau^{ij}$  to account all possible feedbacks of short-wavelength fluctuations on the long ones [34]. However, in the limiting cases that we study, those are constrained such that they do not lead to new terms in the EFT expansions other than the ones generated by  $\partial_i\partial_j\Phi$  (see (2.20) and (2.22)).

- The expansion of the density field in redshift space (2.40) involves (products of) the momentum. Because the momentum is a composite operator (2.41), it has to be renormalised by adding suitable counterterms to remove its UV-sensitivity. Those are precisely provided by the expansion of  $\tau^{ij}$  through the Euler equation (2.32). Importantly, some of the next-to-leading response terms entering the momentum renormalisation are not present in the bias expansion (2.38) up to forth order [44]. This is because the spatial Green's function from the Poisson equation is nonlocal, *i.e.*,  $\Phi \propto \partial^{-2}\delta$ , and is not cancelled when considering the traceless part of  $\partial_i\partial_j\Phi$  contributing to the vector part of the momentum  $p_V^i = \epsilon^{ijk}\partial_j p^k$  (related to the vorticity).<sup>6</sup> As a consequence, appear in the density in redshift space at forth order non-locally-contributing counterterms [44]. Products involving momentum operators in the redshift-space expansion are renormalised by a new scale  $k_R^{-1}$  [55, 56]. All response terms are found to be necessary and sufficient to renormalise the one-loop contributions in the power spectrum and bispectrum involving  $\delta_g^{(3)}$  or  $\delta_g^{(4)}$  with a self-loop [44].
- Stochastic contributions arising in the expansions of both the galaxy density field and the stress tensor. Those are quantities  $\epsilon$  and  $\epsilon_{ij}$ , whose correlation functions can be written as an expansion in powers of  $\partial_i$  of terms invariant by rotations [57, 44]. In the expansion of

<sup>6</sup>Here  $\epsilon^{ijk}$  is the three-dimensional totally antisymmetric Levi-Civita symbol.



the galaxy density, their size is controlled by  $1/\bar{n}_g$ , where  $\bar{n}_g$  is the average number density of observed galaxies, while in the stress tensor, their size is controlled by  $1/\bar{n}_{\text{NL}} \sim k_{\text{NL}}^3$ , the occupation number density in regions of size  $\sim k_{\text{NL}}^{-1}$ . Analogously as the response terms, there are non-locally contributing stochastic terms at next-to-leading order [44].

**Observables** We consider the two- and three-point function in Fourier space, defined as

$$\langle \delta_{g,r}(\mathbf{k}) \delta_{g,r}(\mathbf{k}') \rangle = (2\pi)^3 \delta_D(\mathbf{k} + \mathbf{k}') P(k, \mu) , \quad (2.44)$$

$$\langle \delta_{g,r}(\mathbf{k}_1) \delta_{g,r}(\mathbf{k}_2) \delta_{g,r}(\mathbf{k}_3) \rangle = (2\pi)^3 \delta_D(\mathbf{k}_1 + \mathbf{k}_2 + \mathbf{k}_3) B(k_1, k_2, k_3, \mu, \phi) . \quad (2.45)$$

The Dirac delta-distributions reflect translation invariance. Rotation invariance, partially broken in redshift space, implies that the power spectrum  $P$  is a function of the norm  $k$  and the cosine  $\mu = \hat{k} \cdot \hat{z}$ . As for the bispectrum  $B$ , we can express it with the three sides of the triangle formed by  $(\mathbf{k}_1, \mathbf{k}_2, \mathbf{k}_3)$ , the cosine  $\mu \equiv \mu_1 = \hat{k}_1 \cdot \hat{z}$ , and the azimuthal angle  $\phi$  [58]. At the one-loop precision, the power spectrum  $P$  and bispectrum  $B$  of galaxies in redshift space read [44]

$$P = P_{11} + (P_{13} + P_{13}^{ct}) + (P_{22} + P_{22}^\epsilon) , \quad (2.46)$$

$$B = B_{211} + (B_{321}^{(II)} + B_{321}^{(II),ct}) + (B_{411} + B_{411}^{g,r,ct}) + (B_{222} + B_{222}^{g,r,\epsilon}) + (B_{321}^{(I)} + B_{321}^{(I),\epsilon}) , \quad (2.47)$$

where in each loop diagram the UV-sensitivity is absorbed by the appropriate counterterms mentioned above. For our data analysis, we consider the multipoles ( $\ell = 0, 2$ ) of the power spectrum and the monopole of the bispectrum,

$$P_\ell(k) = \frac{2\ell + 1}{2} \int_{-1}^{+1} d\mu P(k, \mu) \mathcal{L}_\ell(\mu) , \quad (2.48)$$

$$B_0(k_1, k_2, k_3) = \frac{1}{4\pi} \int_{-1}^{+1} d\mu \int_0^{2\pi} d\phi B(k_1, k_2, k_3, \mu, \phi) , \quad (2.49)$$

where  $\mathcal{L}_\ell$  is the Legendre multipole of order  $\ell$ . In fig. 3, we show the relative difference in the power spectrum and bispectrum when accounting for the modified time dependence in the presence of dark energy. Compared to current data uncertainties, the EdS approximation appears likely to be under control for the best fit of  $w(z)$  obtained in this work — we nevertheless explicitly check its impact on the constraints in sec. 4. In contrast, the difference between the  $c_s^2 \rightarrow 0$  and  $c_s^2 \rightarrow 1$  limits is significant and can impact the constraints, as we find in sec. 4.

**IR-resummation** The variance of long-wavelength displacements  $\mathbf{s}_\ell$  is close to unity for scales around the BAO peak, making the expansion of the density field converge slowly in this parameter [59, 6]. To cure this limitation, one can displace the position of the galaxies with the linear displacement, which captures most of the large-scale bulk flow [60]. The linear displacement is

$$s_i^{(1)}(\mathbf{x}, a) = \int^{\ln a} \frac{d \ln a'}{\mathcal{H}(a')} v_i^{(1)}(\mathbf{x}, a') = -\mathcal{G}(a) \frac{\partial_i}{\partial^2} \delta^{(1)} , \quad (2.50)$$



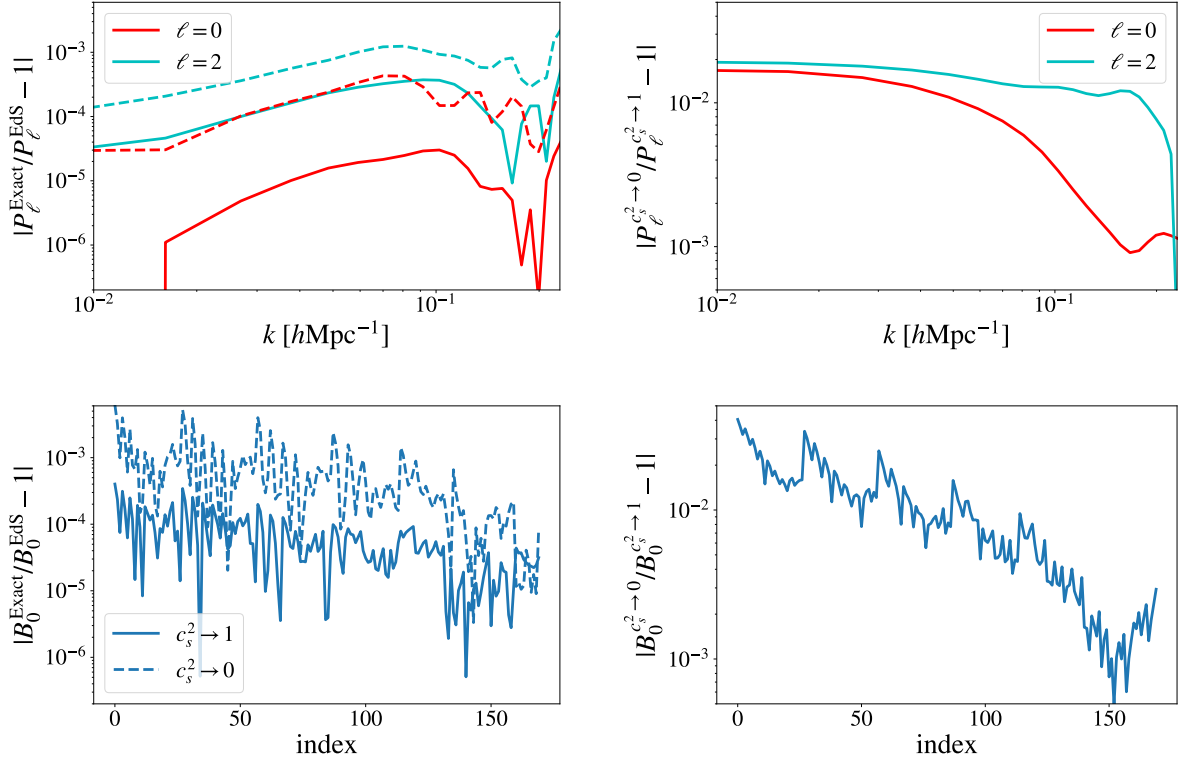


Figure 3: Relative difference on the power spectrum multipoles (*upper panels*) and bispectrum monopole (*bottom panels*) at fixed cosmology ( $\sim w_0 = -0.8, w_a = -0.6$ ) for various setups considered in this work. The  $x$ -axes in the bottom panel correspond to the triangle bin indices. *Left panels*: Exact-time dependence vs. EdS approximation for  $c_s^2 \rightarrow 1$  (solid line) or  $c_s^2 \rightarrow 0$  (dashed line). *Right panels*:  $c_s^2 \rightarrow 1$  vs.  $c_s^2 \rightarrow 0$ .

where in the second equality we have used  $v_i^{(1)} = \frac{\partial_i}{\partial^2} \theta^{(1)} = -\frac{\mathcal{H}f}{C} \frac{\partial_i}{\partial^2} \delta^{(1)}$  following the linearised continuity equation (2.31), together with the definition (2.43). The power spectrum and bispectrum are therefore IR-resummed as usual following [55, 61, 17] but with the replacement  $P_{\text{lin}} \rightarrow \mathcal{G}^2 P_{\text{lin}}$  in the exponent of the damping [44]. This is relevant only in clustering quintessence as we remind that  $\mathcal{G} = 1$  if  $C = 1$ . We find that setting  $\mathcal{G}$  in eq. (2.50) to its values associated with the best fit found in this work in  $w_0 w_a$ CDM leads to an extra relative damping of  $\sim 0.1\%$ . Thus, in practice, the modification of the BAO features from the presence of clustering dark energy is negligible.

### 3 Inference setup

We aim to find an appropriate way to bridge candidate models of dark energy that can produce departure from  $w = -1$ , with what the data can tell us. Because there is no consensus on what dark energy is, we make use of several parametric forms for  $w(t)$  in our search. The various forms for the equation of state of dark energy  $w(t)$  considered in this work are presented in sec. 3.1. In sec. 3.2, we then describe the datasets we use to constrain them. In sec. 3.3 we give some extra

details on the likelihood and prior used to analyse the power spectrum and bispectrum of galaxies.

### 3.1 Probing evolution in the dark

To probe potential evolution in dark energy equation of state, we consider the following parametrisations for  $w(a)$ :

- $w(a) = w_0$ : How on average is the cosmic acceleration not driven by  $\Lambda$ , *i.e.*, is  $w \neq -1$ ? From a UV perspective, this raises the following question: if we give up  $\Lambda$ , how flat must the scalar field potential remain throughout cosmic history? This naturally leads to the question of the extent to which cosmological data constrain  $w$  to be close to (or far from)  $-1$ . Pragmatically, we want to get a sense of the overall data sensitivity on  $w$ .  $w_0$ CDM was explored in ref. [18] in light of the galaxy bispectrum, yielding  $w_0 = -0.975 \pm 0.019$  at 68%CL using a similar dataset as the baseline considered in this work (see below). Given the high sensitivity to  $w$ , this motivates us to explore more general parametric forms.
- $w(a) = w_0 + w_a(1 - a)$ : Commonly referred to as the Chevalier-Polarsky-Linder (CPL) parametrisation [62, 63], it can be thought as the first (linear) correction in a Taylor expansion of  $w(a)$  around the scale factor today  $a_0 \equiv 1$ .  $w_0w_a$ CDM is explored in sec. 4 in light of various dataset combinations and analysis setups. To help visualise and understand our results, we also use an equivalent, more interpretable, parametric form,  $w_\star = w_0 + w_a(1 - a_\star)$ , where  $a_\star$  is the pivot epoch at which  $w$  is best constrained throughout cosmic history (see sec. 5.1).
- Beyond-CPL parametrisation: Is the data sensitive to more subtle time variations? We investigate this question in details in sec. 5.1 and app. C, using a piece-wise  $w(z)$  in redshift bins, arbitrarily generalisable by increasing the number of bins upon saturating the  $\chi^2_{\min}$ . If no particular model of dark energy is assumed, a general flexible parametric form allows to assess the consistency with  $\Lambda$  in a data-driven way.

### 3.2 Datasets and inference framework

In our cosmological inference, we consider different combinations of the following datasets:

- **Planck**: The temperature, polarization and lensing power spectrum data from *Planck* PR3. We use the **Commander** likelihood for low- $l$  TT, the **Simall** likelihood for EE, and the **Plik** likelihood for high- $l$  TT, EE, TE [64], as well as the reconstructed gravitational lensing potential power spectrum from [65].<sup>7</sup>
- **EFTBOSS**: The full-shape analysis of the power spectrum and bispectrum of BOSS Luminous Red Galaxies (LRG) from the EFTofLSS at one loop. The SDSS-III BOSS DR12 galaxy sample data are described in ref. [19]. The power spectrum and bispectrum measurements,

---

<sup>7</sup>We checked that the difference in the lensing likelihood compared to that used in the joint analysis of DESI Y1 [1] results in a negligible impact on the posteriors.

obtained in ref. [17], are from BOSS catalogs DR12 (v5) combined CMASS-LOWZ<sup>8</sup> [66], and are divided in two redshift bins (and four sky-cuts): low- $z$ ,  $0.2 < z < 0.43$  ( $z_{\text{eff}} = 0.32$ ), and high- $z$ ,  $0.43 < z < 0.7$  ( $z_{\text{eff}} = 0.57$ ), with north and south galactic skies for each. The covariance, including the correlation between power spectrum and bispectrum, is measured through 2048 Patchy mocks [67], while the window function is measured from `fkpwin`<sup>9</sup> [68]. More details are provided in sec. 3.3.

- **ext-BAO:** The angle-averaged distance ratio  $D_V/r_s$  extracted from baryon acoustic oscillations (BAO) at  $z = 0.106$  from 6dFGS [26] and at  $z = 0.15$  from SDSS DR7 [27], as well as the joint constraints from eBOSS DR14 Ly- $\alpha$  absorption auto-correlation at  $z = 2.34$  and cross-correlation with quasars at  $z = 2.35$  [20, 69].
- **DESI-BAO:** The DESI Y1 BAO data [1], which include the distance ratios  $D_M/r_s$  and  $D_H/r_s$  at  $z = 0.51$  (LRG1),  $0.706$  (LRG2),  $0.930$  (LRG3+ELG1),  $1.317$  (ELG2), and  $2.33$  (Ly- $\alpha$  QSO), as well as  $D_V/r_s$  at  $z = 0.295$  (BGS), and  $1.491$  (QSO).
- **PanPlus:** Pantheon+ catalog of uncalibrated luminosity distance of SNeIa in the range  $0.01 < z < 2.26$  [23].
- **Union3:** Union3 catalog of uncalibrated luminosity distance of SNeIa in the range  $0.05 < z < 2.26$  [24].
- **DESY5:** DES year 5 catalog of uncalibrated luminosity distance of SNeIa in the range  $0.10 < z < 1.13$ , combined with an external sample of SNeIa at low redshifts  $0.024 < z < 0.10$  [25].<sup>10</sup>

When inferring cosmological parameters from various combinations of the datasets above, we simply add their likelihoods together, marginalising over the nuisance parameters upon sampling. In particular, and in line with the literature, we neglect the small correlations between *Planck* lensing and the integrated Sachs-Wolfe effects with galaxy clustering data.

**DESI-BAO + EFTBOSS/ $r_s^{\text{marg}}$**  DESI Y1 and SDSS/BOSS share a substantial overlap in their observed sky coverage. Specifically, 27% of DESI BGS and LRG1 galaxies, along with 9% of DESI LRG2 galaxies, were already observed by BOSS [71]. To avoid potential correlations when combining these two datasets, the information from the sound horizon ( $r_s$ ) is taken from DESI-BAO while being properly marginalised in EFTBOSS full-shape analysis, following the methodology of refs. [72, 73]. Explicitly, when jointly fitting these datasets, we further marginalise over a nuisance parameter,  $\alpha_{r_s}$ . This parameter modifies the EFT predictions for the BOSS power spectrum and bispectrum by scaling the BAO wiggles through the (input) linear matter power spectrum as

$$P_{\text{lin}}(k) \rightarrow P_{\text{nw}}(k) + P_{\text{w}}(\alpha_{r_s} k) , \quad (3.1)$$

<sup>8</sup>Publicly available at <https://data.sdss.org/sas/dr12/booss/lss/>.

<sup>9</sup><https://github.com/pierrexyz/fkpwin>

<sup>10</sup>For Union3 and DESY5, we have adapted the public Cobaya [70] likelihoods to `Montepython-v3`.

thus effectively marginalising over the sound horizon information. Here,  $P_{\text{nw}}$  and  $P_{\text{w}}$  represent the no-wiggle and wiggle components of the linear power spectrum, split following the method of ref. [74].

**Inference framework** To sample posteriors from the likelihoods of the datasets above, we run Markov chain Monte Carlo (MCMC) chains through the Metropolis-Hasting algorithm implemented in `Montepython-v3`<sup>11</sup> [75, 76], interfaced with the Boltzmann code `class`<sup>12</sup> [77, 78] for background and linear cosmological quantities, and `PyBird` for computing the nonlinear galaxy power spectrum and bispectrum<sup>13</sup> [61]. When marginalising over EFTofDE parameters described in sec. 2.1, we use a modified version of `hi_class`<sup>14</sup> [79, 80] to compute the linear cosmological observables in the EFTofDE, while using `PyBird`<sup>15</sup> with modified nonlinear time functions (see sec. 2.3).

For all analyses performed in this work, we impose large flat priors on the  $\Lambda$ CDM cosmological parameters  $\{\omega_b, \omega_{\text{cdm}}, h, \ln(10^{10} A_s), n_s, \tau_{\text{reio}}\}$ , as well as on the dark energy equation-of-state parameters described in sec. 3.1. Following *Planck* convention for neutrinos, we consider two massless neutrinos and one massive neutrino, with  $m_\nu = 0.06\text{eV}$ . We consider that our chains have converged when the Gelman-Rubin criterion  $R - 1 < 0.05$ . We use simulated annealing from `Procoli`<sup>16</sup> [82] to find the maximum a posteriori (that we also refer as the best fit). Finally, marginalised posteriors and credible intervals are obtained using `Getdist`<sup>17</sup> [83].

### 3.3 EFT likelihood

We analyse the full-shape power spectrum ( $P$ ) and bispectrum ( $B$ ) of BOSS galaxies in redshift space based on the one-loop predictions from the EFTofLSS presented in sec. 2.3. Additional modelling required to make contact with observations — such as Alcock-Paczynski distortions, window functions, and binning — have been thoroughly tested and detailed in refs. [10, 17].

**Likelihood, data specification, and covariance** The likelihood used in this work follows the methodology outlined in ref. [17]. The BOSS survey data are divided into two redshift bins: low- $z$  ( $0.2 < z < 0.43$  ( $z_{\text{eff}} = 0.32$ )) and high- $z$  ( $0.43 < z < 0.7$  ( $z_{\text{eff}} = 0.57$ )), each further split into north and south galactic cuts, resulting in four independent sky regions. For each region, we analyse the monopole and quadrupole of the power spectrum, and the monopole of the bispectrum, measured in ref. [17] using standard FKP-like estimators [84–86].<sup>18</sup> The chosen scale ranges are  $k_{\text{min}} = 0.01 h \text{Mpc}^{-1}$  and  $k_{\text{max}} = 0.20/0.23 h \text{Mpc}^{-1}$  for low- $z$ /high- $z$  skies, based on

<sup>11</sup>[https://github.com/brinckmann/montepython\\_public](https://github.com/brinckmann/montepython_public)

<sup>12</sup><http://class-code.net/>

<sup>13</sup><http://github.com/pierrexyz/pybird/>

<sup>14</sup>[https://miguelzuma.github.io/hi\\_class\\_public/](https://miguelzuma.github.io/hi_class_public/)

<sup>15</sup>Adapted from <https://github.com/billwright93/pybird> [81]

<sup>16</sup><https://github.com/tkarwal/procoli>

<sup>17</sup><https://getdist.readthedocs.io/en/latest/>

<sup>18</sup><https://github.com/hectorgil/Rustico>

prior estimates of the theoretical error relative to BOSS uncertainties (see below). For each sky region, we construct a data vector  $\mathcal{D}_\alpha$  consisting of all observables, where  $\alpha$  indexes multipoles, power spectrum  $k$ -bins, or bispectrum triangle bins. The covariance matrix  $C_{\alpha\beta}$  is estimated from the scatter across 2048 Patchy mocks [67], with the inverse covariance corrected using the Hartlap factor [87]. At each likelihood evaluation, the theory model vector  $m_\alpha(\theta)$  is computed according to the predictions of sec. 2.3, where  $\theta$  contains the cosmological and EFTofLSS parameters. The likelihood function  $\mathcal{L}$  for each sky is given by:

$$-2 \ln \mathcal{L}(\mathcal{D}|\theta) = \sum_{\alpha,\beta} (\mathcal{D}_\alpha - m_\alpha(\theta)) C_{\alpha\beta}^{-1} (\mathcal{D}_\beta - m_\beta(\theta)) . \quad (3.2)$$

**Prior and marginalisation** Details on priors and analytical marginalisation can be found in ref. [17]. For the predictions to remain within the validity of perturbation theory, EFT parameters are expected to be  $\mathcal{O}(1)$ . Thus, they are marginalized over using Gaussian priors centred at zero with a width of  $\sim 2$ , except for  $b_1$ , which is constrained to be positive via an equivalent log-normal prior. To account for variations across different sky regions, separate sets of EFT parameters are assigned for each region, incorporating correlations due to redshift evolution and north-south observational differences. Specifically, EFT parameters are expected to vary by at most 10% between north and south regions within the same redshift bin, and by 20% between the low- $z$  and high- $z$  bins within the same hemisphere. This is enforced through a multivariate Gaussian prior. Since our primary focus is on cosmological parameters, we analytically marginalise over the EFT parameters that enter linearly in the predictions (and quadratically in the likelihood) using Gaussian integral properties. This significantly reduces computational cost, as only three EFT parameters —  $b_1, b_2$ , and  $b_5$  (following the notation of ref. [15]) — need to be explicitly sampled, out of a total of 41 per sky. For the characteristic scales governing the EFTofLSS expansions described in sec. 2.3, we set  $k_{\text{NL}} = k_{\text{M}} = 0.7 \ h \text{ Mpc}^{-1}$  and  $k_{\text{R}} = 0.25 \ h \text{ Mpc}^{-1}$ , while adopting a mean galaxy number density of  $\bar{n}_g = 4 \cdot 10^{-4} (\text{Mpc}/h)^3$ . In sec. 4.2, we verify that our prior choice has a negligible impact on the cosmological constraints by increasing the prior width by a factor of 2 and by checking the distance of the posterior mean with the maximum a posteriori estimate.

**Validations** Extensive tests of the power spectrum and bispectrum have been performed using high-fidelity simulations with their  $k$ -reach further assessed using perturbative arguments [88, 10, 89, 56, 46, 17]. In particular, the BOSS LRG power spectrum likelihood used in this work has been validated against the following  $N$ -body simulations with various galaxy-to-halo connection models: the BOSS lettered challenge [10, 90], the PT blind challenge [88], with additional tests in extended cosmologies or alternative setups in refs. [61, 44, 56, 91, 46, 92]. The pipeline has also been tested using eBOSS quasars and ELGs against EZmocks [13, 93]. Finally, the  $P + B$  likelihood for BOSS has been validated against the Nseries and Patchy mocks in ref. [17], which incorporate realistic observational effects such as lightcone evolution and sky footprints.

## 4 Cosmological results

In this section, we present our cosmological results for the dark energy equation of state  $w(t)$  parametrised by  $(w_0, w_a)$ , using the theoretical developments presented in sec. 2 together with the inference setup laid in sec. 3. Our main results are presented in sec. 4.1 with several combinations of data, before investigating in sec. 4.2 where does the preference for evolving dark energy comes from in our analysis. We complete our analysis of  $w_0w_a$ CDM by releasing the curvature in sec. 4.3 or EFTofDE parameters in sec. 4.4.

### 4.1 $w_0w_a$ CDM

Smooth quintessence ( $c_s^2 \rightarrow 1$ )	$w_0$	$w_a$	$p > \Lambda$	$\Delta\chi^2$
<i>Planck</i> + PanPlus + ext-BAO	$-0.856 \pm 0.085$	$-0.60^{+0.43}_{-0.37}$	$1.1\sigma$	-2.5
<i>Planck</i> + PanPlus + DESI-BAO	$-0.821 \pm 0.063$	$-0.77 \pm 0.27$	$2.5\sigma$	-8.9
<i>Planck</i> + ext-BAO + EFTBOSS	$-0.724^{+0.087}_{-0.11}$	$-0.91^{+0.42}_{-0.33}$	$0.0\sigma$	0.0
<i>Planck</i> + PanPlus + ext-BAO + EFTBOSS	$-0.844 \pm 0.055$	$-0.53^{+0.26}_{-0.23}$	$2.6\sigma$	-9.2
<i>Planck</i> + Union3 + ext-BAO + EFTBOSS	$-0.735^{+0.073}_{-0.085}$	$-0.87^{+0.35}_{-0.29}$	$3.4\sigma$	-14.5
<i>Planck</i> + DESY5 + ext-BAO + EFTBOSS	$-0.776 \pm 0.063$	$-0.76^{+0.29}_{-0.27}$	$3.7\sigma$	-16.8
Clustering quintessence ( $c_s^2 \rightarrow 0$ )	$w_0$	$w_a$	$p > \Lambda$	$\Delta\chi^2$
<i>Planck</i> + PanPlus + ext-BAO	$-0.856 \pm 0.085$	$-0.60^{+0.43}_{-0.37}$	$1.1\sigma$	-2.5
<i>Planck</i> + PanPlus + DESI-BAO	$-0.821 \pm 0.063$	$-0.77 \pm 0.27$	$2.5\sigma$	-8.9
<i>Planck</i> + ext-BAO + EFTBOSS	$-0.679^{+0.091}_{-0.11}$	$-1.15^{+0.42}_{-0.35}$	$0.6\sigma$	-1.3
<i>Planck</i> + PanPlus + ext-BAO + EFTBOSS	$-0.809^{+0.053}_{-0.061}$	$-0.72^{+0.28}_{-0.25}$	$2.8\sigma$	-10.3
<i>Planck</i> + Union3 + ext-BAO + EFTBOSS	$-0.692 \pm 0.078$	$-1.10 \pm 0.33$	$3.6\sigma$	-16.0
<i>Planck</i> + DESY5 + ext-BAO + EFTBOSS	$-0.739 \pm 0.061$	$-0.97^{+0.30}_{-0.27}$	$3.9\sigma$	-18.2
<i>Planck</i> + PanPlus + DESI-BAO + EFTBOSS/ $r_s^{\text{marg}}$	$-0.789 \pm 0.050$	$-0.80^{+0.25}_{-0.22}$	$3.7\sigma$	-16.9
<i>Planck</i> + Union3 + DESI-BAO + EFTBOSS/ $r_s^{\text{marg}}$	$-0.677 \pm 0.075$	$-1.14^{+0.33}_{-0.29}$	$3.8\sigma$	-17.7
<i>Planck</i> + DESY5 + DESI-BAO + EFTBOSS/ $r_s^{\text{marg}}$	$-0.726 \pm 0.060$	$-1.00^{+0.30}_{-0.25}$	$4.4\sigma$	-22.9

Table 2: 68% credible intervals of  $w_0$  and  $w_a$ , as well as the preference over  $\Lambda$  ( $p > \Lambda$ ) and the associated  $\Delta\chi^2$ , obtained within  $w_0w_a$ CDM for both smooth and clustering quintessence across various datasets, varying galaxy clustering (ext-BAO, ext-BAO + EFTBOSS, DESI-BAO, or DESI-BAO + EFTBOSS/ $r_s^{\text{marg}}$ ) and supernova (PanPlus, Union3 or DESY5) data.

**Baseline ‘pre-DESI’ dataset** In fig. 4, we show the 2D posterior distributions in the  $w_0 - w_a$  plane for the  $w_0w_a$ CDM model, while the 1D and 2D posterior distributions for the whole parameter space are shown in fig. 15 of app. B. In these figures, we consider the *Planck* + PanPlus + ext-BAO + EFTBOSS dataset, for the two phenomenologically-distinct limits of the dark energy fluctuations identified in sec. 2.2, *i.e.*, the smooth ( $c_s^2 \rightarrow 1$ ) and clustering ( $c_s^2 \rightarrow 0$ ) quintessence. The 68%-credible intervals and the best fit values are given in tab. 3 of app. B, together with the  $\Delta\chi^2$  and the  $\sigma$ -deviation from  $\Lambda$ CDM.

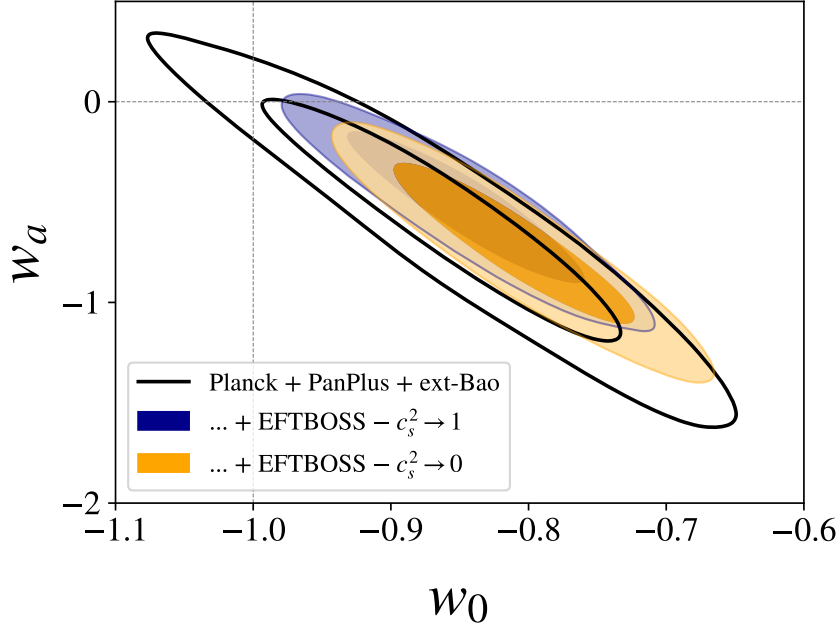


Figure 4: **Baseline constraints on  $(w_0, w_a)$  from pre-DESI data** — 2D posterior distributions of  $(w_0, w_a)$  from *Planck* + PanPlus + ext-BAO + EFTBOSS within  $w_0w_a$ CDM for both smooth and clustering quintessence. Constraints obtained without EFTBOSS are shown for comparison.

Within  $w_0w_a$ CDM, we obtain, at 68%CL,  $w_0 = -0.844 \pm 0.055$  and  $w_a = -0.53^{+0.26}_{-0.23}$  in smooth quintessence, and  $w_0 = -0.809^{+0.053}_{-0.061}$  and  $w_a = -0.72^{+0.28}_{-0.25}$  in clustering quintessence. Compared to the results without EFTBOSS, yielding  $w_0 = -0.856 \pm 0.085$  and  $w_a = -0.60^{+0.43}_{-0.37}$ , the uncertainties are improved by  $\sim 35\%$ . In light of these results, we can make several observations:

- For the dataset combination considered, *Planck* + PanPlus + ext-BAO + EFTBOSS, we find a preference for evolving dark energy over  $\Lambda$  at  $2.6\sigma$  and  $2.8\sigma$  whether  $c_s^2 \rightarrow 1$  or  $c_s^2 \rightarrow 0$  is considered, corresponding to  $\Delta\chi^2_{\min} = -9.2$  and  $\Delta\chi^2_{\min} = -10.3$ , respectively.
- The preferences arise only with the inclusion of the bispectrum in EFTBOSS (carefully studied in sec. 4.2). Without this contribution, the significance decreases to  $1.4\sigma$  for  $c_s^2 \rightarrow 1$  and  $1.5\sigma$  for  $c_s^2 \rightarrow 0$ .
- Our findings, relying on pre-DESI clustering data, are consistent with DESI Y1 results, that yield a  $2.5\sigma$  preference over  $\Lambda$ CDM when combined with *Planck* and PanPlus [3], in the same preferred region as displayed in fig. 6. While posteriors in the  $w_0 - w_a$  plane are consistent at  $\sim 0.5\sigma$ , our 2D constraints are approximately 35% (25%) tighter for  $c_s^2 \rightarrow 1$  ( $c_s^2 \rightarrow 0$ ) compared to those from DESI BAO [1], and comparable to those from DESI FS + BAO, where FS stands for the full-shape power spectrum [3].<sup>19</sup>

<sup>19</sup>Here and throughout the paper, comparisons of credible region areas in the  $w_0 - w_a$  plane are based on the ratio of the dark energy Figure of Merit (FoM) [94, 3]. Especially, we use the fact that the  $\text{FoM} \propto |\det C|^{-1/2}$ , where  $C$  corresponds to the  $2 \times 2$  covariance matrix of  $(w_0, w_a)$ .



- Constraints on  $(w_0, w_a)$  depend not only on the background but also on the propagation of dark energy perturbations — controlled by  $c_s^2$  — affecting clustering differently, as anticipated in sec. 2.2. Our results are further discussed in light of the stability of dark energy fluctuations in sec. 5.3.

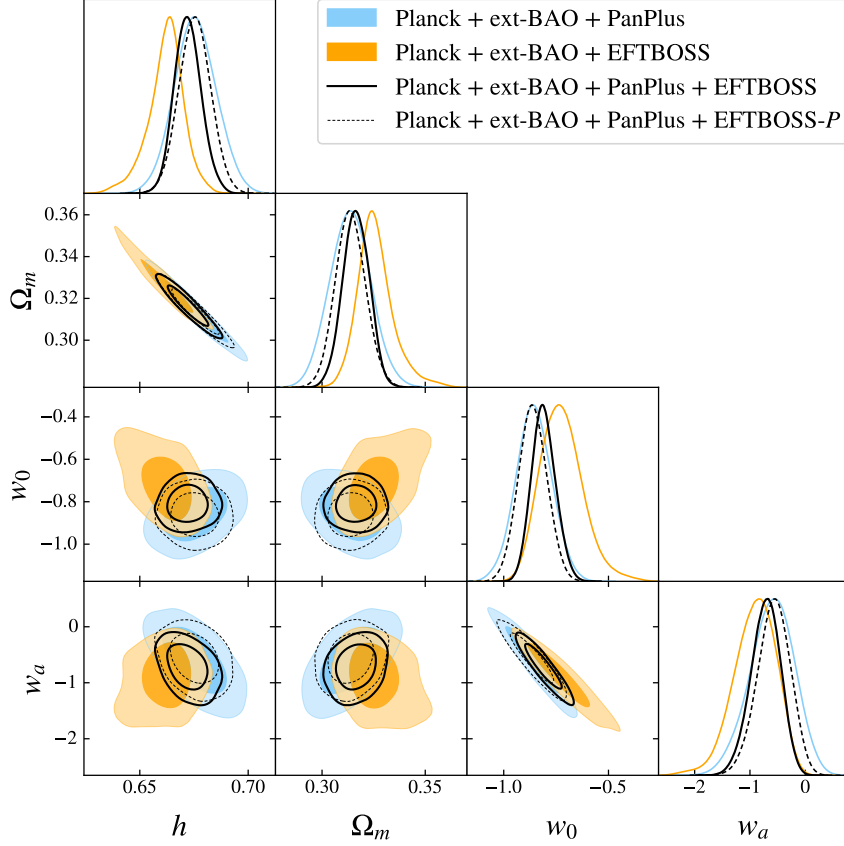


Figure 5: **Breaking degeneracies between PanPlus and EFTBOSS** — 2D posterior distributions of  $(w_0, w_a)$  from *Planck* + ext-BAO combined with PanPlus, EFTBOSS, or PanPlus + EFTBOSS, within  $w_0 w_a$ CDM for clustering quintessence. For comparison, we show *Planck* + ext-BAO + PanPlus + EFTBOSS with the contribution of the power spectrum only for the latter.

**Breaking degeneracies** In tab. 2, we report the preference for  $(w_0, w_a)$  over  $\Lambda$  (and the associated  $\Delta\chi^2$ ) for several dataset. Interestingly, the combinations of *Planck* + ext-BAO with either PanPlus or EFTBOSS do not show any preference for evolving dark energy. Yet, the preference arises when PanPlus and EFTBOSS are combined, implying that some degeneracies are broken. In fig. 5, we show how the degeneracies in the  $h - w_0/w_a$  and  $\Omega_m - w_0/w_a$  planes are orthogonal between PanPlus and EFTBOSS. The combination of both thus allows to break those degeneracies efficiently, leading to a strong constraint in the  $w_0 - w_a$  plane, which is 1.9 (2.2) times better than the dataset including PanPlus (EFTBOSS) only. In addition, the inclusion of EFTBOSS pulls



the contours towards small  $h$  and large  $\Omega_m$ , leading to an increase in  $w_0$  and a decrease in  $w_a$  due to their geometrical degeneracies in the angular diameter distance. Anticipating the results of sec. 4.2, we can see that the analysis with the power spectrum only is less able to break those degeneracies and prefers higher values of  $h$  and smaller values of  $\Omega_m$ .

**Impact of DESI BAO data** In the top left panel of fig. 1, we display, for clustering quintessence, the 2D posterior distributions in the  $w_0$ – $w_a$  plane from *Planck* + PanPlus + ext-BAO + EFTBOSS and *Planck* + PanPlus + DESI-BAO + EFTBOSS/ $r_s^{\text{marg}}$ , where the sound horizon information is marginalised in the latter (see sec. 3.2). The corresponding 68% credible intervals of  $w_0$  and  $w_a$  along with the preference over  $\Lambda$  (and the associated  $\Delta\chi^2$ ) are reported in tab. 2. Posteriors of the scaling parameter  $\alpha_{r_s}$  are shown in app. B. The preference for evolving dark energy increases from  $2.8\sigma$  to  $3.7\sigma$  (for  $c_s^2 \rightarrow 0$ ) when replacing ext-BAO by DESI-BAO. This improvement is accompanied by uncertainty reductions of  $\sim 45\%$  and  $\sim 15\%$  on the 2D posterior of  $(w_0, w_a)$  compared to *Planck* + PanPlus + DESI-BAO and *Planck* + PanPlus + ext-BAO + EFTBOSS, respectively. Interestingly, our joint *Planck* + PanPlus + DESI-BAO + EFTBOSS analysis yields a significantly stronger preference than the  $2.5\sigma$  significance reported in ref. [3] from *Planck* + PanPlus + DESI-BAO + DESI FS, where DESI FS relies solely on the full-shape power spectrum. These results highlight the crucial role of the bispectrum in probing evolving dark energy, further demonstrating that it carries substantial information beyond the sound horizon.

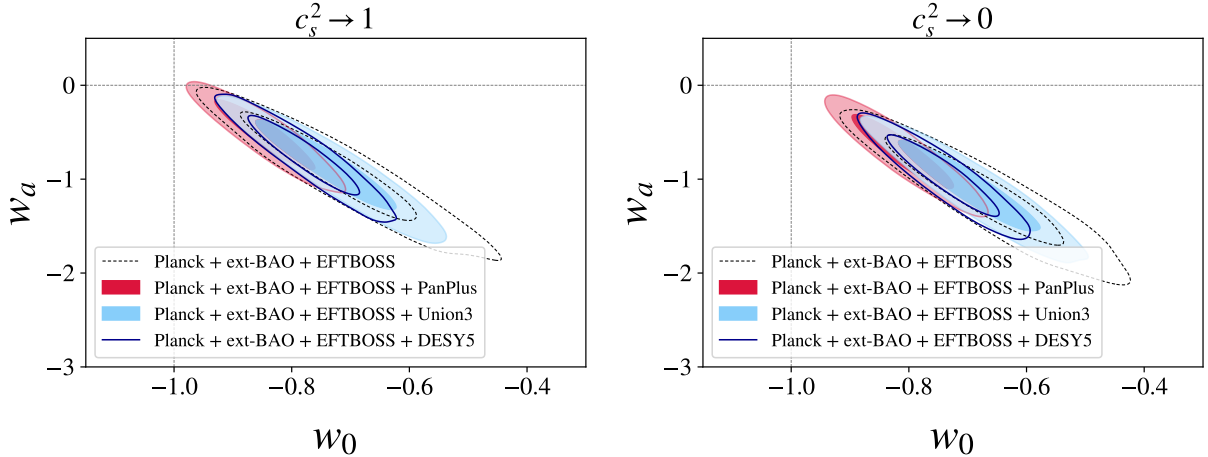


Figure 6: **Impact of supernova data on  $(w_0, w_a)$  constraints** — 2D posteriors of  $(w_0, w_a)$  from *Planck* + ext-BAO + EFTBOSS combined with various supernova data (*i.e.*, no supernovae data, PanPlus, Union3, or DESY5) within  $w_0w_a$ CDM for smooth (left) and clustering (right) quintessence. See also fig. 1.

**Impact of supernova data** We compare in fig. 6 the 2D posteriors in the  $w_0$  –  $w_a$  plane from *Planck* + ext-BAO + EFTBOSS without supernova data, or in combination with PanPlus, Union3, or DESY5. Corresponding 68% credible intervals of  $w_0$  and  $w_a$  with preference over  $\Lambda$  are shown in tab. 2. With no supernovae, the significance reduces to  $< 0.6\sigma$  for both smooth and

clustering quintessence.<sup>20</sup> As already mentioned above, supernovae are thus crucial in driving the preference for evolving dark energy, in line with DESI Y1 results [1, 3]. In addition, the significance over  $\Lambda$  increases from  $2.6\sigma$  to  $3.4\sigma$  ( $3.7\sigma$ ) when replacing PanPlus by Union3 (DESY5) in smooth quintessence, and from  $2.8\sigma$  to  $3.7\sigma$  ( $3.9\sigma$ ) in clustering quintessence, following the same trend as found with DESI Y1 data.<sup>21</sup>

Finally, in the right panel of fig. 1, we perform the same exercise replacing ext-BAO by DESI-BAO while properly marginalising over the sound horizon information in EFTBOSS. The corresponding 68% credible intervals of  $w_0$  and  $w_a$  with the preference over  $\Lambda$  are shown in tab. 2. For clustering quintessence, the preference over  $\Lambda$  increases from  $3.7\sigma$  to  $3.8\sigma$  ( $4.4\sigma$ ) when replacing PanPlus with Union3 (DESY5). Notably, in contrast to the DESI Y1 results [3], the preference obtained from the three supernova datasets remains relatively stable ( $\lesssim 1\sigma$ ) when they are combined with *Planck* + DESI-BAO + EFTBOSS/ $r_s^{\text{marg}}$ .

## 4.2 Consistency checks

To assess the robustness of our results, we systematically examine and compare different analysis configurations against our baseline setup. In particular, we remind that our baseline setup consists in

1. the power spectrum  $P$  and bispectrum  $B$  at one loop;
2. the bispectrum cutoff scales  $k_{\text{max}}^{\text{lowz}} = 0.20 h/\text{Mpc}$  and  $k_{\text{max}}^{\text{highz}} = 0.23 h/\text{Mpc}$ ;
3. the exact-time dependence of nonlinear EFTofLSS operators;
4. the EFT priors presented in sec. 3.3;
5. the monopole  $P_0$  and the quadrupole  $P_2$  of the power spectrum.

In the following, we vary each of these configurations, using the *Planck* + PanPlus + ext-BAO + EFTBOSS dataset.

**Power spectrum vs. bispectrum** To assess the impact of the bispectrum on the constraints, we show in the top panels of fig. 7 the difference in the posteriors of  $(w_0, w_a)$  upon its inclusion. Without the bispectrum, we obtain a  $1.4\sigma$  ( $1.5\sigma$ ) preference over  $\Lambda$  for  $c_s^2 \rightarrow 1$  ( $c_s^2 \rightarrow 0$ ). Including this contribution increases the significance to  $2.6\sigma$  ( $2.8\sigma$ ), corresponding to a relative shift of  $\sim 0.5\sigma$  in the 2D plane, mostly along the principal axis of the ellipse, and an uncertainty reduction of  $\sim 30\%$  on the 2D posterior (corresponding to  $\sim 15\%$  on the 1D marginals). To isolate the impact of the bispectrum, we compare in fig. 8 the constraints derived from the one-loop power spectrum alone, from the one-loop bispectrum alone, and from the combined one-loop power spectrum and tree-level bispectrum (restricting  $k_{\text{max}} = 0.08 h \text{ Mpc}^{-1}$  in the latter). We observe

<sup>20</sup>As checked on fake synthetic data, we find prior volume projection effects at  $> 1\sigma$  when not including any supernova data, in accordance with the observed shift between the posterior mean and maximum a posteriori.

<sup>21</sup>Ref. [3] finds an increase from  $2.5\sigma$  to  $3.4\sigma$  ( $3.8\sigma$ ) when replacing PanPlus by Union3 (DESY5) data.

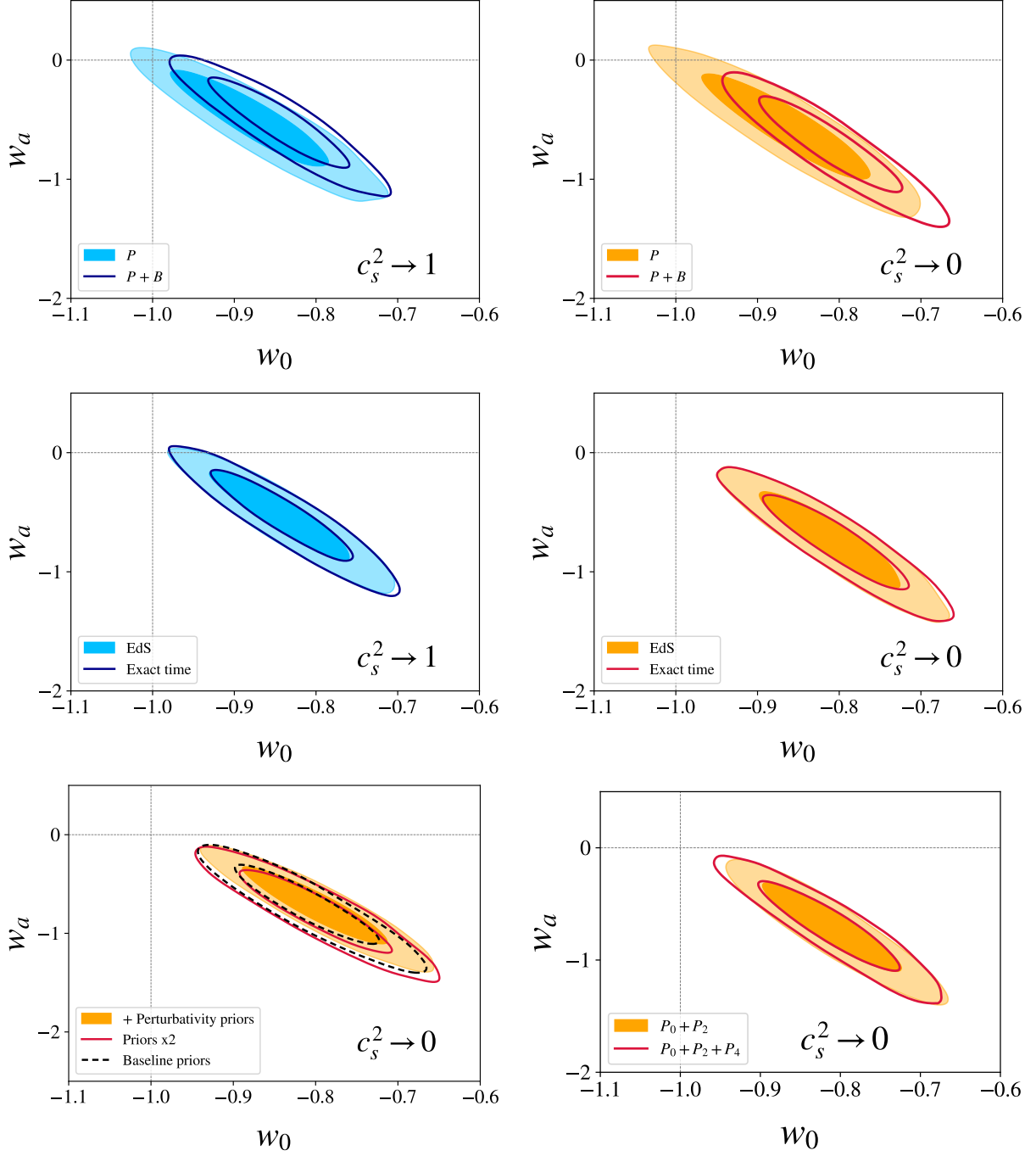


Figure 7: **Constraints on  $(w_0, w_a)$  across analysis variations** — This figure illustrates the impact of different analysis choices relative to our baseline setup: the addition of the bispectrum (*upper panels*), the EdS time approximation (*middle panels*), the prior choice on EFT parameters (*lower left panel*), and the addition of the power spectrum hexadecapole (*lower right panel*). Comparison are shown for both smooth ( $c_s^2 \rightarrow 1$ ) and clustering ( $c_s^2 \rightarrow 0$ ) quintessence, except in the lower panels, where only clustering quintessence is shown. See main text for more details.

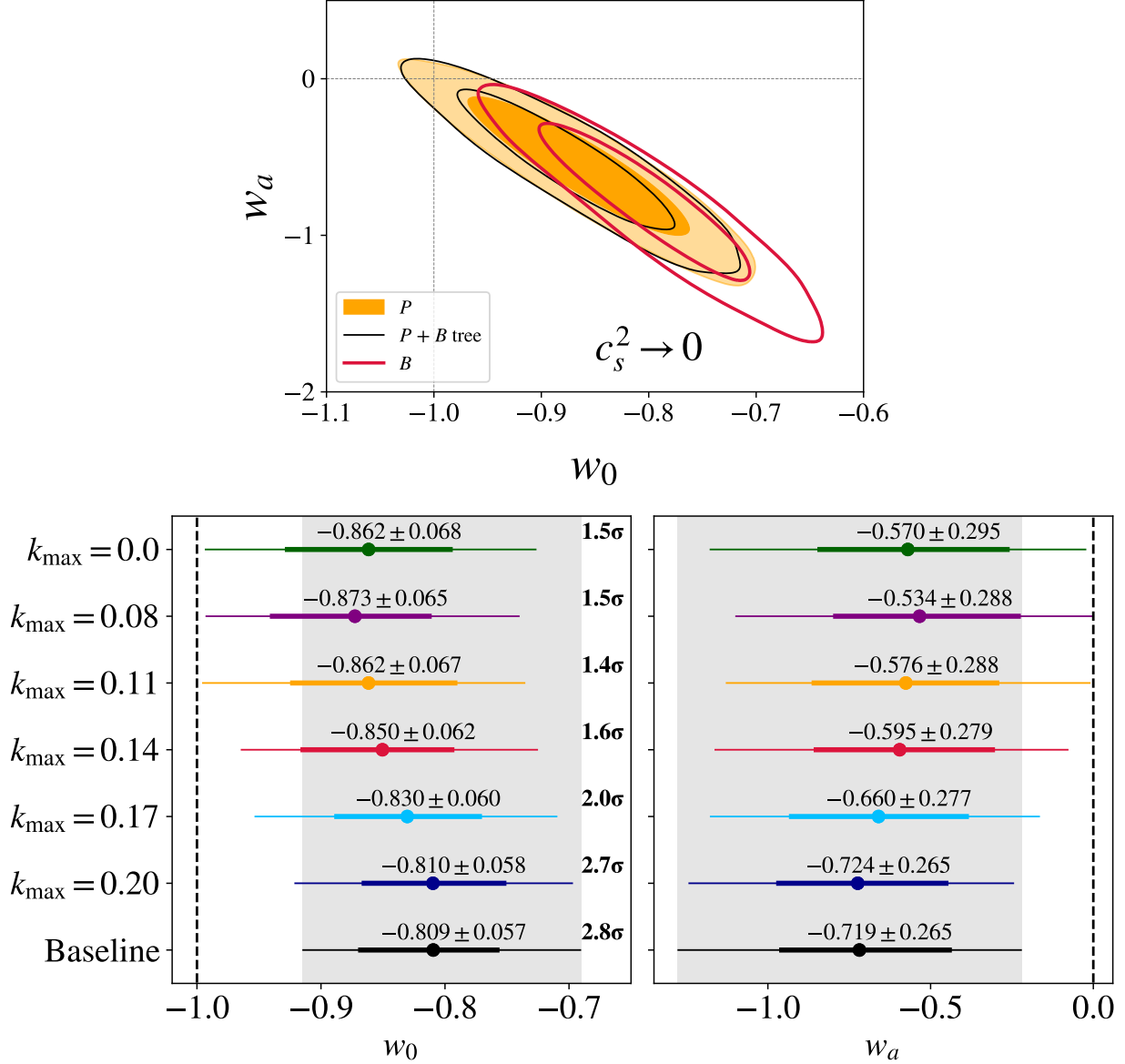


Figure 8: **Impact of the bispectrum on  $(w_0, w_a)$  constraints** — *Upper panel:* Comparison of the constraints in clustering quintessence derived from *Planck* + PanPlus + ext-BAO + EFTBOSS, where EFTBOSS includes the one-loop power spectrum alone, the one-loop bispectrum alone, or the combined one-loop power spectrum and tree-level bispectrum. Contrary to the one-loop bispectrum, the tree-level one is analysed only up to  $k_{\text{max}} = 0.08 \ h\text{Mpc}^{-1}$ . *Bottom panel:* 68% credible intervals and significance over  $\Lambda$  for clustering quintessence as a function of the highest  $k_{\text{max}}$  (in  $h\text{Mpc}^{-1}$ ) used in the analysis of the bispectrum. “Baseline” corresponds to the fiducial scale cuts used in our main analysis. See main text for details.

that the bispectrum drives the constraints away from  $\Lambda$ , provided that it is analysed up to the  $k$ -reach accessible by one-loop predictions. A similar, albeit weaker, trend is seen when assuming a constant equation of state as discussed in ref. [18].

**Cutoff scale** In fig. 8, we show the 68% credible intervals of  $w_0$  and  $w_a$ , together with the significance over  $\Lambda$ , as a function of the highest Fourier mode  $k_{\text{max}}$  included in the analysis of the bispectrum.<sup>22</sup> In particular, we display the analysis without the bispectrum (*i.e.*,  $k_{\text{max}} = 0 \text{ h Mpc}^{-1}$ ), the analysis with the tree-level bispectrum (*i.e.*,  $k_{\text{max}} = 0.08 \text{ h Mpc}^{-1}$ ), the baseline analysis (*i.e.*,  $k_{\text{max}}^{\text{lowz}} = 0.20 \text{ h Mpc}^{-1}$  and  $k_{\text{max}}^{\text{highz}} = 0.23 \text{ h Mpc}^{-1}$ ), as well as several intermediate cutoff scales, namely  $k_{\text{max}} \in [0.11, 0.14, 0.17, 0.29] \text{ h Mpc}^{-1}$ . Deviations from  $\Lambda$ , together with improvement in the constraints, start around  $k_{\text{max}} = 0.14 \text{ h Mpc}^{-1}$ , progressively increasing until the highest  $k_{\text{max}}$  reachable at one loop which is used in our main analyses. This is to be contrasted with the marginal gain in precision from the inclusion of the tree-level bispectrum, reaching at most  $k_{\text{max}} \sim 0.08 - 0.10 \text{ h Mpc}^{-1}$ .

**EFTofLSS time dependence** In the middle panels of fig. 7, we show the difference in the 2D posteriors of  $(w_0, w_a)$  treating the time dependence in the EFTofLSS exactly, or assuming the EdS approximation (see sec. 2.3). As anticipated in figs. 2 and 3, the EdS approximation is valid for the current data precision *in the region preferred by the data*. The exact-time dependence might reveal to be significant for upcoming surveys such as future DESI data releases or Euclid.

**EFT priors** In the bottom left panel of fig. 7, we illustrate the effect of broadening the prior width on the EFT parameters (as described in sec. 3.3) by a factor 2. As the constraints remain virtually unchanged, we conclude that our prior choice has a negligible impact on the results. Additionally, we impose a prior, dubbed “perturbativity prior” in the same plot, on the size of the one-loop contributions to the power spectrum and bispectrum based on a perturbative convergence criterion. Along with our fiducial prior choice, this ensures that our constraints are marginalised over EFT parameter values for which loop corrections remain within their expected range in the EFTofLSS [95, 96]. Again, the constraints remain practically unchanged, reinforcing the conclusion that the region favored by the data is consistently described within the EFTofLSS. Moreover, tab. 3 shows that the relative shifts between the maximum a posteriori estimates and the posterior means are  $\lesssim 0.3\sigma$  for all cosmological parameters, and  $\lesssim 0.2\sigma$  for  $w_0$  and  $w_a$ , indicating that prior volume projection effects are not important. This stems from the efficient breaking of parameter degeneracies enabled by the dataset combination we use, consistent with the findings of ref. [3].

**Power spectrum multipoles** In the bottom right panel of fig. 7, we show the impact of the addition of the power spectrum hexadecapole. Given its small signal-to-noise ratio in BOSS [91, 92],

---

<sup>22</sup>The  $k_{\text{max}}$  of the power spectrum is kept unchanged in this exercise.

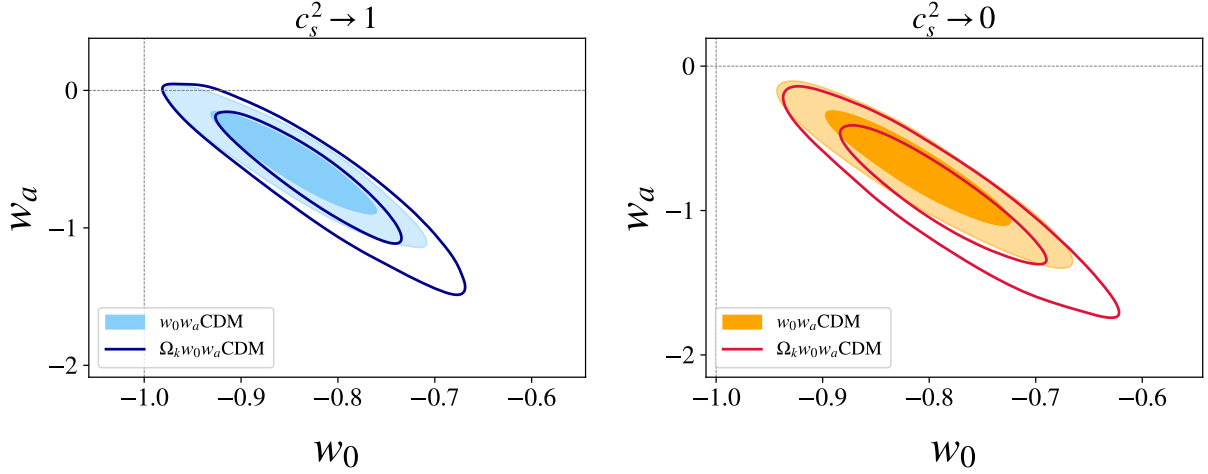


Figure 9: **Impact of free curvature on  $(w_0, w_a)$  constraints** — 2D posterior distributions of  $(w_0, w_a)$  from *Planck* + PanPlus + ext-BAO + EFTBOSS within  $w_0w_a$ CDM with or without free  $\Omega_k$  for both smooth (*left*) and clustering (*right*) quintessence.

this additional contribution has no additional constraining power, in particular in the  $w_0 - w_a$  plane.

In summary, we conclude that the preference for evolving dark energy is entirely driven by the bispectrum over the scales accessible to the EFTofLSS at one loop and appears robust in regards of the consistency checks we have conducted.

### 4.3 $w_0w_a$ CDM + $\Omega_k$

Is the preference for evolving dark energy sensitive to the curvature of the Universe? In fig. 9, we compare the 2D posterior distributions in the  $w_0 - w_a$  plane from the baseline dataset where  $\Omega_k$  is fixed to zero or let free (within a large flat prior), for both smooth and clustering quintessence. We respectively obtain  $\Omega_k = -0.0014 \pm 0.0027$  and  $\Omega_k = -0.0027 \pm 0.0025$  at 68%CL, both compatible with a flat Universe at  $\lesssim 1\sigma$ . As expected, the constraints on  $w_0$  and  $w_a$  are weakened because of the degeneracy with  $\Omega_k$ .<sup>23</sup> Yet, the preference over  $\Lambda$ , at  $2.7\sigma$  ( $2.9\sigma$ ) for  $c_s^2 \rightarrow 1$  ( $c_s^2 \rightarrow 0$ ), remains similar as in the flat case.

### 4.4 $w_0w_a$ CDM in modified gravity

In the analyses presented previously, we provided results for smooth quintessence assuming the standard fluid approximation. However, the  $c_s^2 \rightarrow 1$  limit allows stable dark energy fluctuations for  $w < -1$  only if the EFTofDE operators are adjusted to avoid gradient instabilities (2.29), thereby leading to the modified Poisson equation (2.19). The time dependence in the EFTofLSS is modified accordingly, as detailed in app. A.2. In fig. 10, we show the results obtained by fitting

<sup>23</sup>For smooth quintessence, we obtain  $w_0 = -0.825^{+0.060}_{-0.067}$  and  $w_a = -0.64^{+0.36}_{-0.28}$  at 68% CL, while for clustering quintessence, we obtain  $w_0 = -0.787 \pm 0.063$  and  $w_a = -0.91^{+0.34}_{-0.30}$  at 68% CL.

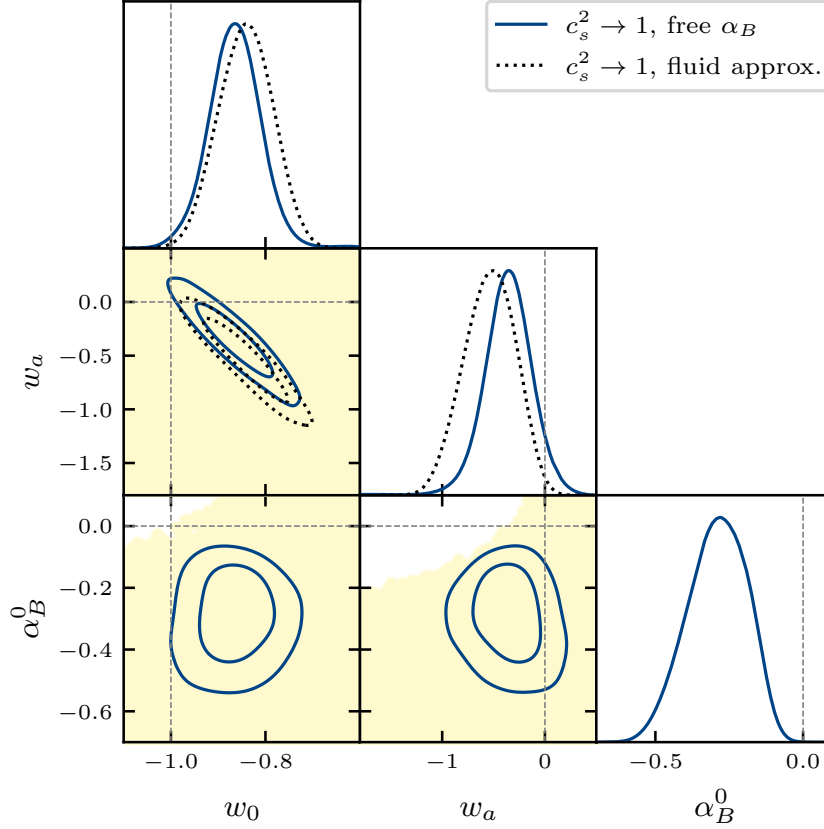


Figure 10:  $w_0 w_a$ CDM in modified gravity — 1D and 2D posteriors of  $(w_0, w_a, \alpha_B^0)$  from *Planck* + PanPlus + ext-BAO + EFTBOSS within  $w_0 w_a$ CDM for  $c_s^2 \rightarrow 1$ , with free braiding  $\alpha_B(t) = \alpha_B^0 \Omega_d(t)/\Omega_{d,0}$ . The beige area corresponds to the perturbatively stable region. Constraints from smooth quintessence in the standard fluid approximation are shown for reference.

*Planck* + PanPlus + ext-BAO + EFTBOSS within  $w_0 w_a$ CDM for  $c_s^2 \rightarrow 1$  with free  $\alpha_B$ , assumed to evolve as  $\alpha_B(t) = \alpha_B^0 \Omega_d(t)/\Omega_{d,0}$ .<sup>24</sup> To ensure that the stability conditions are satisfied in the fit,  $c_s^2$  is kept to unity by fixing  $\alpha_K = \nu - \alpha_w - 3\alpha_B^2$  (see eq. (2.12)), while  $\alpha_B$  is allowed to vary in the region that ensures  $\nu > 0$ .

Freeing  $\alpha_B$  results in a visible volume increase as well as a shift towards  $\Lambda$  in the posteriors of  $(w_0, w_a)$ , leading to  $w_0 = -0.868 \pm 0.056$ ,  $w_a = -0.33 \pm 0.24$ , and  $\alpha_B^0 = -0.283^{+0.12}_{-0.086}$  at 68%CL. Yet, the preference over  $\Lambda$  is raised to  $2.9\sigma$  (associated with  $\Delta\chi^2 = -13.3$ ), counting 3 additional degrees of freedom with respect to  $\Lambda$ CDM.  $w_0 w_a$ CDM in modified gravity is thus favoured over  $\Lambda$ CDM, given a departure in  $\alpha_B$  at the  $\sim 2.3\sigma$  level, as shown in fig. 10. Here we have only varied one EFTofDE parameter, the braiding  $\alpha_B$ , assuming that its time evolution is proportional to  $\Omega_d$ . A more comprehensive exploration of modified gravity in the EFTofDE would be insightful, extending over the analysis of ref. [97] based solely on the power spectrum and where a constant

<sup>24</sup>As we follow the conventions of ref. [33],  $\alpha_B$  defined in eq. (2.14) is related to  $\alpha'_B$  defined in `hi-class` as  $\alpha_B = -\alpha'_B/2$ . Notice also the normalisation  $\alpha_B \equiv 1$  at  $a = 1$  when  $\alpha_B^0 = 1$ .

$w$  is assumed.

## 5 Discussions

In this section, we first investigate how the preference we see for evolving dark energy arises across cosmic history (sec. 5.1). We then assess the significance for  $w < -1$  (sec. 5.2). Since this possibility is allowed by the data, we check that the stability conditions on the propagation of dark energy fluctuations laid in sec. 2 are met (sec. 5.3).

### 5.1 Dark energy histories

To understand the origin of the preference for  $(w_0, w_a)$  over  $\Lambda$ , we reconstruct the evolution of dark energy  $w(z)$  across cosmic history preferred by the data, delimiting the redshift range within which the data is sensitive to  $w$ . As a warm up, we identify the pivot epoch  $z_* \sim 0.25$  for which  $w(z)$  is best constrained. Next, we reconstruct  $w(z)$ , either assuming the CPL  $(w_0, w_a)$ -parametrisation or in a model-agnostic way. The reconstruction methodology is relegated to app. C. This comparison allows us to identify the deviations from  $\Lambda$  across redshifts driving the preference for  $(w_0, w_a)$ .

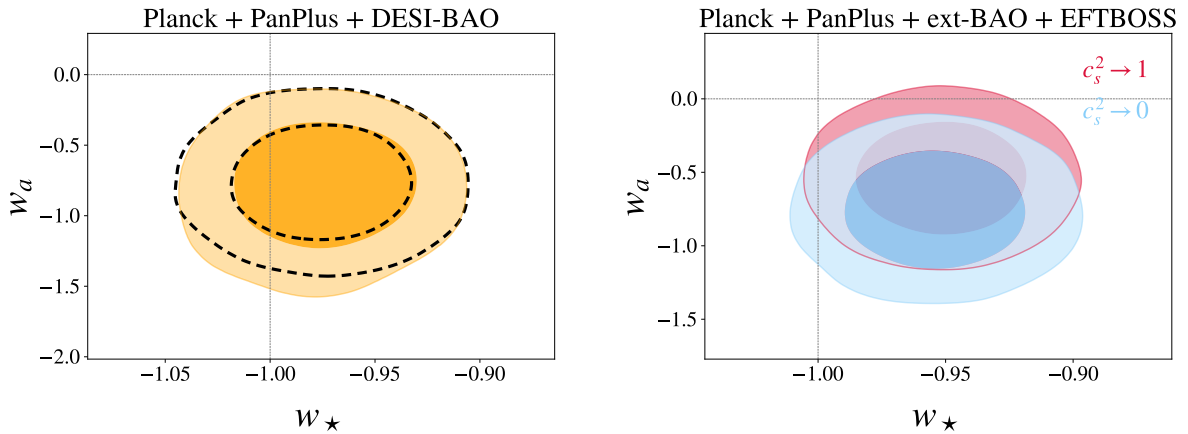


Figure 11:  **$w$  at the pivot  $z_*$**  — Posterior distributions in the  $w_* - w_a$  plane from *Planck* + PanPlus + DESI-BAO (left) or from *Planck* + PanPlus + ext-BAO + EFTBOSS (right) for smooth (red contour) or clustering (blue contour) quintessence. While we obtain those results by directly sampling  $w_*$  and  $w_a$  in the MCMC, the dashed contour is obtained under the Gaussian approximation (*i.e.*, minimising  $\sigma_{w_*}$  in eq. (5.4)), displaying good agreement.

**$w$  at the pivot** First, it is useful to look at the constraints on  $(w_*, w_a)$  [94], where  $w_*$  is defined at the pivot epoch  $a_*$ , such that

$$w_* = w_0 + (1 - a_*)w_a, \quad (5.1)$$

yielding  $w(a) = w_* + (a_* - a)w_a$ . The pivot epoch  $a_*$  is chosen such that  $w_*$  has minimal variance. As such,  $w_*$  can be seen as the principal component of the  $(w_0, w_a)$ -contours, *i.e.*, the major



semi-axis of the ellipse [98], implying that  $w_*$  and  $w_a$  are fully uncorrelated. While  $w_*$  is the best constrained value of  $w$  across cosmic history,  $w_a$  now becomes the local, linearised variation of  $w(a)$  around  $a_*$ . To find  $a_*$ , we use the fact that the Fisher matrices  $\mathcal{F}^*$  and  $\mathcal{F}^0$  of  $\mathbf{w}^* \equiv (w_*, w_a)$  and  $\mathbf{w}^0 = (w_0, w_a)$ , respectively, are related by

$$\mathcal{F}_{\mu\nu}^* = J_{\mu\alpha} \mathcal{F}_{\mu\nu}^0 J_{\beta\nu} , \quad (5.2)$$

through the Jacobian

$$J_{\mu\nu} = \partial w_\mu^* / \partial w_\nu^0 = \begin{pmatrix} 1 & 1 - a_* \\ 0 & 1 \end{pmatrix} . \quad (5.3)$$

Writing

$$(\mathcal{F}^*)_{\mu\nu}^{-1} = \begin{pmatrix} \sigma_{w_*}^2 & \sigma_{w_*} \sigma_{w_a} \rho \\ \sigma_{w_*} \sigma_{w_a} \rho & \sigma_{w_a}^2 \end{pmatrix} , \quad (5.4)$$

we can find the solution of  $a_*$  such that  $\rho \equiv 0$ . Equivalently, we can find  $a_*$  by minimising  $\sigma_{w_*}$  (and check that  $\rho \simeq 0$ ). Regardless the method we use, we get  $z_* \simeq 0.25 - 0.27$  for *Planck* + PanPlus + ext-BAO + EFTBOSS and *Planck* + PanPlus + DESI. We show the 2D posterior distributions in the  $(w_*, w_a)$  plane for both smooth and clustering quintessence in fig. 11. We summarise our findings as follows:

- The best constrained value  $w_*$  across cosmic history is above while being consistent with  $-1$  at  $\lesssim 1.7\sigma$  for all dataset combinations considered;
- The time derivative  $w_a$  is nonzero at  $1.5\sigma$  when analysing BOSS with  $c_s^2 \rightarrow 1$  and  $2.3\sigma$  when analysing either BOSS with  $c_s^2 \rightarrow 0$  or DESI BAO.

Therefore, while data mainly constrain  $w$  around  $z_* \sim 0.25$  at a value marginally consistent with  $-1$ , another culprit behind the deviation from  $\Lambda$ , that induces a non-negligible time variation (*i.e.*,  $w_a \neq 0$ ), is to be found elsewhere.

**$w(z)$  histories** In fig. 12, we show  $w(z)$  across cosmic history reconstructed from the posterior of  $(w_0, w_a)$  obtained in sec. 4. This is compared with the reconstruction of  $w(z)$  from a “model-independent” approach based on a general piecewise parametrisation  $\{w_i^z\}$ ,  $i = 1, \dots, N$ , with  $N = 9$ . For simplicity, we use here *Planck* + PanPlus + DESI-BAO. Given our findings in sec. 4.1, we do not expect our conclusions to change significantly if alternative dataset combinations are used. Our choice of redshift bins  $\{w_i^z\}$  roughly follows the division of galaxy clustering data from DESI, divided into 7 redshift bins between  $z \in [0.1, 4.16]$ , that we further complement with a bin at  $z \in [0, 0.1]$  and a bin at  $z \in [4.16, \infty]$ . Details on our reconstruction methodology are provided in app. C, where we also explain how the reconstructed  $w(z)$  which assumes the  $(w_0, w_a)$  parametrisation can be obtained by adjusting  $\{w_0, w_a\}$  to the posterior of  $\{w_i^z\}$ . From fig. 12, we make several observations:

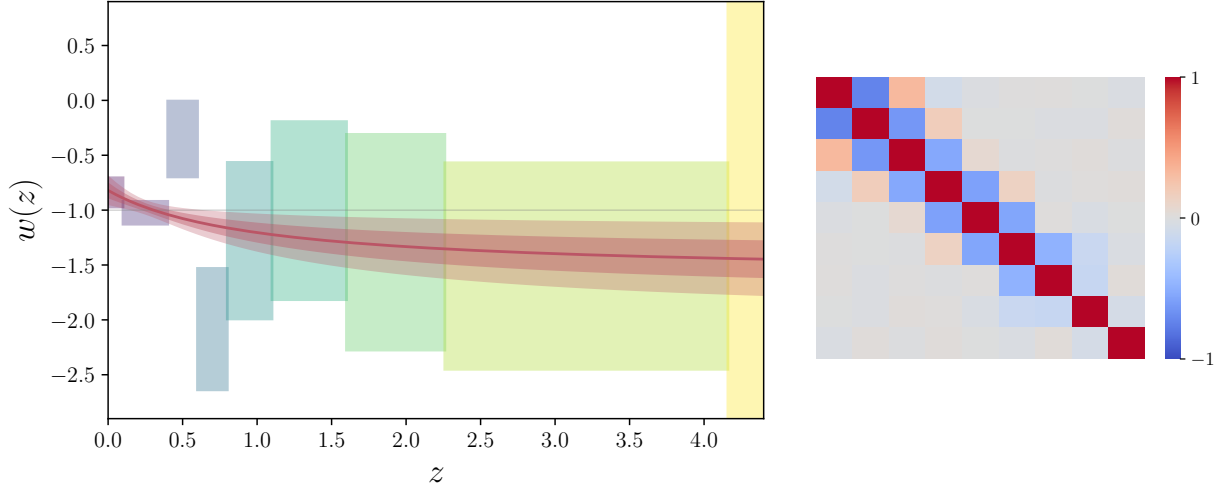


Figure 12: **Reconstructed dark energy equation of state  $w(z)$  across cosmic history** — *Left panel*: “Model-independent” piecewise parametrisation  $\{w_i^z\}$ ,  $i = 1, \dots, 9$ , where the coloured rectangles correspond to the 68% credible intervals of  $w(z)$  for the redshift ranges considered (with  $w_9^z$  partially depicted), compared to the reconstructed  $w(z)$  under the  $(w_0, w_a)$  parametrisation, where the 68% and 96% credible regions are shown in shaded red. *Right panel*: Correlation matrix of  $\{w_i^z\}$ .

- The constraint on  $w_*$  primarily originating from low redshifts around  $z_* \sim 0.25$  can be traced to the error bars on  $w_z^1$  and  $w_z^2$  being significantly smaller than those for the other  $w_i^z$ . The mild preference for  $w_* > -1$  seen in fig. 11 is driven by  $w_z^1$ , *i.e.*, low-redshift supernovae. For  $z \gg 1$ , the variance in  $w(z)$  increases as expected, given that  $\Omega_d/\Omega_m \ll 1$ .<sup>25</sup>
- The constraint on  $w_a$ , instead, is mainly driven by multiple  $w_i^z$  spanning from  $z \sim 0.6$  to  $z \sim 4$ , which consistently lie below  $-1$  to various degrees. Notably, at face value, the data around  $z \sim 0.7$  show a departure from  $\Lambda$  at almost  $2\sigma$ , though this should be interpreted with caution, as discussed in the next point.
- Since the transverse BAO parameter  $D_A$  and the luminosity distance  $D_L$  are integrated quantities along the line of sight, and supernovae and CMB lensing span multiple redshift bins, the estimated  $w_i^z$  exhibit an approximate  $\sim 50 - 70\%$  anticorrelation (see right panel of fig. 12) between neighbouring bins up to redshift  $z \sim 2.2$ , the maximal redshift covered by PanPlus supernovae. This implies that the apparent deviation in  $w(z)$  around redshift  $z \sim 0.7$  when inferred from the diagonal of the covariance is not solely driven by data at  $z \sim 0.7$  but also influenced by data from lower and higher redshifts.
- From the model-independent reconstruction, we find a  $1.7\sigma$  deviation from  $\Lambda$ , counting  $N = 9$  degrees of freedom. For the first 5 bins alone (for which deviations from  $\Lambda$  might appear

<sup>25</sup>To avoid unnecessary sampling in the high redshift bins where parameters such as  $w_9^z$  are practically unconstrained, we fit with restricted, yet wide, flat prior range  $-3 < w_i^z < 1$ .

significant), we find  $2.1\sigma$  instead. The data themselves thus provide only mild evidence for departure from  $\Lambda$ .

- The last bin,  $w_8^z$ , has no impact in the posterior of  $(w_0, w_a)$ , as deduced by reconstructing  $(w_0, w_a)$  using eq. (C.2) from the posterior of  $\{w_i^z\}$ , removing  $w_8^z$ . Further removing  $w_8^z$ , and subsequently  $w_7^z$ , leads to the  $(w_0, w_a)$ -posteriors shown in fig. 13, which we discuss in sec. 5.3.

In summary, the preference over  $\Lambda$  seen with  $(w_0, w_a)$  is not solely driven by the multiple deviations from  $\Lambda$  visible across cosmic history, but also by the inherent restriction of the  $(w_0, w_a)$ -parametrisation as discussed in app. C. See refs. [99–103] for alternative approaches to reconstructing dark energy evolution.

## 5.2 Quantifying the phantom evidence

For values of  $(w_0, w_a)$  satisfying  $w_a(a-1) > (w_0+1)$ , dark energy necessarily becomes phantom ( $w(a) < -1$ ) at some point in the past. Given that  $(w_0, w_a)$  is merely a parametrisation, enforcing this behaviour appears as a strong theoretical assumption. A committed Bayesian could argue that ultimately data serve as the referee: since the data favours  $(w_0, w_a)$ , this specific ‘model’ is naturally selected, even if it lies in the region where  $w < -1$ . However, to our knowledge, no known UV-complete construction allows for phantom dark energy.<sup>26</sup> Given a *zero measure* in the dark energy model space for  $w(z) < -1$ , this region would then be prohibited in a data analysis. When such prior is imposed, and given the inherent constraint of  $(w_0, w_a)$  mentioned above, the evidence for evolving dark energy over  $\Lambda$  is then immediately eliminated, as illustrated in the left panel of fig. 14 (see orange contour).

Yet, as seen in sec. 2.1, stable theories at low energies for  $w < -1$  can be build in EFT, irrespectively of known UV completion. We thus quantify the significance for  $w < -1$  throughout cosmic history from the constraints obtained in sec. 4. To do so, we assess how much more likely the data  $\mathcal{D}$  support, under a given parametrisation  $\phi$  for  $w(t)$  — *i.e.*,  $w(t) \equiv w(t|\phi)$  —, “ $w < -1$  somewhere” than “ $w \geq -1$  everywhere”, the latter being our null hypothesis (*i.e.*, no phantom behaviour). Denoting the events “ $w < -1$  somewhere” (for at least one time  $t$ ) and “ $w \geq -1$  everywhere” (for all times  $t$ ) as  $w^\exists < -1$  and  $w^\forall \geq -1$ , respectively, this is answered by computing the log-probability ratio

$$\lambda = -2 \ln \left[ \frac{\sup_{\{\phi|w^\exists < -1\}} \mathcal{P}(\phi|\mathcal{D})}{\sup_{\{\phi|w^\forall \geq -1\}} \mathcal{P}(\phi|\mathcal{D})} \right], \quad (5.5)$$

from which the significance level is determined as usual.<sup>27</sup> Eq. (5.5) represents the  $\chi_{\min}^2$ -difference found maximising  $\mathcal{P}(\phi|\mathcal{D})$  with or without imposing  $w \geq -1$  throughout cosmic history.<sup>28</sup> Under

<sup>26</sup>See however, *e.g.*, refs. [104–107].

<sup>27</sup>Here  $\sup_{\{\phi \in S\}} \mathcal{P}(\phi)$  denotes the supremum of  $\mathcal{P}(\phi)$  over all  $\phi \in S$ .

<sup>28</sup>In practice, we do not impose the condition  $w^\exists < -1$  to determine  $\sup_{\{\phi|w^\exists < -1\}} \mathcal{P}(\phi|\mathcal{D})$ , since the best fit already lies in a region where  $w^\exists < -1$ .

the  $(w_0, w_a)$  parametrisation, we find a preference for  $w < -1$  at  $2.3\sigma$  for *Planck* + PanPlus + DESI-BAO, while we obtain  $1.4\sigma$  ( $2.1\sigma$ ) for  $c_s^2 \rightarrow 0$  ( $c_s^2 \rightarrow 1$ ) when we replace DESI-BAO by ext-BAO + EFTBOSS, and  $2.7\sigma$  with DESI-BAO + EFTBOSS/ $r_s^{\text{marg}}$  for  $c_s^2 \rightarrow 1$ . There is thus a marginal hint for phantom behaviour, albeit weaker than the preference for  $(w_0, w_a)$  over  $\Lambda$ .

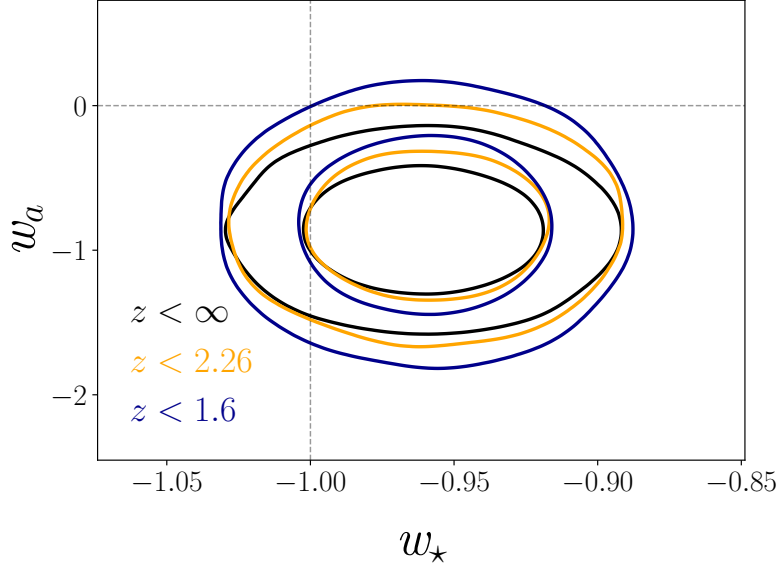


Figure 13: **Data redshift sensitivity window on  $(w_*, w_a)$**  — Comparison of  $(w_*, w_a)$  constraints when freeing the parametrisation of  $w(z)$  for  $z > z_t$ , where  $z_t = 1.6$  or  $z_t = 2.26$ , with floating parameters  $w_i^z$  for  $z_i > z_t$ . The constraint on  $w_*$ , coming from  $z_* = 0.25$ , remains practically untouched, while the one on  $w_a$  is progressively relaxed as we scan over decreasing  $z_t$ . In this plot, we use the *Planck* + PanPlus + DESI-BAO dataset and we reconstruct  $w_*$  and  $w_a$  according to the method developed in app. C.

### 5.3 Stability for $w < -1$

Building on our previous discussion about where  $w(z)$  is constrained across cosmic history, the key takeaway is that cosmological data primarily constrain  $w$  and its local variation within a limited redshift range. Consequently, any extrapolation of the linear parametrisation  $(w_0, w_a)$  in the far past should only be considered if there is a strong theoretical motivation to assume that  $w(z)$  continues to evolve in this specific parametric form. Since no such theoretical prior appears evident to us, we appeal for the possibility that  $w(z)$  may evolve differently beyond the redshift range where the data are sensitive (see refs. [108, 98, 109, 110] for related discussions). In principle, the sensitivity of the data to  $w$  decreases smoothly as  $\Omega_a(z)/\Omega_m(z) \rightarrow 0$ , corresponding to redshifts deep in the matter-dominated era. Therefore, to simplify the discussion, we introduce a transition redshift,  $z_t = 2.26$ , as a representative threshold. Below this redshift, we assume that  $w(z)$  follows the  $(w_0, w_a)$  parametrisation, while above  $z_t$ , we leave it unconstrained.<sup>29</sup> This choice

<sup>29</sup>Above  $z_t$ , we use floating parameters, *e.g.*,  $w_9^z$  introduced in sec. 5.1.

is well justified, as we find that allowing  $w(z)$  to vary freely above  $z_t$  only marginally relaxes the constraints on  $(w_0, w_a)$ , as shown in fig. 13.

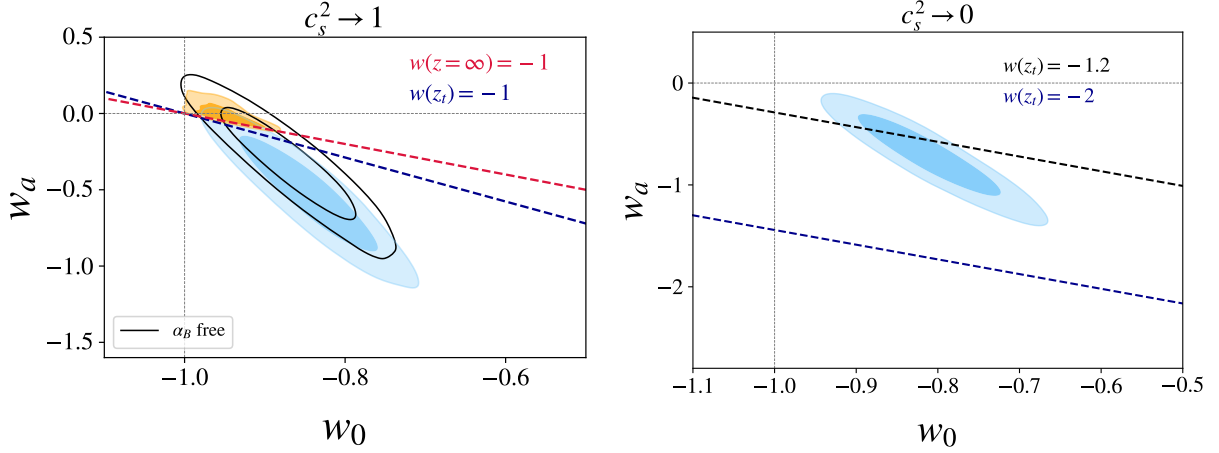


Figure 14: **Stability of dark energy fluctuations** — 2D posterior distributions in the  $w_0 - w_a$  plane with representative stability conditions (dashed lines) discussed in the main text for smooth (*left*) and clustering (*right*) quintessence (in cyan). Black and blue lines represent stability conditions on the redshift sensitivity range of the data, extending up to  $z_t \simeq 2.26$ , while the red line is on the whole cosmic history. The resulting posterior restricted to  $w > -1$  throughout cosmic history for  $c_s^2 \rightarrow 1$  (in orange) is shown for illustration. We also show in black contour the posterior obtained in the  $c_s^2 \rightarrow 1$  limit with the modified Poisson equation (2.19), where dark energy fluctuations remain stable in the  $w < -1$  limit.

We now assess the significance of our results in light of the stability conditions governing the propagation of dark energy fluctuations laid in sec. 2.1. As highlighted there,  $w < -1$  is allowed if possible operators in the EFT are present (irrespectively of potential UV completions). For each class of theories identified in sec. 2.2, we show in fig. 14 the priors on  $w(z)$  that ensure stability, especially within the redshift range where the data are sensitive to  $w$ , namely  $z \lesssim z_t$ . For *Planck* + PanPlus + ext-BAO + EFTBOSS, our findings are as follows:

- *k-essence models*, for which  $w < -1$  is prohibited, remains consistent with  $\Lambda$ , whether we impose  $w < -1$  as a strict prior throughout cosmic history (see the orange contour above the red dashed line in the left panel of fig. 14) or within the data redshift sensitivity window, *i.e.*, up to  $z = z_t$  (see the blue dashed line in the left panel of fig. 14). We note that refs. [111–113] have shown that the EFTofDE reduces to *k-essence* based on constraints imposed by the speed of graviton measured by LIGO/Virgo [114] and its potential decay into dark energy, assuming the EFTofDE to be valid up to the energy scales observed at LIGO (with caveats discussed in ref. [115]).
- The  $c_s^2 \rightarrow 1$  limit is stable for  $w < -1$  when additional EFTofDE parameters stabilising the gradient are present (see black contour in the left panel of fig. 14), as highlighted in sec. 2.1. The case with free  $\alpha_B$  was presented in sec. 4.4, for which a  $2.9\sigma$  preference over  $\Lambda$  was found.

- The  $c_s^2 \rightarrow 0$  limit permits stable dark energy fluctuations for  $w < -1$ , but only if  $w \gtrsim -1.2$  when stabilised via  $\alpha_B$  or if  $w \gtrsim -2$  when stabilised using higher-order operators [44]. As discussed in sec. 2.1, assuming the presence of such additional operators has no incident on the cosmological analysis. These stability conditions are displayed in the right panel of fig. 14. While the significance over  $\Lambda$  would also reduce, by roughly a half, in the sole presence of  $\alpha_B$ , it stays intact if the gradient instability is safely confined at large scales by higher-derivative corrections.

In summary, consistently enforcing stability conditions on the propagation of dark energy fluctuations can influence the results. Ultimately, a significant preference for evolving dark energy arises in the  $c_s^2 \rightarrow 0$  limit assuming the presence of higher-derivative operators or in the  $c_s^2 \rightarrow 1$  limit stabilised by  $\alpha_B$ .

## 6 Conclusions

In this paper, we have looked for deviations from  $\Lambda$  by probing the time evolution of the dark energy equation of state  $w(t)$  in the cosmological data, primarily using the  $(w_0, w_a)$  parametrisation. One key novelty is the inclusion of the one-loop bispectrum, which is found to be essential for constraining dark energy evolution. We summarise our main findings as follows:

- Considering the combination of *Planck*, Pantheon+ supernovae, ext-BAO measurements, with BOSS power spectrum and bispectrum, we find a preference for evolving dark energy (using the  $w_0 w_a$ CDM model) at  $2.6\sigma$  for  $c_s^2 \rightarrow 1$  (smooth quintessence), and at  $2.8\sigma$  for  $c_s^2 \rightarrow 0$  (clustering quintessence). This preference is due to the combination of PanPlus and EFTBOSS, which breaks degeneracies in the  $h - w_0/w_a$  and  $\Omega_m - w_0/w_a$  planes (see fig. 5). The preference increases at  $3.4\sigma$  ( $3.7\sigma$ ) when we replace Pantheon+ by Union3 (DESY5) for  $c_s^2 \rightarrow 1$ , while it increases at  $3.6\sigma$  ( $3.9\sigma$ ) for  $c_s^2 \rightarrow 0$ .
- The preference for evolving dark energy is observed consistently across two independent galaxy clustering datasets, namely SDSS/BOSS DR12 and DESI Y1, when they are combined with CMB and supernovae data. This suggests that it is unlikely that the detected signal is due to an instrumental systematic effect in either DESI or BOSS, as such a bias would have to affect both experiments in the same way. In addition, since the preference vanishes when supernova data are excluded from the analysis, further investigation is required to clarify the role played by supernovae in driving this result (see *e.g.*, refs. [116, 117] for discussions regarding DESY5 supernovae).
- The preference from pre-DESI data shows up upon inclusion of the BOSS bispectrum, which is analysed on an extended  $k$ -range thanks to the one-loop predictions from the EFTofLSS. Since our analysis follows a different methodology than that used in DESI Y1 BAO, and given the consistency checks outlined in sec. 4.2, our findings suggest that this evidence is not an artifact of systematic biases in the analysis methods. Moreover, our work motivates an analysis of DESI data including the bispectrum at one-loop.

- Combining DESI Y1 BAO with BOSS power spectrum and bispectrum, together with *Planck* and Pantheon+ supernovae, we find a  $3.7\sigma$  preference over  $\Lambda$  in the  $c_s^2 \rightarrow 0$  limit within  $w_0 w_a$ CDM. This preference increases at  $3.8\sigma$  ( $4.4\sigma$ ) when replacing Pantheon+ with Union3 (DESY5). These results are obtained marginalising over the sound horizon in BOSS full-shape analysis to avoid unaccounted correlation with DESI BAO measurements (see sec. 3.2). Since a significant fraction of objects observed by DESI Y1 were already observed by BOSS [71] — a fraction that will increase with future DESI data releases — further work is needed to properly account for the correlations between these datasets (at the covariance level) to fully exploit the constraining power of LSS. These results also underscore that the bispectrum carries substantial information beyond the BAO, further motivating sound horizon-free analyses.
- The preference over  $\Lambda$  depends on assumptions regarding the propagation of dark energy fluctuations and their stability conditions. The standard  $c_s^2 \rightarrow 1$  limit is either disfavoured compared to the  $c_s^2 \rightarrow 0$  limit if restricting to the  $k$ -essence regime (practically indistinguishable from  $\Lambda$ , as shown in fig. 14), or comparably favoured when additional degrees of freedom preventing gradient instabilities for  $w < -1$  are introduced (see sec. 4.4). In this work, we have considered stabilisation via a single EFTofDE operator, the braiding  $\alpha_B$ . A more systematic study, following the approach of ref. [97], would be valuable. In that context, a joint fit with galaxy lensing data — known to efficiently break degeneracies introduced by additional EFTofDE parameters (see *e.g.*, ref. [3]) — would be useful for strengthening the constraints in the  $c_s^2 \rightarrow 1$  limit. Additionally, it would be interesting to investigate dark energy with intermediate values of  $c_s^2$ , introducing scale dependence in the growth of fluctuations, or in beyond Horndeski theories [118].
- Our results suggest that exploring dark energy evolution would benefit from more general parametrisations of  $w(t)$  as touched in sec. 5.1 and app. C, to allow a consistent link between theoretical models and what the cosmological data can tell us on  $w(t)$ .<sup>30</sup> Intriguingly, as outlined in sec. 5.1, we find, assuming the  $(w_0, w_a)$  parametrisation, a significance for  $w < -1$  throughout cosmic history at  $1.4\text{--}2.7\sigma$  depending on the galaxy clustering dataset considered (combined with *Planck* and Pantheon+) in the  $c_s^2 \rightarrow 0$  limit.<sup>31</sup> If this hint persists, it would motivate the development of UV-complete descriptions that can accommodate phantom dark energy.

We hope to explore some of these promising directions in future work.

---

<sup>30</sup>Departure from  $\Lambda$  seen in  $(w_0, w_a)$  can still prove useful if dark energy models are systematically mapped onto the  $(w_0, w_a)$ -space, properly accounting for the data sensitivity in that mapping. If the preference aligns with regions where viable models exist, this could serve as a powerful discriminant (see *e.g.*, refs. [119, 109, 120]).

<sup>31</sup>For  $c_s^2 \rightarrow 1$ , the significance for  $w < -1$  is  $\lesssim 1\sigma$ .

## Acknowledgements

We thank Guido D’Amico, Matthew Lewandowski, Vivian Poulin, Leonardo Senatore, and Filippo Vernizzi for useful discussions or comments on the draft. We gratefully acknowledge Yi-Fu Cai for support. TS and PZ thank the Theory Group at CERN for hospitality during completion of this work. We acknowledge the use of computational resources from the computer clusters *Linda & Judy* at USTC, LUPM’s cloud computing infrastructure founded by Ocevu labex and France-Grilles, as well as the Euler cluster at ETH Zürich.

## A Details on the EFTofLSS

### A.1 Time dependence in presence of quintessence

The growth factor  $D$  is defined as the solution of

$$\frac{d^2 D}{d \ln a^2} + \left( 2 + \frac{d \ln H}{d \ln a} - \frac{d \ln C}{d \ln a} \right) \frac{dD}{d \ln a} - \frac{3}{2} \Omega_m C D = 0, \quad (\text{A.1})$$

which results from linearising the equations of motion of the smoothed fields, namely eqs. (2.31) and (2.32). Here the Hubble parameter is given by eq. (2.9). In the smooth ( $c_s^2 \rightarrow 1$ ) limit,  $C = 1$ , while it is given by eq. (2.26) in the clustering ( $c_s^2 \rightarrow 0$ ) limit. For a constant  $w$ , eq. (A.1) has analytical solutions given in terms of hypergeometric functions [121]. For a general  $w(a)$ , while there exists a closed form solution in the clustering limit [36], it is not the case in the  $c_s^2 \rightarrow 1$  limit. In this work, we thus numerically solve eq. (A.1), starting the initial time deep inside matter domination that selects initial conditions from an EdS Universe,

$$D_+(a) \propto a \quad \text{and} \quad D_-(a) \propto a^{-3/2}, \quad (\text{A.2})$$

where  $D_+$  and  $D_-$  are the growing and decaying solutions of eq. (A.1). We have checked that our numerical solutions agree to closed form solutions in the limits where the latter exist. Accordingly, we have two solutions for the growth rate  $f = \frac{d \ln D}{d \ln a}$ , yielding  $f_+$  and  $f_-$  from the definition of  $f$  using  $D_+$  or  $D_-$ .

Defining the Green’s functions from the equations of motion as

$$a \frac{dG_\sigma^\delta(a, \tilde{a})}{da} - f_+(a) G_\sigma^\theta(a, \tilde{a}) = \lambda_\sigma \delta_D(a - \tilde{a}), \quad (\text{A.3})$$

$$a \frac{dG_\sigma^\theta(a, \tilde{a})}{da} - f_+(a) G_\sigma^\theta(a, \tilde{a}) - \frac{f_-(a)}{f_+} \left( G_\sigma^\theta(a, \tilde{a}) - G_\sigma^\delta(a, \tilde{a}) \right) = (1 - \lambda_\sigma) \delta_D(a - \tilde{a}), \quad (\text{A.4})$$

where  $\sigma \in \{1, 2\}$ , while  $\lambda_1 = 1$  and  $\lambda_2 = 0$ . The solutions for the nonlinear time functions with



exact time dependence can be written as

$$G_1^\delta(a, \tilde{a}) = \frac{1}{\tilde{a}W(\tilde{a})} \left( \frac{dD_-(\tilde{a})}{d\tilde{a}} D_+(a) - \frac{dD_+(\tilde{a})}{d\tilde{a}} D_-(a) \right) \Theta(a - \tilde{a}) , \quad (\text{A.5})$$

$$G_2^\delta(a, \tilde{a}) = \frac{f_+(\tilde{a})/\tilde{a}^2}{W(\tilde{a})} \left( D_+(\tilde{a})D_-(a) - D_-(\tilde{a})D_+(a) \right) \Theta(a - \tilde{a}) , \quad (\text{A.6})$$

$$G_1^\theta(a, \tilde{a}) = \frac{a/\tilde{a}}{f_+(a)W(\tilde{a})} \left( \frac{dD_-(\tilde{a})}{d\tilde{a}} \frac{dD_+(a)}{da} - \frac{dD_+(\tilde{a})}{d\tilde{a}} \frac{dD_-(a)}{da} \right) \Theta(a - \tilde{a}) , \quad (\text{A.7})$$

$$G_2^\theta(a, \tilde{a}) = \frac{f_+(\tilde{a})a/\tilde{a}^2}{f_+(a)W(\tilde{a})} \left( D_+(\tilde{a}) \frac{dD_-(a)}{da} - D_-(\tilde{a}) \frac{dD_+(a)}{da} \right) \Theta(a - \tilde{a}) . \quad (\text{A.8})$$

Here  $W(\tilde{a})$  is the Wronskian of  $D_+$  and  $D_-$  and  $\Theta(a - \tilde{a})$  is the Heaviside step function. We impose the boundary conditions

$$G_\sigma^\delta(a, \tilde{a}) = 0 \quad \text{and} \quad G_\sigma^\theta(a, \tilde{a}) = 0 \quad \text{for} \quad \tilde{a} > a , \quad (\text{A.9})$$

$$G_\sigma^\delta(\tilde{a}, \tilde{a}) = \frac{\lambda_\sigma}{\tilde{a}} \quad \text{and} \quad G_\sigma^\theta(\tilde{a}, \tilde{a}) = \frac{(1 - \lambda_\sigma)}{\tilde{a}} . \quad (\text{A.10})$$

The generalised nonlinear time functions relevant to our predictions are given by

$$\mathcal{G}_\sigma^\lambda(a) = \int_0^1 G_\sigma^\lambda(a, \tilde{a}) \frac{f_+(\tilde{a})D_+^2(\tilde{a})}{C(\tilde{a})D_+^2(a)} d\tilde{a} , \quad (\text{A.11})$$

$$\mathcal{U}_\sigma^\lambda(a) = \int_0^1 G_1^\lambda(a, \tilde{a}) \frac{f_+(\tilde{a})D_+^3(\tilde{a})}{C(\tilde{a})D_+^3(a)} \mathcal{G}_\sigma^\delta(\tilde{a}) d\tilde{a}, \quad \mathcal{V}_{\sigma\tilde{\sigma}}^\lambda(a) = \int_0^1 G_\sigma^\lambda(a, \tilde{a}) \frac{f_+(\tilde{a})D_+^3(\tilde{a})}{C(\tilde{a})D_+^3(a)} \mathcal{G}_{\tilde{\sigma}}^\theta(\tilde{a}) d\tilde{a},$$

where  $\lambda \in \{\delta, \theta\}$  and  $\sigma, \tilde{\sigma} \in \{1, 2\}$ .

The additional function entering the galaxy field expansions, eqs. (A.25) and (A.26), is given by

$$\tilde{Y}(a) = -\frac{3}{14} \mathcal{G}(a)^2 + \mathcal{V}_{11}^\delta(a) + \mathcal{V}_{12}^\delta(a) , \quad (\text{A.12})$$

where  $\mathcal{G} = \mathcal{G}_1^\delta + \mathcal{G}_2^\delta$ .

## A.2 Time dependence in modify gravity

In this subsection, we provide the growth function and time dependence in the EFTofLSS for general dark energy and modified gravity models described by the EFTofDE in the quasi-static limit (assuming  $c_s^2 \rightarrow 1$ ), following refs. [81]. As discussed in sec. 2.1, we need to solve the equations of motion for a modified Poisson equation, that up to third order in fluctuations, reads [35]:

$$\begin{aligned} \frac{\partial^2 \Phi}{\mathcal{H}^2} = & \frac{3\Omega_m}{2} \mu_\Phi(t) \delta + \left( \frac{3\Omega_m}{2} \right)^2 \mu_{\Phi,2}(t) \left[ \delta^2 - \left( \frac{\partial_i \partial_j \delta}{\partial^2} \right)^2 \right] \\ & + \left( \frac{3\Omega_m}{2} \right)^3 \mu_{\Phi,22}(t) \left[ \delta - \frac{\partial_i \partial_j \delta}{\partial^2} \frac{\partial_i \partial_j}{\partial^2} \right] \left[ \delta^2 - \left( \frac{\partial_k \partial_l \delta}{\partial^2} \right)^2 \right] \\ & + \left( \frac{3\Omega_m}{2} \right)^3 \mu_{\Phi,3}(t) \left[ \delta^3 - 3\delta \left( \frac{\partial_i \partial_j \delta}{\partial^2} \right)^2 + 2 \frac{\partial_i \partial_j \delta}{\partial^2} \frac{\partial_k \partial_l \delta}{\partial^2} \frac{\partial_i \partial_k \delta}{\partial^2} \right] + O(\delta^4) . \end{aligned} \quad (\text{A.13})$$

The time-dependent functions  $\mu_\Phi$  in terms of EFTofDE parameters are given in ref. [35]. When only considering the braiding parameter  $\alpha_B$ , the equation reduces to eq. (2.19) at linear order.

The linear growth function  $D$  satisfies a modified second order differential equation,

$$\frac{d^2 D(a)}{d \ln a^2} + \left(2 + \frac{d \ln H}{d \ln a}\right) \frac{d D(a)}{d \ln a} - \frac{3}{2} \mu_\Phi(a) \Omega_m(a) D(a) = 0. \quad (\text{A.14})$$

The initial conditions are set according to the strategy of ref. [81] for numerical stability. The growing mode initial condition is still set deep in matter domination as in eq. (A.2), while the decaying mode is solved future to past using the boundary condition in the far future, yielding

$$D_+(a | a \ll a_0) \propto a, \quad D_-(a | a \gg a_0) \propto \left(\frac{a_0}{a}\right)^2. \quad (\text{A.15})$$

The derivation for the nonlinear time functions then follows closely the one in sec. A.1 but with additional source terms from the modified Poisson equation (A.13), yielding

$$\mathcal{G}_1^\lambda(a) = \int_0^1 \left[ G_1^\lambda(a, \tilde{a}) f_+(\tilde{a}) + G_2^\lambda(a, \tilde{a}) \mu_{\Phi,2}(\tilde{a}) M_1(\tilde{a}) \right] \frac{D_+^2(\tilde{a})}{D_+^2(a)} d\tilde{a}, \quad (\text{A.16})$$

$$\mathcal{G}_2^\lambda(a) = \int_0^1 G_2^\lambda(a, \tilde{a}) [f_+(\tilde{a}) - \mu_{\phi,2}(\tilde{a}) M_1(\tilde{a})] \frac{D_+^2(\tilde{a})}{D_+^2(a)} d\tilde{a},$$

$$\mathcal{U}_1^\lambda(a) = \int_0^1 \left\{ G_1^\lambda(a, \tilde{a}) f_+(\tilde{a}) \mathcal{G}_1^\delta(\tilde{a}) + G_2^\lambda(a, \tilde{a}) M_1(\tilde{a}) \left[ \mu_{\Phi,2}(\tilde{a}) \mathcal{G}_1^\delta(\tilde{a}) + M_2(\tilde{a}) \right] \right\} \frac{D_+^3(\tilde{a})}{D_+^3(a)} d\tilde{a}, \quad (\text{A.17})$$

$$\mathcal{U}_2^\lambda(a) = \int_0^1 \left\{ G_1^\lambda(a, \tilde{a}) f_+(\tilde{a}) \mathcal{G}_2^\delta(\tilde{a}) + G_2^\lambda(a, \tilde{a}) M_1(\tilde{a}) \left[ \mu_{\Phi,2}(\tilde{a}) \mathcal{G}_2^\delta(\tilde{a}) - M_2(\tilde{a}) \right] \right\} \frac{D_+^3(\tilde{a})}{D_+^3(a)} d\tilde{a}, \quad (\text{A.18})$$

$$\mathcal{V}_{11}^\lambda(a) = \int_0^1 \left\{ G_1^\lambda(a, \tilde{a}) f_+(\tilde{a}) \mathcal{G}_1^\theta(\tilde{a}) + G_2^\lambda(a, \tilde{a}) M_1(\tilde{a}) \left[ \mu_{\Phi,2}(\tilde{a}) \mathcal{G}_1^\delta(\tilde{a}) + M_2(\tilde{a}) \right] \right\} \frac{D_+^3(\tilde{a})}{D_+^3(a)} d\tilde{a}, \quad (\text{A.19})$$

$$\mathcal{V}_{21}^\lambda(a) = \int_0^1 \left\{ G_1^\lambda(a, \tilde{a}) f_+(\tilde{a}) \mathcal{G}_2^\theta(\tilde{a}) + G_2^\lambda(a, \tilde{a}) M_1(\tilde{a}) \left[ \mu_{\Phi,2}(\tilde{a}) \mathcal{G}_2^\delta(\tilde{a}) - M_2(\tilde{a}) \right] \right\} \frac{D_+^3(\tilde{a})}{D_+^3(a)} d\tilde{a}, \quad (\text{A.20})$$

$$\mathcal{V}_{12}^\lambda(a) = \int_0^1 G_2^\lambda(a, \tilde{a}) \left\{ f_+(\tilde{a}) \mathcal{G}_1^\theta(\tilde{a}) - M_1(\tilde{a}) \left[ \mu_{\Phi,2}(\tilde{a}) \mathcal{G}_1^\delta(\tilde{a}) + M_2(\tilde{a}) \right] \right\} \frac{D_+^3(\tilde{a})}{D_+^3(a)} d\tilde{a}, \quad (\text{A.21})$$

$$\mathcal{V}_{22}^\lambda(a) = \int_0^1 G_2^\lambda(a, \tilde{a}) \left\{ f_+(\tilde{a}) \mathcal{G}_2^\theta(\tilde{a}) - M_1(\tilde{a}) \left[ \mu_{\Phi,2}(\tilde{a}) \mathcal{G}_2^\delta(\tilde{a}) - M_2(\tilde{a}) \right] \right\} \frac{D_+^3(\tilde{a})}{D_+^3(a)} d\tilde{a}, \quad (\text{A.22})$$

$$(\text{A.23})$$

where

$$M_1(a) \equiv \frac{1}{f_+(a)} \left( \frac{3\Omega_m(a)}{2} \right)^2, \quad M_2(a) \equiv \frac{\mu_{\Phi,22}}{2} \frac{3\Omega_m(a)}{2}. \quad (\text{A.24})$$

### A.3 Bias expansion

In real space, the expansion of the galaxy density and velocity divergence up to third order in the presence of dark energy are given by

$$\begin{aligned}
\delta_g(\vec{k}, t) = & \tilde{c}_{\delta,1}(t) \left( \mathbb{C}_{\delta,1}^{(1)}(\vec{k}, t) + \mathcal{G}(t) \mathbb{C}_{\delta,1}^{(2)}(\vec{k}, t) + \mathcal{G}(t)^2 \mathbb{C}_{\delta,1}^{(3)}(\vec{k}, t) + \tilde{Y}(a) \mathbb{C}_Y^{(3)}(\vec{k}, a) \right) \quad (\text{A.25}) \\
& + \tilde{c}_{\delta,2}(t) \left( \mathbb{C}_{\delta,2}^{(2)}(\vec{k}, t) + \mathcal{G}(t) \mathbb{C}_{\delta,2}^{(3)}(\vec{k}, t) \right) \\
& + \tilde{c}_{\delta^2,1}(t) \left( \mathbb{C}_{\delta^2,1}^{(2)}(\vec{k}, t) + \mathcal{G}(t) \mathbb{C}_{\delta^2,1}^{(3)}(\vec{k}, t) \right) \\
& + \tilde{c}_{\delta,3}(t) \mathbb{C}_{\delta,3}^{(3)}(\vec{k}, t) + \tilde{c}_{\delta^2,2}(t) \mathbb{C}_{\delta^2,2}^{(3)}(\vec{k}, t) \\
& + \tilde{c}_{s^2,2}(t) \mathbb{C}_{s^2,2}^{(3)}(\vec{k}, t) + \tilde{c}_{\delta^3}(t) \mathbb{C}_{\delta^3}^{(3)}(\vec{k}, t) ,
\end{aligned}$$

$$\begin{aligned}
\theta_g(\vec{k}, t) = & \left( \mathbb{C}_{\delta,1}^{(1)}(\vec{k}, t) + \mathcal{G}(t) \mathbb{C}_{\delta,1}^{(2)}(\vec{k}, t) + \mathcal{G}(t)^2 \mathbb{C}_{\delta,1}^{(3)}(\vec{k}, t) + \tilde{Y}(a) \mathbb{C}_Y^{(3)}(\vec{k}, a) \right) \quad (\text{A.26}) \\
& + \left( \frac{7}{2} - \frac{7}{2} \mathcal{G}_1^\theta \right) \left( \mathbb{C}_{\delta,2}^{(2)}(\vec{k}, t) + \mathcal{G}(t) \mathbb{C}_{\delta,2}^{(3)}(\vec{k}, t) \right) \\
& + \left( -\frac{5}{2} + \frac{7}{2} \mathcal{G}_1^\theta \right) \left( \mathbb{C}_{\delta^2,1}^{(2)}(\vec{k}, t) + \mathcal{G}(t) \mathbb{C}_{\delta^2,1}^{(3)}(\vec{k}, t) \right) \\
& + \left( \frac{45}{7} - 9\mathcal{V}_{12}^\theta - \frac{45}{2} \mathcal{V}_{21}^\theta \right) \mathbb{C}_{\delta,3}^{(3)}(\vec{k}, t) + \left( -\frac{22}{7} - \frac{7}{4} \mathcal{G}_1^\theta + \frac{25}{6} \mathcal{V}_{12}^\theta + \frac{151}{8} \mathcal{V}_{21}^\theta \right) \mathbb{C}_{\delta^2,2}^{(3)}(\vec{k}, t) \\
& + \left( -\frac{3}{7} + 2\mathcal{V}_{12}^\theta + \frac{3}{2} \mathcal{V}_{21}^\theta \right) \mathbb{C}_{s^2,2}^{(3)}(\vec{k}, t) + \left( \frac{10}{7} + \frac{7}{2} \mathcal{G}_1^\theta - 2\mathcal{V}_{12}^\theta - \frac{69}{4} \mathcal{V}_{21}^\theta \right) \mathbb{C}_{\delta^3}^{(3)}(\vec{k}, t) ,
\end{aligned}$$

where the expressions for the operators  $\mathbb{C}$  can be found in ref. [52], and  $\mathbb{C}_Y^{(3)}$  in ref. [50]. The full list of forth order operators in the same basis of descendants (within EdS time approximation) can be found in ref. [15] (see also refs. [122, 123] for other, equivalent bases). For reasons mentioned in the main text, we use the exact-time dependence in the loop power spectrum, while for the bispectrum we only keep exact-time dependence at the tree level. The explicit redshift-space kernels up to fourth order can be found the inancillary `Mathematica` file distributed with ref. [15].

## B Supplementary analysis products

This appendix contains supplementary analysis products. In fig. 15, we display the 1D and 2D posterior distributions of the whole cosmological parameter space from *Planck* + PanPlus + ext-BAO + EFTBOSS for both smooth and clustering quintessence, while in tab. 3 we show the corresponding maximum a posteriori estimates as well as the 68% credible intervals. In fig. 16, we show the 1D and 2D posterior distributions of  $(w_0, w_a, \alpha_{r_s})$  obtained by fitting *Planck* + PanPlus + DESI-BAO + EFTBOSS/ $r_s^{\text{marg}}$  in the  $c_s^2 \rightarrow 0$  limit.

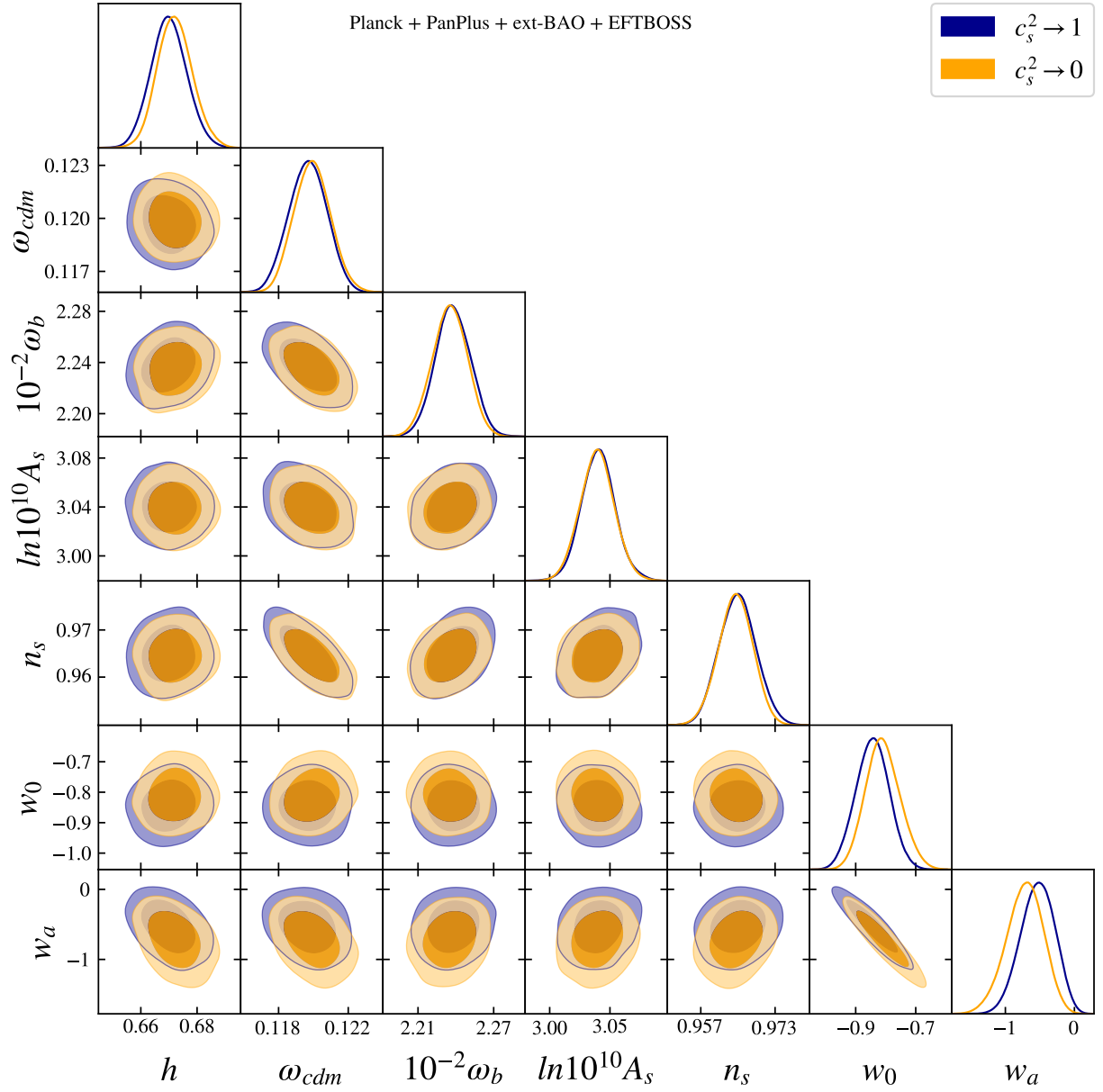


Figure 15: 1D and 2D posterior distributions of the cosmological parameters inferred from *Planck* + PanPlus + ext-BAO + EFTBOSS within  $w_0w_a$ CDM for both smooth and clustering quintessence.

## C Reconstructing $w(z)$ histories

In this appendix, we first lay down the methodology to reconstruct the credible region of  $w(z)$  from a given posterior distribution of its underlying parameters. For the exercise, we do so by comparing two parametrisations:  $(w_0, w_a)$ , serving as a representative candidate model of dark energy, and an (arbitrarily) general one, providing a model-agnostic way to probe the evolution of dark energy. We explain the difference in the reconstructed  $w(z)$ , highlighting that when no

Quintessence	$c_s^2 \rightarrow 1$	$c_s^2 \rightarrow 0$
$10^{-2}\omega_b$	2.237 $2.238 \pm 0.014$	2.237 $2.235 \pm 0.014$
$\omega_{\text{cdm}}$	0.1199 $0.1197 \pm 0.0011$	0.1199 $0.1199 \pm 0.0010$
$h$	0.6713 $0.6700 \pm 0.0063$	0.6714 $0.6722^{+0.0058}_{-0.0065}$
$\ln(10^{10} A_s)$	3.044 $3.040 \pm 0.014$	3.044 $3.039 \pm 0.014$
$n_s$	0.9658 $0.9650 \pm 0.0039$	0.9656 $0.9645 \pm 0.0037$
$\tau_{\text{reio}}$	0.0544 $0.0531 \pm 0.0073$	0.0544 $0.0520 \pm 0.0072$
$w_0$	-0.831 $-0.844 \pm 0.055$	-0.820 $-0.809^{+0.053}_{-0.061}$
$w_a$	-0.61 $-0.53^{+0.26}_{-0.23}$	-0.66 $-0.72^{+0.28}_{-0.25}$
$\Omega_m$	0.317 $0.3180 \pm 0.0067$	0.317 $0.3164 \pm 0.0064$
$\sigma_8$	0.8115 $0.8059 \pm 0.0093$	0.8119 $0.8104 \pm 0.0096$
$\chi^2_{\text{min}}$	4835.36	4834.22
$\Delta\chi^2_{\text{min}}$	-9.2	-10.3
p-value	$2.6\sigma$	$2.8\sigma$

Table 3: Maximum a posteriori estimates and 68% credible intervals of the cosmological parameters inferred from *Planck* + PanPlus + ext-BAO + EFTBOSS within  $w_0w_a$ CDM for both smooth quintessence and clustering quintessence, where EFTBOSS includes both the power spectrum and bispectrum.

model is assumed, we obtain an estimate of the data sensitivity on  $w(z)$  across cosmic history. In passing, we derive approximate analytical formulae for assessing the preference over  $\Lambda$  or for phantom behaviour. .

Let  $\phi$  and  $\psi$  be two sets of parameters of *non-equivalent* models for the observational data  $\mathcal{D}$ . Let  $\theta$  be the  $\Lambda$ CDM parameters that they share, such that the remaining ones offer two parametrisations of  $w(z)$ . We consider  $\phi \setminus \theta = (w_0, w_a)^T$  and  $\psi \setminus \theta = (w_1^z, w_2^z, \dots, w_N^z)^T$ , where  $w_i^z$  is the value of  $w$  in the redshift bin  $z_i$  and  $N$  is the number of bins. To avoid clutter, in the following we will simply denote  $\phi$  for  $\phi \setminus \theta$  and similarly for  $\psi$ , implicitly implying that  $\theta$  are marginalised when relevant. With  $N$  sufficiently large, we assume that  $\psi$  forms a partition of  $\mathcal{D}$ . Since  $\phi$  is just a parametric form for  $w(z)$  guiding our search, we do not know a priori if  $\phi$  forms a partition of  $\mathcal{D}$ . We thus do not assume so. Defining the map  $M : \Omega_\phi \subset \mathbb{R}^{N_\phi} \rightarrow \mathcal{T} \subset \mathbb{R}^N$  as  $\phi_\alpha \mapsto M_{i\alpha}\phi_\alpha$ , where  $\Omega_\phi \sim \mathcal{P}(\phi)$ , and where  $\mathcal{T}$  is the target space of the map  $M$ , which is a

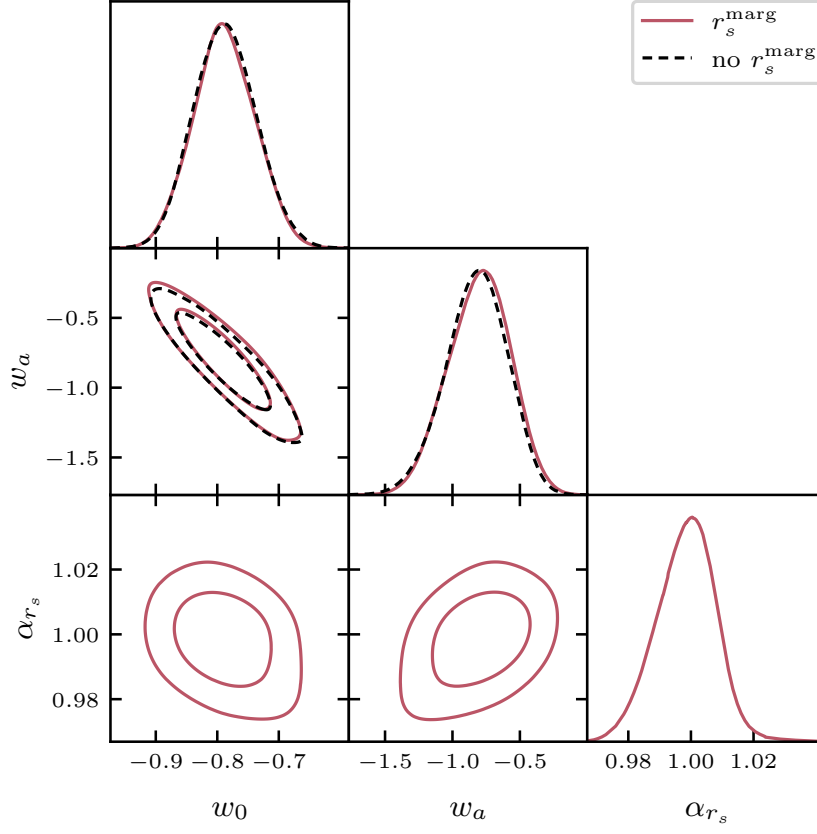


Figure 16: 1D and 2D posterior distributions of  $(w_0, w_a, \alpha_{r_s})$  inferred from *Planck* + PanPlus + DESI-BAO + EFTBOSS/ $r_s^{\text{marg}}$  within  $w_0 w_a$ CDM for clustering quintessence. Results combining DESI-BAO + EFTBOSS without marginalising over the sound horizon  $r_s$  are shown for reference.

subspace of  $\Omega_\psi \sim \mathcal{P}(\psi)$ , the domain of  $\psi$ .<sup>32</sup>

Reconstructing  $w(z)$  amounts to estimate  $\mathcal{P}(\psi|\mathcal{D})$ , that can be sampled from the likelihood  $\mathcal{L}(\mathcal{D}|\psi)$ , defined in sec. 3 with  $w(z)$  parametrised following  $\psi$ . The reconstructed  $w(z)$  is shown in fig. 12.

If  $\phi$  is not a partition of  $\mathcal{D}$ , we can not infer  $\mathcal{P}(\psi|\mathcal{D})$  from  $\mathcal{P}(\phi|\mathcal{D})$ . In contrast, if we believe that the data  $\mathcal{D}$  is well-specified by the model  $M$  parametrised by  $\phi$ , we may write

$$\mathcal{P}_{\mathcal{T}}(\psi|\mathcal{D}) = \int d^{N_\phi} \phi \mathcal{P}(\psi|\phi) \mathcal{P}(\phi|\mathcal{D}), \quad (\text{C.1})$$

where  $\mathcal{P}_{\mathcal{T}}$  means that the distribution lives in the target space  $\mathcal{T}$  of  $M$ . Since  $\mathcal{P}(\psi|\phi) = \prod_{i=1}^N \delta_D(\psi_i - M_{i\alpha} \phi_\alpha)$ , eq. (C.1) is equivalent to sampling  $\mathcal{P}_{\mathcal{T}}(\psi|\mathcal{D})$  by repeatedly drawing  $\phi$  according to  $\mathcal{P}(\phi|\mathcal{D})$  and applying the map  $M$ . This reconstruction appears clearly distinct from  $\mathcal{P}(\psi|\mathcal{D})$  in fig. 12. Since the two models specified by  $\phi$  and  $\psi$  are non-equivalent, we have that  $\mathcal{P}_{\mathcal{T}}(\psi|\mathcal{D}) \neq \mathcal{P}(\psi|\mathcal{D})$ .

<sup>32</sup>In general,  $M$  does not need to be a linear map, but for the case we consider,  $M$  consists in applying  $w(a) = w_0 + (1-a)w_a$ , i.e.,  $M_{i\alpha} = (1, 1-a_i)^T$  (with eventually a binning matrix).

To develop a more intuitive understanding of the situation, we can approach the problem from the opposite perspective. Since  $\psi$  is a partition of  $\mathcal{D}$ , for a given  $\mathcal{D}$  there exists a  $\psi$  that generates it. This implies that  $\mathcal{P}(\phi|\psi, \mathcal{D}) \equiv \mathcal{P}(\phi|\psi)$ , and using the law of total probability, we can write

$$\mathcal{P}(\phi|\mathcal{D}) = \int d^N \psi \mathcal{P}(\phi|\psi, \mathcal{D}) \mathcal{P}(\psi|\mathcal{D}) . \quad (\text{C.2})$$

Given a mapping  $\mathcal{P}(\phi|\psi) = \prod_{i=1}^N \delta_D(\psi_i - M_{i\alpha} \phi_\alpha)$ , eq. (C.2) translates the possibility to compress the data  $\mathcal{D}$  into the posterior distribution  $\mathcal{P}(\psi|\mathcal{D})$  and use it as a likelihood to sample the probability distribution of the model parameters  $\phi$ , similarly to other situations in cosmology (see e.g., [124, 19]). In our case, eq. (C.2) means we can reconstruct  $\mathcal{P}(\phi|\mathcal{D})$ , the posterior of  $(w_0, w_a)$ , from  $\mathcal{P}(\psi|\mathcal{D})$ , the posterior of  $(w_1^z, \dots, w_N^z)$ . Since  $M$  is not surjective, the converse is not true.

To close the loop, we can finally insert eq. (C.2) into eq. (C.1) to relate the two reconstructions of  $w(z)$ , yielding

$$\mathcal{P}_{\mathcal{T}}(\psi|\mathcal{D}) = \int_{\psi' \in \mathcal{T}} d^N \psi' \delta_D(\psi - \psi') \mathcal{P}(\psi'|\mathcal{D}) . \quad (\text{C.3})$$

This translates the fact that  $\mathcal{P}_{\mathcal{T}}$  is the projection of  $\mathcal{P}(\psi|\mathcal{D})$  onto the target space  $\mathcal{T}$  of  $M$ . We conclude that the reconstructed  $w(z)$  being constrained by  $(w_0, w_a)$  is in general not representative of the data sensitivity on  $w(z)$ .

**Analytical posterior for Gaussian distributions** For near Gaussian distributions (as we deal with in this paper), we can derive analytical solutions for the formulae above to get posterior distributions and significance (likelihood-ratio) at low cost. In the following, we assume that  $\mathcal{P}(\psi|\mathcal{D})$  is given to us and derive the evidence of the model  $\phi$  over  $\Lambda$ , the null hypothesis.

Assuming  $\mathcal{P}(\psi|\mathcal{D})$  to be a multivariate normal distribution  $\mathcal{N}(\psi|\bar{\psi}, \mathcal{C})$ , we can solve eq. (C.2) exactly by projecting the  $N$ -D Gaussian onto the domain  $\Omega_\phi$ , yielding  $\mathcal{P}(\phi|\mathcal{D}) = \mathcal{N}(\phi|\bar{\phi}, \Sigma)$ , where

$$\bar{\phi} = \Sigma M^T \mathcal{C}^{-1} \bar{\psi} , \quad \Sigma = (M^T \mathcal{C}^{-1} M)^{-1} . \quad (\text{C.4})$$

For completeness, we also provide the expressions to get  $\mathcal{P}_{\mathcal{T}}(\psi|\mathcal{D})$ . We can solve eq. (C.1) exactly by projecting the 2D Gaussian onto the 1D constraints  $\psi_i = M_{i\alpha} \phi_\alpha$ , yielding  $\mathcal{P}_{\mathcal{T}}(\psi|\mathcal{D}) = \mathcal{N}(\psi|\bar{\psi}_{\mathcal{T}}, \mathcal{C}_{\mathcal{T}})$ , where

$$\bar{\psi}_{\mathcal{T}} = M \bar{\phi} , \quad \mathcal{C}_{\mathcal{T}} = M \Sigma M^T . \quad (\text{C.5})$$

Notice that  $\mathcal{C}_{\mathcal{T}}$  is nothing but eq. (5.2) for  $z_i = z_*$ . Using eqs. (C.4) and (C.5), we find that

$$\bar{\psi}_{\mathcal{T}} = M (M^T \mathcal{C}^{-1} M)^{-1} M^T \mathcal{C}^{-1} \bar{\psi} , \quad \mathcal{C}_{\mathcal{T}} = M (M^T \mathcal{C}^{-1} M)^{-1} M^T . \quad (\text{C.6})$$

Note that  $\mathcal{C}_{\mathcal{T}} \neq \mathcal{C}$  given that  $\psi$  and  $\phi$  are not equivalent parametrisations of the same model (*i.e.*,  $M$  is not a bijective map — a square invertible matrix).

We now show how we quantify the evidence for evolving dark energy over  $\Lambda$  as well as the evidence for phantom dark energy. For a normal distribution  $\mathcal{N}(\phi|\bar{\phi}, \Sigma)$ , the log-likelihood ratio with respect to the null hypothesis  $\Lambda$  can be found as the square distance to a point  $\phi_{\Lambda} \equiv (-1, 0)^T$ , reading

$$\lambda(\phi_{\Lambda}) = (\phi_{\Lambda} - \bar{\phi})^T \Sigma^{-1} (\phi_{\Lambda} - \bar{\phi}) . \quad (\text{C.7})$$

Given that the posterior of  $(w_0, w_a)$  is near Gaussian, we find that (C.7) agrees well with the  $\Delta\chi_{\min}^2$  from full numerical minimisation, allowing us to quantify the evidence for evolving dark energy over  $\Lambda$ . Regarding the evidence for  $w < -1$ , we evaluate the difference between the maximum of  $\mathcal{N}(\phi|\bar{\phi}, \Sigma)$  (where  $\phi$  is taken as  $(w_0, w_a)$ ) with the one found profiling the line  $w(a) = -1$ .<sup>33</sup> The square distance to a line  $\phi(\tau) = \phi_{\Lambda} + \tau\mathbf{v}$  is given by

$$\lambda(\phi(\tau)) = \lambda(\phi_{\Lambda}) - \frac{(\mathbf{v}^T \Sigma^{-1} (\phi_{\Lambda} - \bar{\phi}))^2}{\mathbf{v}^T \Sigma^{-1} \mathbf{v}}. \quad (\text{C.8})$$

## References

- [1] DESI collaboration, *DESI 2024 VI: cosmological constraints from the measurements of baryon acoustic oscillations*, *JCAP* **02** (2025) 021 [[2404.03002](#)].
- [2] EUCLID collaboration, *Euclid. I. Overview of the Euclid mission*, [2405.13491](#).
- [3] DESI collaboration, *DESI 2024 VII: Cosmological Constraints from the Full-Shape Modeling of Clustering Measurements*, [2411.12022](#).
- [4] D. Baumann, A. Nicolis, L. Senatore and M. Zaldarriaga, *Cosmological Non-Linearities as an Effective Fluid*, *JCAP* **07** (2012) 051 [[1004.2488](#)].
- [5] J.J.M. Carrasco, M.P. Hertzberg and L. Senatore, *The Effective Field Theory of Cosmological Large Scale Structures*, *JHEP* **09** (2012) 082 [[1206.2926](#)].
- [6] L. Senatore and M. Zaldarriaga, *The IR-resummed Effective Field Theory of Large Scale Structures*, *JCAP* **02** (2015) 013 [[1404.5954](#)].
- [7] L. Senatore, *Bias in the Effective Field Theory of Large Scale Structures*, *JCAP* **11** (2015) 007 [[1406.7843](#)].
- [8] L. Senatore and M. Zaldarriaga, *Redshift Space Distortions in the Effective Field Theory of Large Scale Structures*, [1409.1225](#).
- [9] A. Perko, L. Senatore, E. Jennings and R.H. Wechsler, *Biased Tracers in Redshift Space in the EFT of Large-Scale Structure*, [1610.09321](#).
- [10] G. D’Amico, J. Gleyzes, N. Kokron, K. Markovic, L. Senatore, P. Zhang et al., *The Cosmological Analysis of the SDSS/BOSS data from the Effective Field Theory of Large-Scale Structure*, *JCAP* **05** (2020) 005 [[1909.05271](#)].
- [11] M.M. Ivanov, M. Simonović and M. Zaldarriaga, *Cosmological Parameters from the BOSS Galaxy Power Spectrum*, *JCAP* **05** (2020) 042 [[1909.05277](#)].

---

<sup>33</sup>This is true only because  $\sup_{\{\phi|w \forall \geq -1\}} \mathcal{P}(\phi|\mathcal{D})$  lies on the  $w(t) = -1$  line.



- [12] S.-F. Chen, Z. Vlah and M. White, *A new analysis of galaxy 2-point functions in the BOSS survey, including full-shape information and post-reconstruction BAO*, *JCAP* **02** (2022) 008 [[2110.05530](#)].
- [13] T. Simon, P. Zhang and V. Poulin, *Cosmological inference from the EFTofLSS: the eBOSS QSO full-shape analysis*, *JCAP* **07** (2023) 041 [[2210.14931](#)].
- [14] M. Maus et al., *A comparison of effective field theory models of redshift space galaxy power spectra for DESI 2024 and future surveys*, *JCAP* **01** (2025) 134 [[2404.07272](#)].
- [15] G. D’Amico, Y. Donath, M. Lewandowski, L. Senatore and P. Zhang, *The one-loop bispectrum of galaxies in redshift space from the Effective Field Theory of Large-Scale Structure*, *JCAP* **07** (2024) 041 [[2211.17130](#)].
- [16] C. Anastasiou, D.P.L. Bragança, L. Senatore and H. Zheng, *Efficiently evaluating loop integrals in the EFTofLSS using QFT integrals with massive propagators*, *JHEP* **01** (2024) 002 [[2212.07421](#)].
- [17] G. D’Amico, Y. Donath, M. Lewandowski, L. Senatore and P. Zhang, *The BOSS bispectrum analysis at one loop from the Effective Field Theory of Large-Scale Structure*, *JCAP* **05** (2024) 059 [[2206.08327](#)].
- [18] S. Spaar and P. Zhang, *Cosmological constraints from combined probes with the three-point statistics of galaxies at one-loop precision*, *Phys. Rev. D* **111** (2025) 023529 [[2312.15164](#)].
- [19] BOSS collaboration, *The clustering of galaxies in the completed SDSS-III Baryon Oscillation Spectroscopic Survey: cosmological analysis of the DR12 galaxy sample*, *Mon. Not. Roy. Astron. Soc.* **470** (2017) 2617 [[1607.03155](#)].
- [20] eBOSS collaboration, *Baryon acoustic oscillations at  $z = 2.34$  from the correlations of Ly $\alpha$  absorption in eBOSS DR14*, *Astron. Astrophys.* **629** (2019) A85 [[1904.03400](#)].
- [21] G. Gubitosi, F. Piazza and F. Vernizzi, *The Effective Field Theory of Dark Energy*, *JCAP* **02** (2013) 032 [[1210.0201](#)].
- [22] J. Gleyzes, D. Langlois, F. Piazza and F. Vernizzi, *Essential Building Blocks of Dark Energy*, *JCAP* **08** (2013) 025 [[1304.4840](#)].
- [23] D. Brout et al., *The Pantheon+ Analysis: Cosmological Constraints*, *Astrophys. J.* **938** (2022) 110 [[2202.04077](#)].
- [24] D. Rubin et al., *Union Through UNITY: Cosmology with 2,000 SNe Using a Unified Bayesian Framework*, [2311.12098](#).
- [25] DES collaboration, *The Dark Energy Survey: Cosmology Results with  $\sim 1500$  New High-redshift Type Ia Supernovae Using the Full 5 yr Data Set*, *Astrophys. J. Lett.* **973** (2024) L14 [[2401.02929](#)].

- [26] F. Beutler, C. Blake, M. Colless, D.H. Jones, L. Staveley-Smith, L. Campbell et al., *The 6dF Galaxy Survey: Baryon Acoustic Oscillations and the Local Hubble Constant*, *Mon. Not. Roy. Astron. Soc.* **416** (2011) 3017 [[1106.3366](#)].
- [27] A.J. Ross, L. Samushia, C. Howlett, W.J. Percival, A. Burden and M. Manera, *The clustering of the SDSS DR7 main Galaxy sample – I. A 4 per cent distance measure at  $z = 0.15$* , *Mon. Not. Roy. Astron. Soc.* **449** (2015) 835 [[1409.3242](#)].
- [28] P. Creminelli, M.A. Luty, A. Nicolis and L. Senatore, *Starting the Universe: Stable Violation of the Null Energy Condition and Non-standard Cosmologies*, *JHEP* **12** (2006) 080 [[hep-th/0606090](#)].
- [29] C. Cheung, P. Creminelli, A.L. Fitzpatrick, J. Kaplan and L. Senatore, *The Effective Field Theory of Inflation*, *JHEP* **03** (2008) 014 [[0709.0293](#)].
- [30] P. Creminelli, G. D’Amico, J. Norena and F. Vernizzi, *The Effective Theory of Quintessence: the  $w < -1$  Side Unveiled*, *JCAP* **02** (2009) 018 [[0811.0827](#)].
- [31] M. Lewandowski, A. Maleknejad and L. Senatore, *An effective description of dark matter and dark energy in the mildly non-linear regime*, *JCAP* **05** (2017) 038 [[1611.07966](#)].
- [32] E. Bellini and I. Sawicki, *Maximal freedom at minimum cost: linear large-scale structure in general modifications of gravity*, *JCAP* **07** (2014) 050 [[1404.3713](#)].
- [33] J. Gleyzes, D. Langlois and F. Vernizzi, *A unifying description of dark energy*, *Int. J. Mod. Phys. D* **23** (2015) 1443010 [[1411.3712](#)].
- [34] G. Cusin, M. Lewandowski and F. Vernizzi, *Dark Energy and Modified Gravity in the Effective Field Theory of Large-Scale Structure*, *JCAP* **04** (2018) 005 [[1712.02783](#)].
- [35] G. Cusin, M. Lewandowski and F. Vernizzi, *Nonlinear Effective Theory of Dark Energy*, *JCAP* **04** (2018) 061 [[1712.02782](#)].
- [36] E. Sefusatti and F. Vernizzi, *Cosmological structure formation with clustering quintessence*, *JCAP* **03** (2011) 047 [[1101.1026](#)].
- [37] A. Nicolis, R. Rattazzi and E. Trincherini, *The Galileon as a local modification of gravity*, *Phys. Rev. D* **79** (2009) 064036 [[0811.2197](#)].
- [38] C. Deffayet, O. Pujolas, I. Sawicki and A. Vikman, *Imperfect Dark Energy from Kinetic Gravity Braiding*, *JCAP* **10** (2010) 026 [[1008.0048](#)].
- [39] N. Arkani-Hamed, H.-C. Cheng, M.A. Luty and S. Mukohyama, *Ghost condensation and a consistent infrared modification of gravity*, *JHEP* **05** (2004) 074 [[hep-th/0312099](#)].
- [40] G. D’Amico, N. Kaloper and A. Lawrence, *Strongly Coupled Quintessence*, *Phys. Rev. D* **100** (2019) 103504 [[1809.05109](#)].

- [41] M. Peloso and M. Pietroni, *Galilean invariance and the consistency relation for the nonlinear squeezed bispectrum of large scale structure*, *JCAP* **05** (2013) 031 [[1302.0223](#)].
- [42] A. Kehagias and A. Riotto, *Symmetries and Consistency Relations in the Large Scale Structure of the Universe*, *Nucl. Phys. B* **873** (2013) 514 [[1302.0130](#)].
- [43] P. Creminelli, J. Noreña, M. Simonović and F. Vernizzi, *Single-Field Consistency Relations of Large Scale Structure*, *JCAP* **12** (2013) 025 [[1309.3557](#)].
- [44] G. D’Amico, Y. Donath, L. Senatore and P. Zhang, *Limits on clustering and smooth quintessence from the EFTofLSS*, *JCAP* **03** (2024) 032 [[2012.07554](#)].
- [45] G. D’Amico, M. Marinucci, M. Pietroni and F. Vernizzi, *The large scale structure bootstrap: perturbation theory and bias expansion from symmetries*, *JCAP* **10** (2021) 069 [[2109.09573](#)].
- [46] P. Zhang and Y. Cai, *BOSS full-shape analysis from the EFTofLSS with exact time dependence*, *JCAP* **01** (2022) 031 [[2111.05739](#)].
- [47] P. McDonald, *Clustering of dark matter tracers: Renormalizing the bias parameters*, *Phys. Rev. D* **74** (2006) 103512 [[astro-ph/0609413](#)].
- [48] P. McDonald and A. Roy, *Clustering of dark matter tracers: generalizing bias for the coming era of precision LSS*, *JCAP* **08** (2009) 020 [[0902.0991](#)].
- [49] M. Mirbabayi, F. Schmidt and M. Zaldarriaga, *Biased Tracers and Time Evolution*, *JCAP* **07** (2015) 030 [[1412.5169](#)].
- [50] Y. Donath and L. Senatore, *Biased Tracers in Redshift Space in the EFTofLSS with exact time dependence*, *JCAP* **10** (2020) 039 [[2005.04805](#)].
- [51] R. Angulo, M. Fasiello, L. Senatore and Z. Vlah, *On the Statistics of Biased Tracers in the Effective Field Theory of Large Scale Structures*, *JCAP* **09** (2015) 029 [[1503.08826](#)].
- [52] T. Fujita, V. Mauerhofer, L. Senatore, Z. Vlah and R. Angulo, *Very Massive Tracers and Higher Derivative Biases*, *JCAP* **01** (2020) 009 [[1609.00717](#)].
- [53] T. Fujita and Z. Vlah, *Perturbative description of biased tracers using consistency relations of LSS*, *JCAP* **10** (2020) 059 [[2003.10114](#)].
- [54] T. Matsubara, *Resumming Cosmological Perturbations via the Lagrangian Picture: One-loop Results in Real Space and in Redshift Space*, *Phys. Rev. D* **77** (2008) 063530 [[0711.2521](#)].
- [55] M. Lewandowski, L. Senatore, F. Prada, C. Zhao and C.-H. Chuang, *EFT of large scale structures in redshift space*, *Phys. Rev. D* **97** (2018) 063526 [[1512.06831](#)].

- [56] G. D’Amico, L. Senatore, P. Zhang and T. Nishimichi, *Taming redshift-space distortion effects in the EFTofLSS and its application to data*, *JCAP* **01** (2024) 037 [[2110.00016](#)].
- [57] J.J.M. Carrasco, S. Foreman, D. Green and L. Senatore, *The Effective Field Theory of Large Scale Structures at Two Loops*, *JCAP* **07** (2014) 057 [[1310.0464](#)].
- [58] R. Scoccimarro, H.M.P. Couchman and J.A. Frieman, *The Bispectrum as a Signature of Gravitational Instability in Redshift-Space*, *Astrophys. J.* **517** (1999) 531 [[astro-ph/9808305](#)].
- [59] R.A. Porto, L. Senatore and M. Zaldarriaga, *The Lagrangian-space Effective Field Theory of Large Scale Structures*, *JCAP* **05** (2014) 022 [[1311.2168](#)].
- [60] L. Senatore and G. Trevisan, *On the IR-Resummation in the EFTofLSS*, *JCAP* **05** (2018) 019 [[1710.02178](#)].
- [61] G. D’Amico, L. Senatore and P. Zhang, *Limits on  $w$ CDM from the EFTofLSS with the PyBird code*, *JCAP* **01** (2021) 006 [[2003.07956](#)].
- [62] M. Chevallier and D. Polarski, *Accelerating universes with scaling dark matter*, *Int. J. Mod. Phys. D* **10** (2001) 213 [[gr-qc/0009008](#)].
- [63] E.V. Linder, *Exploring the expansion history of the universe*, *Phys. Rev. Lett.* **90** (2003) 091301 [[astro-ph/0208512](#)].
- [64] PLANCK collaboration, *Planck 2018 results. V. CMB power spectra and likelihoods*, *Astron. Astrophys.* **641** (2020) A5 [[1907.12875](#)].
- [65] PLANCK collaboration, *Planck 2018 results. VIII. Gravitational lensing*, *Astron. Astrophys.* **641** (2020) A8 [[1807.06210](#)].
- [66] BOSS collaboration, *SDSS-III Baryon Oscillation Spectroscopic Survey Data Release 12: galaxy target selection and large scale structure catalogues*, *Mon. Not. Roy. Astron. Soc.* **455** (2016) 1553 [[1509.06529](#)].
- [67] F.-S. Kitaura et al., *The clustering of galaxies in the SDSS-III Baryon Oscillation Spectroscopic Survey: mock galaxy catalogues for the BOSS Final Data Release*, *Mon. Not. Roy. Astron. Soc.* **456** (2016) 4156 [[1509.06400](#)].
- [68] F. Beutler, E. Castorina and P. Zhang, *Interpreting measurements of the anisotropic galaxy power spectrum*, *JCAP* **03** (2019) 040 [[1810.05051](#)].
- [69] A. Cuceu, J. Farr, P. Lemos and A. Font-Ribera, *Baryon Acoustic Oscillations and the Hubble Constant: Past, Present and Future*, *JCAP* **10** (2019) 044 [[1906.11628](#)].
- [70] J. Torrado and A. Lewis, *Cobaya: Code for Bayesian Analysis of hierarchical physical models*, *JCAP* **05** (2021) 057 [[2005.05290](#)].

- [71] DESI collaboration, *DESI 2024 II: Sample Definitions, Characteristics, and Two-point Clustering Statistics*, [2411.12020](#).
- [72] G.S. Farren, O.H.E. Philcox and B.D. Sherwin, *Determining the Hubble constant without the sound horizon: Perspectives with future galaxy surveys*, *Phys. Rev. D* **105** (2022) 063503 [[2112.10749](#)].
- [73] T.L. Smith, V. Poulin and T. Simon, *Assessing the robustness of sound horizon-free determinations of the Hubble constant*, *Phys. Rev. D* **108** (2023) 103525 [[2208.12992](#)].
- [74] J. Hamann, S. Hannestad, J. Lesgourgues, C. Rampf and Y.Y.Y. Wong, *Cosmological parameters from large scale structure - geometric versus shape information*, *JCAP* **07** (2010) 022 [[1003.3999](#)].
- [75] T. Brinckmann and J. Lesgourgues, *MontePython 3: boosted MCMC sampler and other features*, *Phys. Dark Univ.* **24** (2019) 100260 [[1804.07261](#)].
- [76] B. Audren, J. Lesgourgues, K. Benabed and S. Prunet, *Conservative Constraints on Early Cosmology: an illustration of the Monte Python cosmological parameter inference code*, *JCAP* **02** (2013) 001 [[1210.7183](#)].
- [77] J. Lesgourgues, *The Cosmic Linear Anisotropy Solving System (CLASS) I: Overview*, [1104.2932](#).
- [78] D. Blas, J. Lesgourgues and T. Tram, *The Cosmic Linear Anisotropy Solving System (CLASS) II: Approximation schemes*, *JCAP* **07** (2011) 034 [[1104.2933](#)].
- [79] M. Zumalacárregui, E. Bellini, I. Sawicki, J. Lesgourgues and P.G. Ferreira, *hi\_class: Horndeski in the Cosmic Linear Anisotropy Solving System*, *JCAP* **08** (2017) 019 [[1605.06102](#)].
- [80] E. Bellini, I. Sawicki and M. Zumalacárregui, *hi\_class: Background Evolution, Initial Conditions and Approximation Schemes*, *JCAP* **02** (2020) 008 [[1909.01828](#)].
- [81] L. Piga, M. Marinucci, G. D’Amico, M. Pietroni, F. Vernizzi and B.S. Wright, *Constraints on modified gravity from the BOSS galaxy survey*, *JCAP* **04** (2023) 038 [[2211.12523](#)].
- [82] T. Karwal, Y. Patel, A. Bartlett, V. Poulin, T.L. Smith and D.N. Pfeffer, *Procoli: Profiles of cosmological likelihoods*, [2401.14225](#).
- [83] A. Lewis, *GetDist: a Python package for analysing Monte Carlo samples*, [1910.13970](#).
- [84] H.A. Feldman, N. Kaiser and J.A. Peacock, *Power spectrum analysis of three-dimensional redshift surveys*, *Astrophys. J.* **426** (1994) 23 [[astro-ph/9304022](#)].
- [85] R. Scoccimarro, *Fast Estimators for Redshift-Space Clustering*, *Phys. Rev. D* **92** (2015) 083532 [[1506.02729](#)].

- [86] BOSS collaboration, *The clustering of galaxies in the SDSS-III Baryon Oscillation Spectroscopic Survey: RSD measurement from the LOS-dependent power spectrum of DR12 BOSS galaxies*, *Mon. Not. Roy. Astron. Soc.* **460** (2016) 4188 [[1509.06386](#)].
- [87] J. Hartlap, P. Simon and P. Schneider, *Why your model parameter confidences might be too optimistic: Unbiased estimation of the inverse covariance matrix*, *Astron. Astrophys.* **464** (2007) 399 [[astro-ph/0608064](#)].
- [88] T. Nishimichi, G. D’Amico, M.M. Ivanov, L. Senatore, M. Simonović, M. Takada et al., *Blinded challenge for precision cosmology with large-scale structure: results from effective field theory for the redshift-space galaxy power spectrum*, *Phys. Rev. D* **102** (2020) 123541 [[2003.08277](#)].
- [89] S.-F. Chen, Z. Vlah, E. Castorina and M. White, *Redshift-Space Distortions in Lagrangian Perturbation Theory*, *JCAP* **03** (2021) 100 [[2012.04636](#)].
- [90] T. Colas, G. D’amico, L. Senatore, P. Zhang and F. Beutler, *Efficient Cosmological Analysis of the SDSS/BOSS data from the Effective Field Theory of Large-Scale Structure*, *JCAP* **06** (2020) 001 [[1909.07951](#)].
- [91] P. Zhang, G. D’Amico, L. Senatore, C. Zhao and Y. Cai, *BOSS Correlation Function analysis from the Effective Field Theory of Large-Scale Structure*, *JCAP* **02** (2022) 036 [[2110.07539](#)].
- [92] T. Simon, P. Zhang, V. Poulin and T.L. Smith, *Consistency of effective field theory analyses of the BOSS power spectrum*, *Phys. Rev. D* **107** (2023) 123530 [[2208.05929](#)].
- [93] R. Zhao et al., *A multitracer analysis for the eBOSS galaxy sample based on the effective field theory of large-scale structure*, *Mon. Not. Roy. Astron. Soc.* **532** (2024) 783 [[2308.06206](#)].
- [94] A. Albrecht et al., *Report of the Dark Energy Task Force*, [astro-ph/0609591](#).
- [95] D. Braganca, Y. Donath, L. Senatore and H. Zheng, *Peeking into the next decade in Large-Scale Structure Cosmology with its Effective Field Theory*, [2307.04992](#).
- [96] G. D’Amico, M. Lewandowski, L. Senatore and P. Zhang, *Limits on primordial non-Gaussianities from BOSS galaxy-clustering data*, [2201.11518](#).
- [97] P. Taule, M. Marinucci, G. Biselli, M. Pietroni and F. Vernizzi, *Constraints on dark energy and modified gravity from the BOSS Full-Shape and DESI BAO data*, [2409.08971](#).
- [98] M. Cortês and A.R. Liddle, *Interpreting DESI’s evidence for evolving dark energy*, *JCAP* **12** (2024) 007 [[2404.08056](#)].
- [99] DESI collaboration, *DESI 2024: reconstructing dark energy using crossing statistics with DESI DR1 BAO data*, *JCAP* **10** (2024) 048 [[2405.04216](#)].



- [100] M. Raveri, L. Pogosian, M. Martinelli, K. Koyama, A. Silvestri and G.-B. Zhao, *Principal reconstructed modes of dark energy and gravity*, *JCAP* **02** (2023) 061 [[2107.12990](#)].
- [101] L. Pogosian, M. Raveri, K. Koyama, M. Martinelli, A. Silvestri, G.-B. Zhao et al., *Imprints of cosmological tensions in reconstructed gravity*, *Nature Astron.* **6** (2022) 1484 [[2107.12992](#)].
- [102] G. Ye, M. Martinelli, B. Hu and A. Silvestri, *Non-minimally coupled gravity as a physically viable fit to DESI 2024 BAO*, [2407.15832](#).
- [103] Y. Yang, Q. Wang, C. Li, P. Yuan, X. Ren, E.N. Saridakis et al., *Gaussian-process reconstructions and model building of quintom dark energy from latest cosmological observations*, [2501.18336](#).
- [104] C. Csaki, N. Kaloper and J. Terning, *The Accelerated acceleration of the Universe*, *JCAP* **06** (2006) 022 [[astro-ph/0507148](#)].
- [105] W. Fang, W. Hu and A. Lewis, *Crossing the Phantom Divide with Parameterized Post-Friedmann Dark Energy*, *Phys. Rev. D* **78** (2008) 087303 [[0808.3125](#)].
- [106] Y.-F. Cai, E.N. Saridakis, M.R. Setare and J.-Q. Xia, *Quintom Cosmology: Theoretical implications and observations*, *Phys. Rept.* **493** (2010) 1 [[0909.2776](#)].
- [107] C. Deffayet, S. Mukohyama and A. Vikman, *Ghosts without Runaway Instabilities*, *Phys. Rev. Lett.* **128** (2022) 041301 [[2108.06294](#)].
- [108] W.J. Wolf and P.G. Ferreira, *Underdetermination of dark energy*, *Phys. Rev. D* **108** (2023) 103519 [[2310.07482](#)].
- [109] D. Shlivko and P.J. Steinhardt, *Assessing observational constraints on dark energy*, *Phys. Lett. B* **855** (2024) 138826 [[2405.03933](#)].
- [110] I.D. Gialamas, G. Hütsi, K. Kannike, A. Racioppi, M. Raidal, M. Vasar et al., *Interpreting DESI 2024 BAO: Late-time dynamical dark energy or a local effect?*, *Phys. Rev. D* **111** (2025) 043540 [[2406.07533](#)].
- [111] P. Creminelli and F. Vernizzi, *Dark Energy after GW170817 and GRB170817A*, *Phys. Rev. Lett.* **119** (2017) 251302 [[1710.05877](#)].
- [112] P. Creminelli, M. Lewandowski, G. Tambalo and F. Vernizzi, *Gravitational Wave Decay into Dark Energy*, *JCAP* **12** (2018) 025 [[1809.03484](#)].
- [113] P. Creminelli, G. Tambalo, F. Vernizzi and V. Yingcharoenrat, *Resonant Decay of Gravitational Waves into Dark Energy*, *JCAP* **10** (2019) 072 [[1906.07015](#)].
- [114] LIGO SCIENTIFIC, VIRGO collaboration, *GW170817: Observation of Gravitational Waves from a Binary Neutron Star Inspiral*, *Phys. Rev. Lett.* **119** (2017) 161101 [[1710.05832](#)].

- [115] C. de Rham and S. Melville, *Gravitational Rainbows: LIGO and Dark Energy at its Cutoff*, *Phys. Rev. Lett.* **121** (2018) 221101 [[1806.09417](#)].
- [116] G. Efstathiou, *Evolving Dark Energy or Supernovae Systematics?*, [2408.07175](#).
- [117] L. Huang, R.-G. Cai and S.-J. Wang, *The DESI 2024 hint for dynamical dark energy is biased by low-redshift supernovae*, [2502.04212](#).
- [118] J. Gleyzes, D. Langlois, F. Piazza and F. Vernizzi, *Healthy theories beyond Horndeski*, *Phys. Rev. Lett.* **114** (2015) 211101 [[1404.6495](#)].
- [119] E.V. Linder, *Quintessence's last stand?*, *Phys. Rev. D* **91** (2015) 063006 [[1501.01634](#)].
- [120] W.J. Wolf, C. García-García, D.J. Bartlett and P.G. Ferreira, *Scant evidence for thawing quintessence*, *Phys. Rev. D* **110** (2024) 083528 [[2408.17318](#)].
- [121] S. Lee and K.-W. Ng, *Growth index with the exact analytic solution of sub-horizon scale linear perturbation for dark energy models with constant equation of state*, *Phys. Lett. B* **688** (2010) 1 [[0906.1643](#)].
- [122] V. Desjacques, D. Jeong and F. Schmidt, *Large-Scale Galaxy Bias*, *Phys. Rept.* **733** (2018) 1 [[1611.09787](#)].
- [123] A. Eggemeier, R. Scoccimarro and R.E. Smith, *Bias Loop Corrections to the Galaxy Bispectrum*, *Phys. Rev. D* **99** (2019) 123514 [[1812.03208](#)].
- [124] B.D. Wandelt, D.L. Larson and A. Lakshminarayanan, *Global, exact cosmic microwave background data analysis using Gibbs sampling*, *Phys. Rev. D* **70** (2004) 083511 [[astro-ph/0310080](#)].